UNIVERSITÀ DEGLI STUDI DI NAPOLI “FEDERICO II”

Dottorato di Ricerca in Fisica Fondamentale ed Applicata
XIX Ciclo

Dr. Agostino Migliaccio

Neutralino Spin Measurement with the ATLAS detector at LHC

Thesis for Doctor of Philosophy degree

Coordinatore del Dottorato di Ricerca:
Prof. Gennaro Miele

NOVEMBRE 2006

Contents

Introduction

This thesis is dedicated to the study of second lightest neutralino spin measurement with ATLAS detector at the **L**arge **H**adron **C**ollider (LHC), the new high energy proton-proton collider which is entering in the final construction and testing phase at the CERN in Geneva: data taking is expected to start in 2008, after a brief operation period at 900 GeV in the center of mass on December 2007. Bunches of protons can collide at a center of mass energy of 14 TeV with an initial reduced luminosity (low luminosity $\sim$ 10^{33} cm^{-2}s^{-1}), during first three years and, subsequently, with the project luminosity of 10^{34} cm^{-2}s^{-1} which will allow the study of low cross section processes. ATLAS (**A** **T**oroidal **L**HC **A**pparatu**S**) is one of the four detectors (general purpose detector) designed to cope with the very extreme operating conditions, in terms of luminosity, latency, radiation, occupancy etc. expected at the new hadron collider. One of the goals of the ATLAS experiment is to search for evidence of new physics: the Minimal Supersymmetric extension of the Standard Model (MSSM) is one of the most promising candidates to describe the physics beyond the Standard Model. It is characterized by a huge number of free parameters which can be significantly reduced by assuming a particular supersymmetry (SUSY) breaking mechanism: the minimal Supergravity (mSUGRA) model is the theory in which the spontaneous breaking mechanism is operated (communicated from the hidden sector to the visible one) by means of gravity. Within mSUGRA framework, masses, mixings and decays of all SUSY and Higgs particles are determined in terms of only four parameters and a sign: the common mass m_0 of scalar particles, the common fermion mass $m_{1/2}$ and the common trilinear coupling A_0 at the grand unification scale (GUT), the ratio of the Higgs vacuum expectation values tanβ and the sign of the supersymmetric Higgs mass parameter μ. Moreover, in the mSUGRA model, R-parity is conserved and the lightest supersymmetric particle ($\tilde{\chi}_1^0$) represents a good candidate for the cold Dark Matter. In particular two search strategies for supersymmetric particles have been studied in the ATLAS experiment: namely inclusive and exclusive searches. Inclusive analyses consist in searching for

generic SUSY signals such as missing transverse energy plus high transverse momentum multi-jets plus, eventually, leptons. In this way it will be possible to show any deviations with respect to what expected from Standard Model predictions and, at the same time, to measure the SUSY mass scale. After this phase, if new physics emerge, it will be necessary to characterize it with measurements of branching ratios, masses, spins, etc. This is the subject of exclusive analyses which consist in reconstructing particular decay chains from which it is possible to extract useful information. In this context is set the work described in this thesis: it represents a feasibility study of second lightest neutralino spin measurement (the aim is to verify if it is possible to perform such a measurement and, eventually, which luminosity is needed) for two different benchmark points (selected by ATLAS collaboration) in the mSUGRA parameter space allowed by cosmology (that is in agreement with WMAP experiment data): namely a "typical" point in bulk region (SU3) and, as a more complicated case, a point in stau-coannihilation region (SU1). In particular, the decay chain $\tilde{q}_L \rightarrow \tilde{\chi}_2^0 q \rightarrow \tilde{l}_{L,R}^{\pm} l^{\mp} q \rightarrow l^+ l^- q \ \tilde{\chi}_1^0$ will be studied in order to verify the consistency of the spin-$1/2$ neutralino hypothesis, by looking for charge (charge of lepton) asymmetry in lepton-jet invariant mass distributions. At this purpose all studies will be performed by using the fast simulation software, ATLFAST, which does not simulate interactions of generated particles with the detector, but it only parametrizes momentum and energy, associated with each particle, by means of detection efficiencies and detector resolutions tabulated in the program. The thesis is composed as it follows:

Chapter1 describes the theoretical framework of Supersymmetry, starting from the minimal supersymmetric standard model (MSSM), illustrating its properties, the supersymmetry breaking mechanism which allows to introduce the minimal supergravity model (mSUGRA), mass spectrum and decays of supersymmetric particles.

Chapter2 is dedicated to the description of the Large Hadron Collider and of the ATLAS detector.

In Chapter3 the actual limits on Supersymmetry coming from searches at LEP and Tevatron collider and those coming from indirect measurements and WMAP experiment are presented. There, it will be illustrate the phenomenology of Supersymmetry at LHC and the search strategies for SUSY at the ATLAS experiment.

In Chapter4 the strategy applied for spin measurement, starting from left squark decay chain, is described. Experimental effects which can dilute charge asymmetry measurements (from charge asymmetry it is possible to extract spin information) are introduced and discussed. Features of the studied mSUGRA points, kinematic properties of left squark decay chain for these points, Monte

Carlo data sets, MC truth level distributions of invariant masses and charge asymmetries are also presented. Finally, analysis procedure, including event selection, background study, reconstruction of invariant masses, statistical methods used for estimating charge asymmetries is reported together with results on the detectability of such a measurement for both points under consideration.

Chapter 1

Theory

In this chapter I'm going to describe the motivations for introducing Supersymmetry, the minimal new particles content and something about the phenomenology: it represents the theoretical frame on which is based the whole present thesis.

1.1 The Standard Model

The Standard Model (SM) is a theory that allow us to classify the elementary particles and to describe their interactions. It is only recently, observing the evidence of neutrino oscillations, that the model is found to be in disagreement with the experiments. The SM is a re-normalizable [1] gauge field theory where the elementary particles (quarks and leptons having a semi-integer spin) interact by means of particles, with an integer spin, which mediate the interactions (representing excited states of the quantum mechanical fields), called vector bosons.

The Standard Model describes the three fundamental forces by means of the following combination of algebraic groups: $U(1) \times SU(2) \times SU(3)$ representing the electromagnetic, weak and strong interactions. There are three gauge quantum numbers (called charges) associated with each of the interactions: they are known as hypercharge, weak isospin and color respectively. The number of the vector boson mediators is equal to the number of generators of the corresponding symmetry group. So we have one hypercharge gauge boson (B) for $U(1)$, three weak-isospin gauge bosons

[1] It means that the probability amplitudes of the physical processes are not divergent at high energies.

(W_1, W_2, W_3) for $SU(2)$ and eight color gluons (g_i) for $SU(3)$. At this level we are talking about massless particles even if we know that some of them are massive particles as shown by experiments (it can be shown that the massive vector bosons have a mass of the order of ~ 100 GeV and some leptons and quarks have masses up to 174 GeV). There is no way to include the mass terms in the SM lagrangian without breaking gauge invariance and, consequently, the renormalizability of the theory.

Fermions	Isospin I	I_3	Hypercharge Y	Charge Q = $\frac{I_3}{2}$ + Y	Interactions
ν_{l_L}	$1/2$	$+1/2$	-1	0	weak
l_L	$1/2$	$-1/2$	-1	-1	EM, weak
ν_{l_R}	0	0	0	0	weak
l_R	0	0	-2	-1	EM, weak
u_L	$1/2$	$+1/2$	$+1/3$	$+2/3$	EM, weak, strong
d_L	$1/2$	$-1/2$	$+1/3$	$+2/3$	EM, weak, strong
u_R	0	0	$+4/3$	$+2/3$	EM, weak, strong
d_R	0	0	$-2/3$	$-1/3$	EM, weak, strong

Table 1.1: The fermions of the Standard Model organized in doublets or singlets for the three generations. l stands for e, μ and τ; u for u,c and t quarks; d for d,s and b quarks.

Bosons	Mass	Charge	Interaction
γ (photon)	0	0	EM
g_i (gluons)	0	0	strong
$W^{\pm}$, Z	80.4 and 91.2 GeV	± 1, 0	weak
h (higgs)	? (> 119 GeV)	0	gives masses to the SM particles

Table 1.2: The bosons of the Standard Model.

We need a mechanism to give the right mass to the elementary particles described by SM as listed in tab. 1.1 and tab. 1.2. The generally accepted and satisfactory solution to this problem has been found by P.W.Higgs [1] and his method called Higgs mechanism.

1.2 The Higgs mechanism

The Higgs mechanism assumes that all SM particles are initially massless and acquire masses by interacting with a new scalar field, Φ, generated by a massive new particle called higgs boson. This field is a $SU(2)$ doublet (with hypercharge $Y = +1$) containing two complex scalars leading to four degrees of freedom in total. When we introduce in the SM lagrangian the field Φ with its kinetic and potential terms

$$\mathcal{L}_{kin}^{Higgs} = \left(D_\mu \Phi^\dagger\right)\left(D^\mu \Phi\right)$$

$$\mathcal{L}_{pot}^{Higgs} = \mu^2 \Phi^\dagger \Phi - \lambda \left(\Phi^\dagger \Phi\right)^2$$

where D^μ is covariant derivative, the vacuum expectation value (VEV) of the higgs field will keep a non-zero value (namely $v = \sqrt{-\mu^2/\lambda}$). The scalar potential will therefore have its global minimum away from zero (cfr. fig. 1.1) so that the symmetry is spontaneously broken. At this

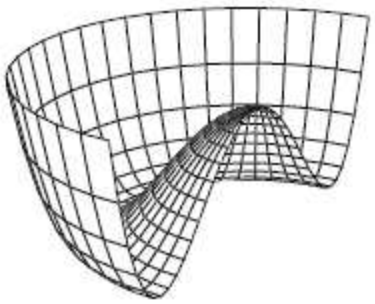

Figure 1.1: Higgs potential

point the gauge bosons naturally acquire mass terms from $\mathcal{L}_{kin}^{Higgs}$ and they result to be proportional to the vacuum expectation value; moreover, by putting the mass matrix into diagonal form, we can obtain the more familiar mass eigenstates of the massive vector bosons $W^\pm$, Z and of the massless photon. In this way 3 out of the 4 degrees of freedom are *eaten* to give the right masses to the massive bosons and the remaining degree of freedom represents the still undiscovered physical higgs boson h.

Finally, it is necessary to introduce some extra terms in the SM lagrangian to generate the fermion masses:

$$-\mathcal{L}^{Higgs}_{fermion-coupling} = \sum_{Y_f+Y_{f'}+Y_\Phi=0} \bar{\psi}^L_f C_{ff'} \Phi \psi^R_{f'} + h.c. + \sum_{Y_f+Y_{f'}+Y_{\Phi*}=0} \bar{\psi}^L_f C'_{ff'} i\sigma_2 \Phi * \psi^R_{f'} + h.c.$$

where $\psi^{R,L}_f = \frac{1}{2}(1 \pm \gamma_5)\,\psi$ are the left,right-handed components of the fermion fields and $C_{ff\prime}$,$C\prime_{ff\prime}$ are known as Yukawa couplings.

1.3 Motivations for Supersymmetry

The Standard Model is a good theory which has a lot of excellent agreements with experiments but it, however, does not include the gravity which plays a central role in the universe. So SM can be considered as an approximation at low energy scale of a more fundamental theory and it is possible to constrain it to be valid up to the Planck scale ($\Lambda \sim 10^19$ GeV) where gravitational effects could take place. Moreover, as previously mentioned, the Higgs boson has not been discovered yet and this is one of the goals of the new experiments particularly at **L**arge **H**adron **C**ollider (LHC). Since the Higgs mass is a parameter of the theory it can, in principle, take any value. But some theoretical reasonings (such as the study of unitarity limits for WW scattering) suggest us that the renormalized Higgs mass is constrained to be below ~ 1 TeV. Furthermore, the global fits of electroweak parameters on existing LEP data favour the existence of a light Higgs Boson as shown in fig. 1.2.

Some problems rise when we consider the one-loop radiative corrections to the Higgs mass: in fact if the Higgs field couples to fermions (f) with a term in the lagrangian $-\lambda_f h \bar{f} f$, then, using the Feynman diagram in fig. 1.3 (a) we get the following expression:

$$\Delta m^2_{h_f} = \frac{|\lambda_f|^2}{16\pi^2}[-2\Lambda^2_{UV} + 6m^2_f \ln(\Lambda_{UV}/m_f) + ...] \tag{1.1}$$

where Λ_{UV} is the cutoff scale and f can be any quark or lepton. The corrections to the Higgs mass are, therefore, quadratically divergent as $\Lambda_{UV} \to \infty$. If we set the SM to be valid up to the Planck scale (10^{19}) then the bare Higgs-mass-squared is forced, by means of a fine tuning of some 30 order of magnitude, to the same scale, in order to keep the renormalized Higgs mass ($m_h \simeq m^0_h + \Delta m_{h_f}$) $\lesssim 1$ TeV. This is known as "naturalness problem" and the Supersymmetry (SUSY) provides an elegant solution to it as we will see in the next section.

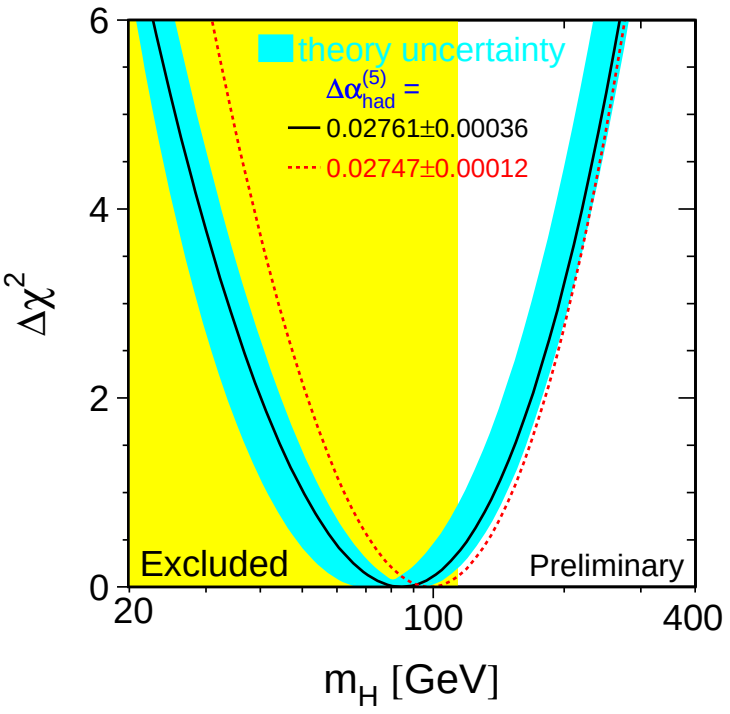

Figure 1.2: Global fit of m_H using all electroweak data [4].

1.4 Supersymmetry

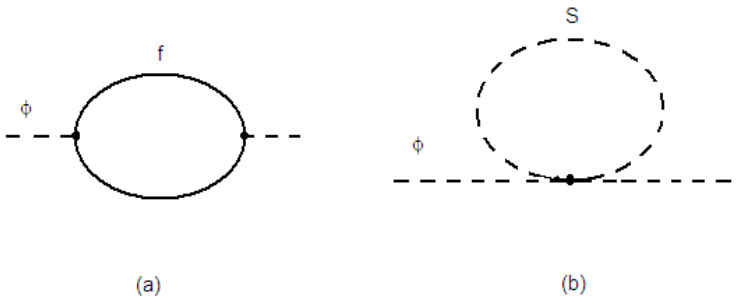

Figure 1.3: One loop diagram: (a) fermion-Higgs one loop; (b) scalar-Higgs one loop.

If we consider the Feynman diagram as in fig. 1.3 (b) representing a one-loop correction to the

Higgs mass with a h-S-S coupling, we get:

$$\Delta m_{\phi_S}^2 = \frac{\lambda_S}{16\pi^2}[\Lambda_{UV}^2 - 2m_S^2 \ln(\Lambda_{UV}/m_S) + ...] \tag{1.2}$$

Again we have a quadratic divergence (as $\Lambda_{UV} \to \infty$) but this time the scalar fields S contributes to the corrections (in the Λ_{UV} factor) with an opposite sign (the relative minus sign is due to the Fermi spin statistics) compared with the fermion loop in fig. 1.3 (a). So we can imagine that each of the quarks and leptons of the Standard Model are associated with two scalar fields in such a way to cancel the dangerous quadratic divergences, if it is assumed $\lambda_S = |\lambda_f|^2$. Nevertheless, in order for this cancellation to persist to all orders in perturbation theory, it must be the result of a symmetry relating fermions and bosons. Such a symmetry is known as Supersymmetry and an its transformation turns a boson state into a fermion state and vice versa; the operator Q generating these transformations:

$$Q|fermion\rangle = |boson\rangle \quad Q|boson\rangle = |fermion\rangle \tag{1.3}$$

is a fermion operator carrying spin $1/2$ and verifying the following algebra relations:

$$\{Q, Q^\dagger\} \sim P^\mu \tag{1.4}$$

$$\{Q, Q\} = \{Q^\dagger, Q^\dagger\} = 0 \tag{1.5}$$

$$[P^\mu, Q] = [P^\mu, Q^\dagger] = 0 \tag{1.6}$$

where P^μ is the momentum generator of space-time translations. It is possible to arrange the single-particle states in irreducible representations of the SUSY algebra called supermutiplets and, since SUSY generators commute with gauge generators and with $-P^2$, the members in a multiplet have the same quantum numbers (charge, weak-isospin, color) and the same masses. Moreover it can be shown (see for instance [2]) that in each of the multiplets the number of fermion degrees of freedom must be equal to the number of boson degrees of freedom ($n_f = n_b$). The simplest ways to build a supermultiplet are just two:

- a single Weyl fermion ($n_f = 2$, due to the two helicity states) is assembled with two real scalars (or better with a complex scalar), each with $n_b = 1$. It is called chiral or matter supermultiplet;

- a massless spin 1 boson (again two helicity states, so $n_b = 2$) can be assembled with a spin $1/2$ Weyl fermion (with two helicity states). It is known as gauge or vector supermultiplet;
- any other combination of particles can always be reduced to chiral or gauge supermultiplets[2].

In summary, in a supersymmetric extension of the Standard Model, each of the SM elementary particles must therefore be assembled in either a chiral or gauge supermultiplet and has a superpartner differing in the spin by a factor $1/2$ and with the same quantum numbers and masses. These particles form their names from the ones of the SM partners: namely the spin 0 partners of quarks and leptons are called squarks and sleptons (prefix "s" stands for scalar) respectively; the spin $1/2$ partners of gauge bosons are called gauginos (suffix "ino" to the name of corresponding SM particle).

1.5 MSSM

The MSSM (**M**inimal **S**upersymmetric **S**tandard **M**odel) is the simplest model containing the smallest possible number of new particles into the theory. As in the Standard Model, the particle states can be either left-handed doublets or right-handed singlets and, as previously mentioned, the elementary particles are organized, together with their superpartners whose spin differ by half a unit, into supermultiplets. The SUSY lagrangian cannot contain arbitrary terms since the allowed interactions between SM particles and their supersymmetric partners are given. Nevertheless the general SUSY lagrangian depends on a function $W(\Phi)$ (Φ is a chiral superfield) called superpotential that is allowed to change. In the tables 1.3 and 1.4 are listed the MSSM chiral and gauge supermultiplets.

As already said, in each supermultiplet, the supersymmetric particles have the same masses than the corresponding SM particles; it is clear, then, that supersymmetry must be a broken symmetry. Indeed it is evident that it has not been observed yet any scalar particles with the mass and quantum numbers of the electron or muon. On the other hand, such a supersymmetry breaking must be a "soft" breaking in order to still preserving the cancellation of all quadratic divergences (that was one of the reasons pushing us to introduce SUSY). The masses of quarks and leptons are obtained

[2]this is true for non-extended supersymmetry, that is when $N = 1$, N referring to the number of supersimmetries (the number of distinct copies of Q,$Q^\dagger$ operators)

Name ($\times 3 families$)	spin 0	spin 1/2	$SU(3)_C \times SU(2)_L \times U(1)_Y$
squarks, quarks:			
Q	$(\tilde{u}_L\, \tilde{d}_L)$	$(u_L\, d_L)$	(**3**, **2**, $\frac{1}{6}$)
$\bar{u}$	$\tilde{u}_R^*$	$u_R^\dagger$	($\bar{\mathbf{3}}$,**1**, $-\frac{2}{3}$)
$\bar{d}$	$\tilde{d}_R^*$	$d_R^\dagger$	($\bar{\mathbf{3}}$,**1**, $\frac{1}{3}$)
sleptons, leptons:			
L	$(\tilde{\nu}\, \tilde{e}_L)$	$(\nu\, e_L)$	(**1**, **2**, $-\frac{1}{2}$)
$\bar{e}$	$\tilde{e}_R^*$	$e_R^\dagger$	(**1**, **1**, 1)
Higgs, Higgsinos:			
H_u	$(H_u^+\, H_u^0)$	$(\tilde{H}_u^+\, \tilde{H}_u^0)$	(**1**, **2**, $+\frac{1}{2}$)
H_d	$(H_d^0\, H_d^-)$	$(\tilde{H}_d^0\, \tilde{H}_d^-)$	(**1**, **2**, $-\frac{1}{2}$)

Table 1.3: Chiral supermultiplets in the MSSM model.

Name	spin 1/2	spin 1	$SU(3)_C \times SU(2)_L \times U(1)_Y$
gluinos,gluons	$\tilde{g}$	g	(**8**, **1**, 0)
winos, W	$\tilde{W}^\pm\ \tilde{W}^0$	$W^\pm\ W^0$	(**1**, **3**, 0)
bino, B	$\tilde{B}^0$	B^0	(**1**, **1**, 0)

Table 1.4: Gauge supermultiplets in the MSSM model.

by the following superpotential:

$$W_{MSSM} = y_u^{ij} \bar{u}_i Q_j H_u - y_d^{ij} \bar{d}_i Q_j H_d - y_e^{ij} \bar{e}_i L_j H_d + \mu H_u H_d, \tag{1.7}$$

where H_u, H_d, Q, L, $\bar{u}$, $\bar{d}$, $\bar{e}$ are the chiral supermultiplets listed in tab. 1.3, the y_u^{ij}, y_d^{ij}, y_e^{ij} (3×3 matrices in the family space) are the Yukawa couplings of the Standard Model and μ is the mass parameter. It is interesting to note (see table 1.3) that there are two complex scalar Higgs doublets (with hypercharge equal ± 1) in MSSM instead of just one as in the Standard Model: in fact in MSSM, since the superpotential must be analytic (it is a holomorphic function of Φ_i, that is it depends only on Φ_i, not on Φ_i^*), neither terms like $\bar{u} Q H_d^*$ nor like $\bar{d} Q H_u^*$ and $\bar{e} L H_u^*$[3] are allowed

[3] In the Standard Model we have

$$\mathcal{L}_{SM} = m_d \bar{Q}_L H d_R + m_u \bar{Q}_L \tilde{H} u_R$$

so that both the Higgs doublets are necessary[4]. Now it still remains the problem to give masses to supersymmetric partners of SM particles; actually there are two ways to do this: either by adding explicitly the "soft" terms in the lagrangian or, as for Standard Model, by using a spontaneous symmetry breaking approach. The latter one is not possible in MSSM without extending the model itself so one can insert the following terms in the lagrangian [3]:

$$\begin{aligned}\mathcal{L}_{soft}^{MSSM} = &-\frac{1}{2}\left(M_3\tilde{g}\tilde{g} + M_2\tilde{W}\tilde{W} + M_1\tilde{B}\tilde{B}\right) + c.c. \\ &-\left(\tilde{\bar{u}}\mathbf{a_u}\tilde{Q}H_u - \tilde{\bar{d}}\mathbf{a_d}\tilde{Q}H_d - \tilde{\bar{e}}\mathbf{a_e}\tilde{L}H_d\right) + c.c. \\ &-\tilde{Q}^\dagger\mathbf{m_Q^2}\tilde{Q} - \tilde{L}^\dagger\mathbf{m_L^2}\tilde{L} - \tilde{u}\mathbf{m_{\bar{u}}^2}\tilde{\bar{u}}^\dagger - \tilde{\bar{d}}\mathbf{m_{\bar{d}}^2}\tilde{\bar{d}}^\dagger - \tilde{\bar{e}}\mathbf{m_{\bar{e}}^2}\tilde{\bar{e}}^\dagger \\ &-m_{H_u}^2 H_u^* H_u - m_{H_d}^2 H_d^* H_d - (bH_u H_d + c.c.)\,, \end{aligned} \tag{1.8}$$

where M_1, M_2, M_3 are the bino, wino and gaugino masses respectively, m_{H_u}, m_{H_d} the Higgs doublets masses, the bold term are 3×3 matrices in the family space, b a parameter[5].

Supersymmetry breaking and EW breaking are correlated in MSSM, so the latter can take place only after the former. In a very similar way as for Standard Model, even if a little bit more complicated because of the two complex Higgs doublets, it can be shown that after the symmetry breaking three out of the eight degrees of freedom are eaten to give the right masses to gauge bosons; the remaining degrees of freedom represent five physical states: two neutral Higgses (h, H), two charged Higgses ($H_\pm$) and a pseudo scalar (A) Higgs. Furthermore, neutral higgsinos and neutral gauginos mix to generate four neutral particles called neutralinos; charged higgsinos and winos mix to give two particles (each with two possible charges) called charginos. The table 1.5 shows the complete list of MSSM particles after SUSY breaking.

Before going on it is useful to introduce the concept of R-parity. The considered superpotential $W(\Phi)$ in 1.7 is not the most general choice one can do but it is possible to include terms violating

---

where $\tilde{H} = i\sigma_2 H^\dagger$.

[4]Two doublets needed also for cancellation of triangle gauge anomalies.

[5]In order for all parameters to be "soft" it must be:

$$M_1, M_2, M_3, \mathbf{a_u}, \mathbf{a_d}, \mathbf{a_e} \sim m_{soft}$$

and

$$\mathbf{m_Q^2}, \mathbf{m_L^2}, \mathbf{m_{\bar{u}}^2}, \mathbf{m_{\bar{d}}^2}, \mathbf{m_{\bar{e}}^2}, m_{H_u}^2, m_{H_d}^2, b \sim m_{soft}^2,$$

with $m_{soft} \sim$1 TeV.

Names	Mass eigenstates	Gauge eigenstates	Spin
Sleptons	$\tilde{e}_L$,$\tilde{\nu}_{eL}$,$\tilde{e}_R$ $\tilde{\mu}_L$,$\tilde{\nu}_{\mu L}$,$\tilde{\mu}_R$ $\tilde{\tau}_1$,$\tilde{\tau}_2$,$\tilde{\nu}_{\tau L}$	$\tilde{e}_L$,$\tilde{\nu}_{eL}$,$\tilde{e}_R$ $\tilde{\mu}_L$,$\tilde{\nu}_{\mu L}$,$\tilde{\mu}_R$ $\tilde{\tau}_L$,$\tilde{\tau}_R$,$\tilde{\nu}_{\tau L}$	0
Squarks	$\tilde{u}_L$,$\tilde{d}_L$,$\tilde{u}_R$,$\tilde{d}_R$ $\tilde{s}_L$,$\tilde{c}_L$,$\tilde{s}_R$,$\tilde{c}_R$ $\tilde{t}_1$,$\tilde{t}_2$,$\tilde{b}_1$,$\tilde{b}_2$	$\tilde{u}_L$,$\tilde{d}_L$,$\tilde{u}_R$,$\tilde{d}_R$ $\tilde{s}_L$,$\tilde{c}_L$,$\tilde{s}_R$,$\tilde{c}_R$ $\tilde{t}_L$,$\tilde{t}_R$,$\tilde{b}_L$,$\tilde{b}_R$	0
Higgs bosons	h,H,A,$H^{\pm}$	H_u^0, H_d^0,H_u^+,H_d^-	0
Gluinos	$\tilde{g}$	$\tilde{g}$	1/2
Charginos	$\tilde{\chi}_1^{\pm}$,$\tilde{\chi}_2^{\pm}$	$\tilde{W}^{\pm}$, $\tilde{H}_u^+$,$\tilde{H}_d^-$	1/2
Neutralinos	$\tilde{\chi}_1^0$,$\tilde{\chi}_2^0$,$\tilde{\chi}_3^0$, $\tilde{\chi}_4^0$	$\tilde{B}^0$,$\tilde{W}^0$, $\tilde{H}_u^0$,$\tilde{H}_u^0$	1/2
Gravitino/Goldstino	$\tilde{G}$	$\tilde{G}$	3/2

Table 1.5: Particle states in MSSM including gravitino

the conservation of lepton and baryon number like

$$W_{\Delta L=1} = \frac{1}{2}\lambda^{ijk} L_i L_j \bar{e}_k + \lambda^{'ijk} L_i Q_j \bar{d}_k + \mu^{'i} L_i H_u$$

$$W_{\Delta B=1} = \lambda^{''ijk} \bar{u}_i \bar{d}_j \bar{d}_k$$

where, unlike the Standard Model, there is not a gauge invariance protecting this conservation. In order to prevent these terms in the lagrangian one can postulate the conservation of a new symmetry called R-parity defined as it follows:

$$R_p = (-1)^{3(B-L)+2s} \tag{1.9}$$

where B, L are respectively the baryon, lepton number and s the spin. In this way all SM particles

have $R_p = +1$, all supersymmetric particles have $R_p = -1$ and, since R-parity is a multiplicative quantum number, there are interesting consequences, if it is conserved:

- in collider experiments the supersymmetric particles will always be produced in even number;
- the **L**ighest **S**upersymmetric **P**article (LSP) must be stable (if electrically neutral can interact only weakly with the matter resulting a good candidate for non-baryonic dark matter; experimentally it behaves just like a neutrino escaping undetected and resulting in a big amount of missing energy thanks to its mass);
- each supersymmetric particle can decay in an odd number of lighter supersymmetric particles.

In R-parity violating theories it is easier to confer masses to neutrinos (with lepton violating terms) but the analysis will result much more complex since the supersymmetric particles can fully decay into SM particles.

1.6 mSUGRA

The supersymmetry breaking has been introduced explicitly (soft breaking) in the MSSM lagrangian but we do not know anything about where these terms come from. We need a spontaneous supersymmetry breaking to explain that but, unfortunately, this does not work with the only MSSM fields. We must hypothesize that the spontaneous SUSY breaking happens into an hidden sector and then communicated, by flavour-blind interactions, to the visible sector (the MSSM) generating the previously discussed “soft” terms (see fig. 1.4).

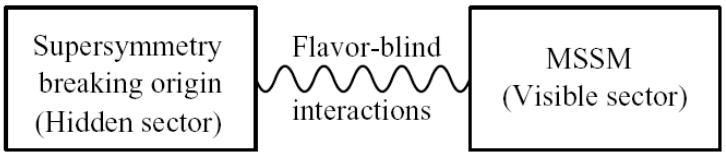

Figure 1.4: Supersymmetry spontaneous breaking scheme.

There are essentially two possible ways to connect the hidden and visible sectors: supersymmetry breaking mediated by either gravity or gauge bosons. An example of the former model is the so-called **mi**nimal **SU**per**GRA**vity model (mSUGRA) where the hidden and visible sectors interact only gravitationally by means of graviton. Spontaneous supersymmetry breaking therefore leads to a super Higgs mechanism which is able to give mass to the superpartner of the graviton known as gravitino. At an energy scale much lower than the Planck scale the two sectors decouple (since the gravitational interactions get too low) and the spontaneous breaking becomes like a soft breaking with non-renormalizable terms.
A very useful feature of mSUGRA is that, if one assumes a minimal form at the Planck scale, then the number of free parameters drastically decreases (after supersymmetry breaking in MSSM there are 105 free parameters) to just five parameters:

- the masses of scalar particles unify at some high energy scale (GUT or Planck scale) to the common scalar mass m_0;
- the masses of fermion particles unify at some high energy scale (GUT or Planck scale) to the common fermion mass $m_{\frac{1}{2}}$;
- the trilinear couplings unify at some high energy scale (GUT or Planck scale) to the common trilinear coupling A_0;
- the ratio of Higgs VEVs $\tan\beta$;
- the sign of μ parameter $sgn(\mu)$.

In order to obtain the right MSSM mass spectrum, for instance at the EW scale, one must evolve the parameters using the Renormalization Group Equations (RGE) to the weak scale (cfr. for instance fig. 1.5).

Furthermore considering how the coupling constants [2] evolve as a function of the energy scale (with one loop corrections)

$$\frac{1}{\alpha_i(Q)} = \frac{1}{\alpha_i(M)} + \frac{b_i}{2\pi}\log(\frac{M}{Q}),$$

where $i = 1, 2, 3$, $\alpha_1, \alpha_2, \alpha_3$ are the electromagnetic, weak and strong coupling constants respectively and b_i a parameter, it is possible to verify (cfr. fig. 1.6) that there is a much better unification

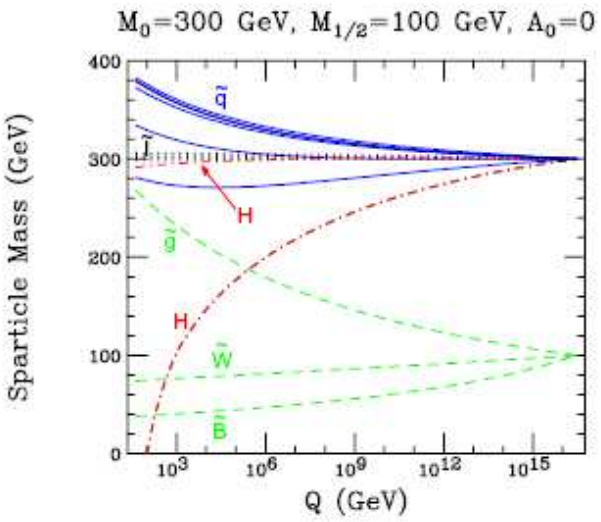

Figure 1.5: Evolution performed through renormalization group equations: running of masses as a function of the energy scale for $m_0 = 300$ GeV, $m_{1/2} = 100$ GeV, $A_0 = 0$.

of the coupling constants in this case compared with the Standard Model case: this is another success of Supersymmetry.

As a last observation, mSUGRA is a $R-parity$ conserving model so that the LSP must be stable: LSP is assumed to be the first neutralino $\tilde{\chi}_1^0$, which is a neutral, weak interacting, massive particle, considered a good candidate for the non-barion dark matter.

1.7 Mass spectrum and decays

Here it will be described some features of MSSM physics, assuming the conservation of $R-parity$ and identifying the LSP as $\tilde{\chi}_1^0$.

Neutralinos

After the supersymmetry breaking mechanism the neutral fields $\tilde{H}_u^0$, $\tilde{H}_d^0$ (higgsinos) and $\tilde{W}^0$ e $\tilde{B}$

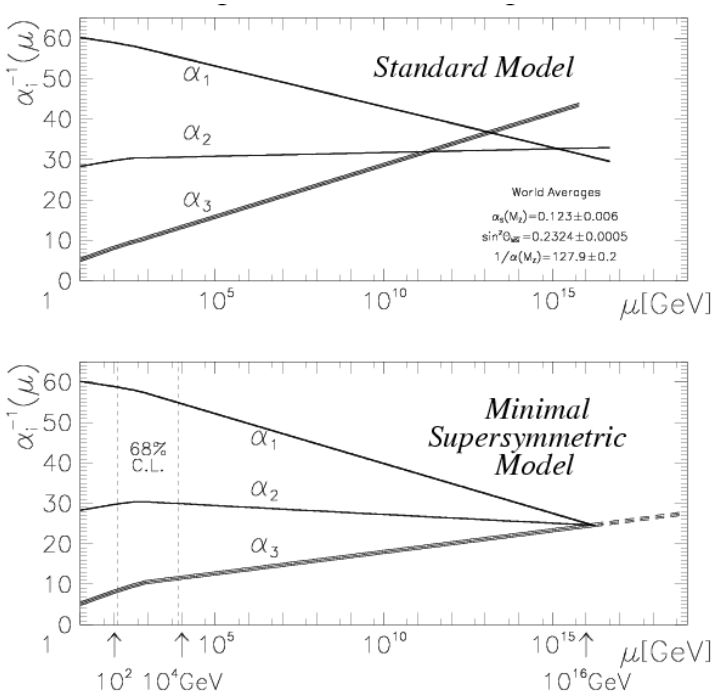

Figure 1.6: Running of coupling constants α_1, α_2, α_3 respectively for electromagnetic, weak and strong interactions as a function of the mass scale. The top plot shows the running in the Standard Model, the bottom one shows the same for the Minimal Supersymmetric Standard Model.

(gauginos) are mixed by a 4×4 non-diagonal matrix. The diagonalization of such a matrix gives four new neutral physical states, $\tilde{\chi}_i^0$ $i = 1, 2, 3, 4$ with $m_{\tilde{\chi}_1^0} < m_{\tilde{\chi}_2^0} < m_{\tilde{\chi}_3^0} < m_{\tilde{\chi}_4^0}$, called neutralinos. They inherit their weak couplings to fermion-scalar pairs from the gaugino component and the both gaugino-higgsino-Higgs and gaugino-gaugino-vector boson couplings from the higgsino component. Some of possible decays are:

$$\tilde{\chi}_i^0 \to Z\tilde{\chi}_j^0,\ W\tilde{\chi}_j^{\pm},\ h_0\tilde{\chi}_j^0,\ l\tilde{l},\ \nu\tilde{\nu};$$

and, even if with a lower probability, decays with the following final states:

$$A_0\tilde{\chi}_j^0,\ H^0\tilde{\chi}_j^0,\ H^{\pm}\tilde{\chi}_j^{\pm},\ e\,q\tilde{q}$$

If these decays are kinematically suppressed then three body decays can be opened.

Charginos

From the mixing of ($\tilde{W}^+$,$\tilde{H}_u^+$) and ($\tilde{W}^-$,$\tilde{H}_u^-$) pairs one gets two positive and two negative physical

states called charginos and denoted as $\tilde{\chi}_i^{\pm}$ where $i = 1, 2$. Also in this case, as for neutralinos, they inherit their couplings from gaugino and higgsino components, so some of possible decays are:

$$\tilde{\chi}_i^{\pm} \to W\tilde{\chi}_j^0,\ Z\tilde{\chi}_1^{\pm},\ h_0\tilde{\chi}_1^{\pm},\ l\tilde{\nu},\ \nu\tilde{l},$$

the less probable ones

$$A_0\tilde{\chi}_1^{\pm},\ H^0\tilde{\chi}_1^{\pm},\ H^{\pm}\tilde{\chi}_j^0,\ e\,q\tilde{q}$$

and three body decays when possible.

Gluinos

The eight gluinos are not mixed and the two body decays, $\tilde{g} \to q\tilde{q}$, are dominant, if kinematically allowed, otherwise they decay through off shell squarks in processes like

$$\tilde{g} \to qq'\tilde{\chi}_i^0,\ qq'\tilde{\chi}_i^{\pm}.$$

Generally the gluinos generate very long cascade decays, always terminating with a $\tilde{\chi}_1^0$, whose branching ratios significantly depend on the parameters of the model.

Squarks and Leptons

Both sleptons and squarks exist in either right-handed or left-handed state[6] (except for sneutrinos having only the left-handed states) even if for the third family of squarks and sleptons these components mix to form new physical states (cfr. tab. 1.5). The rest of sfermions do not mix significantly. Sleptons decay mainly to leptons and charginos/neutralinos

$$\tilde{l} \to l\tilde{\chi}_i^0,\ \nu\tilde{\chi}_i^{\pm},\ \tilde{\nu} \to \nu\tilde{\chi}_i^0,\ l\tilde{\chi}_i^{\pm};$$

where the direct decays $l\tilde{\chi}_1^0$ is always kinematically allowed if $\tilde{\chi}_1^0$ is the LSP and it is favoured by right-handed sleptons (since they do not have couplings to $SU(2)_L$ gauginos) if the latter is bino-like. For what concerns the squarks the decays to $q\tilde{g}$ are preferred, if kinematically allowed, otherwise $\tilde{q} \to q\tilde{\chi}_2^0,\ q'\tilde{\chi}_1^{\pm}$ decays can be opened.

In figure 1.7 it is possible to see an example of mass spectrum for a particular point in the parameter space of mSUGRA model. In short, general considerations on masses are:

- the lightest supersymmetric particle is identified with the $\tilde{\chi}_1^0$ unless it is the gravitino or in the models violating the R-parity. Furthermore if $\mu < M_1, M_2$ the first neutralino is mostly

[6] Being sleptons and squarks scalar particles they have spin-0. So right-handed and left-handed states indicate only which SM particles they are associated to.

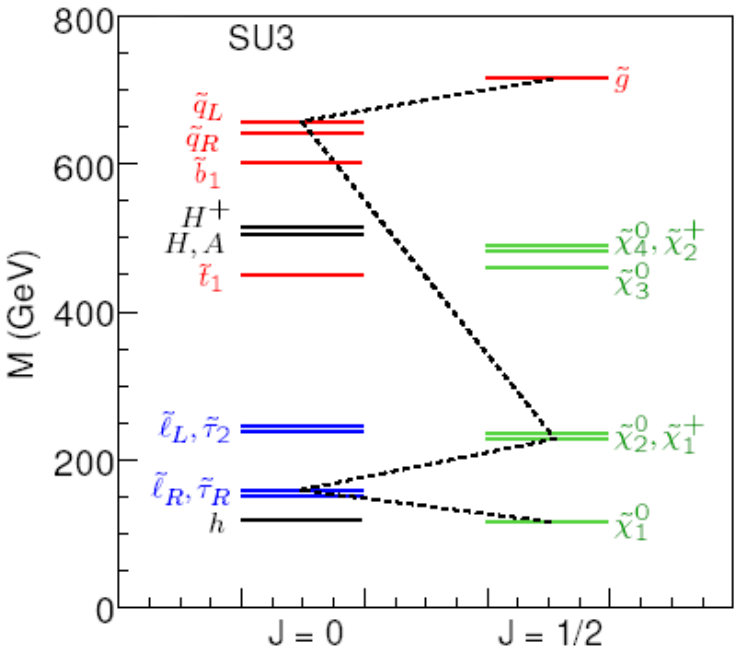

Figure 1.7: An example of supersymmetric particle mass spectrum. It refers to SU3 which is one of the benchmark points chosen by ATLAS collaboration to study the Supersymmetry.

bino-like (mostly $\tilde{B}$) and its mass is about half of $\tilde{\chi}_2^0$ and $\tilde{\chi}_1^\pm$ masses; in the contrary case it is mostly higgsino-like (mostly $\tilde{H}$) and its mass is comparable with those masses;

- the gluino mass is much greater than neutralinos and charginos masses;
- squarks belonging to the first two families are mass degenerate and much heavier than sleptons; their masses are not lower than 0.8 times the gluino mass. Furthermore left-handed squarks are heavier than corresponding right-handed ones.
- $\tilde{t}_1$ and $\tilde{b}_1$ get small masses in comparison with all of the other squarks;
- the lightest charged slepton is τ_1;
- sleptons e_L and μ_L are heavier than corresponding right-handed;
- the lightest Higgs boson, h, must have a mass less than 150 GeV.

Chapter 2

The ATLAS Experiment

In this chapter we will, first the Large Hadron Collider (LHC), the most powerful particles accelerator of all times. A description of the whole experimental apparatus and the details of specific detecors will be given. At the end we will deal with the muon trigger system and its different levels.

2.1 The Large Hadron Collider

The **L**arge **H**adron **C**ollider (LHC) [9, 10] is the highest energy and the highest luminosity particles accelerator ever built. Its construction at CERN (*"Conseil Europeen pour la Recherche Nucleaire"*), in the existing 26.7 Km tunnel previously used for the LEP (**L**arge **E**lectron **P**ositron) collider, should be completed by 2007. LHC will provide *proton-proton* as well as heavy ions collisions. The LHC features, which make it the most powerful accelerator in the world, are mainly three : *Luminosity, Energy* and *Bunch Crossing rate*.

- **Luminosity**
  After a first period of optimization at *Low luminosity* (10^{33} cm^{-2}s^{-1}), the accelerator will reach the value of 10^{34} cm^{-2}s^{-1} that will make possible to study even physics processes with very low cross sections and to store up a large amount of statistics. The LHC design

luminosity $\mathcal{L}$ is defined as

$$\mathcal{L} = f\frac{n_1 n_2}{4\pi\sigma_x\sigma_y} \tag{2.1}$$

where n_1 and n_2 are the number of protons per colliding bunches, f is the collision frequency, σ_x and σ_y characterize the Gaussian transverse profiles in the horizontal (bend) and vertical directions.

- **Energy**
  LHC will reach the center-of-mass energy of 14 TeV that is an order of magnitude greater than any previous collider and it will make possible to investigate new physics sectors. LHC will use extensively the already existing infrastructures to produce, store and accelerate the protons; a layout of the LHC injection scheme is shown in figure 2.1.

  Proton acceleration start in the 50 MeV proton linac, followed by injection into the 1.4 GeV Proton Synchrotron Booster (PSB). The Proton Synchrotron (PS) itself will accelerate the protons to 26 GeV and deliver a beam of 135 bunches, containing 10^{11} protons, spaced by 25 ns. Then the Super Proton Synchrotron (SPS) will accelerate the particles up to 450 GeV, and finally they will be injected into the LHC to be boosted up to 7 TeV. The head-on collision will provide, besides the proton-proton collision also $^{201}Pb_{82} -^{201} Pb_{82}$ collision with center-of-mass energy of 1262 TeV.

- **Bunch Crossing**
  The proton beam will be bunched with a crossing frequency of 40 MHz corresponding to 25 ns of time spacing. Due to this high rate, a great technology effort has been necessary to synchronize all sub detectors read-out in the time of 1-2 ns. Considering a $\sigma(pp) \approx 70$ mb, at *High luminosity*, it will be possible to have an interaction rate of about 10^9 Hz, corresponding to $\sim$23 interactions per crossing.

In the LHC design the proton-proton collisions have been preferred to proton-antiproton ones because to reach similar luminosity with antiprotons is very difficult. A drawback of this choice, with respect to the case of SPS and LEP where the same magnets were used to keep in orbit particles and antiparticles, is that the two beams of equally charged particles must circulate in separate and opposite magnetic fields. A solution to this problem was found using a twin-aperture magnet with two coils and beam channels using the same mechanical structure and cryostat (fig. 2.2).

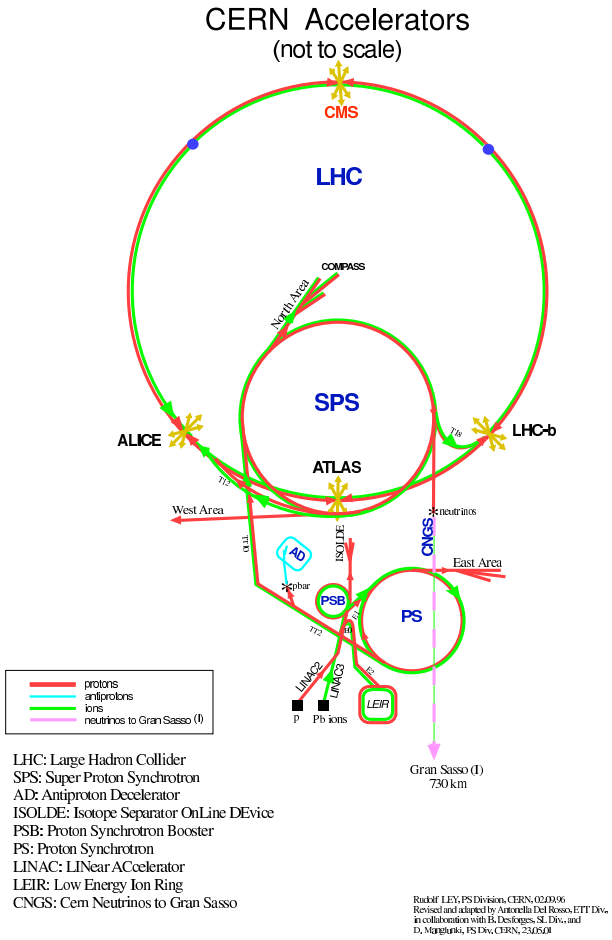

Figure 2.1: Injection scheme for LHC.

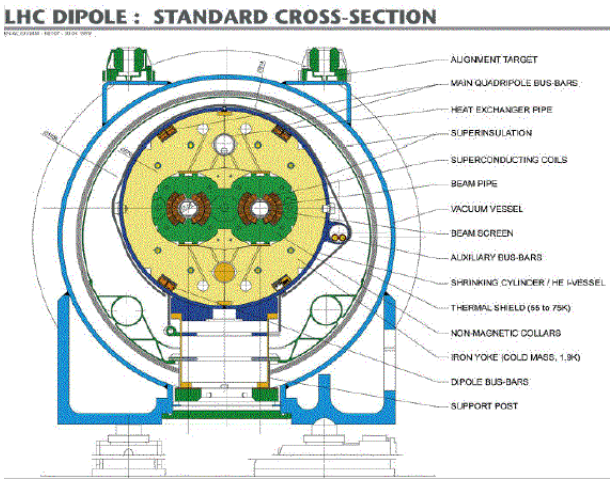

Figure 2.2: Schematic view of a twin-bore magnet for the LHC.

The two beam channels lie side by side, 194 mm apart, in the cold yokes of the main dipole and quadrupole magnets. This twin-aperture arrangement has enabled a cost saving of 30% compared to two separate magnets as well as solving the obvious space problem.

In order to bend the proton beams around the LEP tunnel the magnetic fields need to be of about 9 T. This high magnetic field can only be produced with superconducting magnets at very low temperatures. Up to now superconducting magnets have been cooled down to *only* 4.2 K to reach fields of 5.5 T. To go beyond this field strength, LHC magnets will need to be cooled with superfluid Helium at 1.9 K. At this temperature superfluid Helium has greater heat conductivity and lower viscosity which will allow the magnets to achieve higher fields.

To keep the required temperature value there is a need for a cryogenics plant with a total cooling power of 144 kW equivalent capacity at 4.5 K. This will be provided by eight cryoplants of 18 kW each. Four of them were already used by LEP but their capacity needs to be increased from 12 to 18 kW.

In the LHC, there will be a total of 3444 superconducting magnet units. These include 1232 main dipole magnets and 386 main quadrupole magnets of twin-aperture design. Small correctors (4928) will be added to the main dipoles bringing the total to about 8400 units of different sizes. In addition to these superconducting magnets there will be, also, a number of room temperature magnets. In the four octants of the LEP tunnel the machine utilities such as acceleration, beam

Parameter	Value
Luminosity	10^{34} cm^{-2} s^{-1}
Beam energy	7.0 TeV
Dipole field	8.33 T
Coil aperture	56 mm
Distance between aperture axes (1.9 K$^{\circ}$)	194 mm
Injection energy	450 GeV
DC Beam	0.56 A
Bunch separation	25 ns
Bunch spacing	7.48 m
Particles per bunch	1.1×10^{11}
Stored beam energy	350 MJ
Normalized transverse emittance	3.75 μrad
R.M.S. bunch length	75 mm
Filling time x ring	4.3 min
Luminosity lifetime	10 h
Energy loss per turn	7 keV
Critical photon energy	44.1 eV
Total radiated power per beam	3.8 kW

Table 2.1: Main parameters of the LHC

cleaning and beam dumping systems will be placed. The beam dumping system itself is a very crucial point and for this reason it has been carefully designed and built. In fact, at the highest luminosity of the LHC, the stored beam energy will be about 350 MJ. This energy must be absorbed safely at the end of each run or in case of a malfunction or an emergency. Classical beam dumps, made of a central graphite core surrounded by aluminum and iron blocks, and located at the end of two fast vertical extraction channels, have been designed for this purpose. A summary of the LHC design parameters for p-p collisions is given in table 2.1.

The LHC will be installed in the eight fold symmetry LEP tunnel but, as can be seen from fig.2.3 only four octancts will be used for experiments. The beams will cross in four points where the physics experiments will be situated. The previous considerations on LHC imposed very stringent

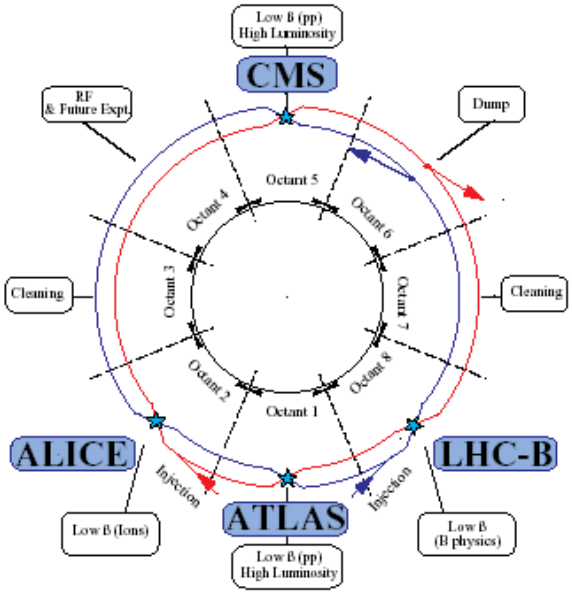

Figure 2.3: Schematic layout of the LHC octants

requirements on the detector design, in particular above all the high flux coming from the proton-proton collisions. Therefore only devices with an high radiation hardness level can be used in the construction of the LHC experiments. The experiments approved and under construction are four:

- ATLAS, A Toroidal LHC ApparatuS [11]
- CMS, Compact Muon Solenoid [12]
- ALICE, A Large Ion Collider Experiment [14]
- LHCb, Large Hadron Collider bPhysics [13]

the first two listed are general purpose experiments while **ALICE** and **LHCb** are dedicated to heavy-ion physics and to b-physics respectively. The **ATLAS** experiment will be widely described in details in the next section.

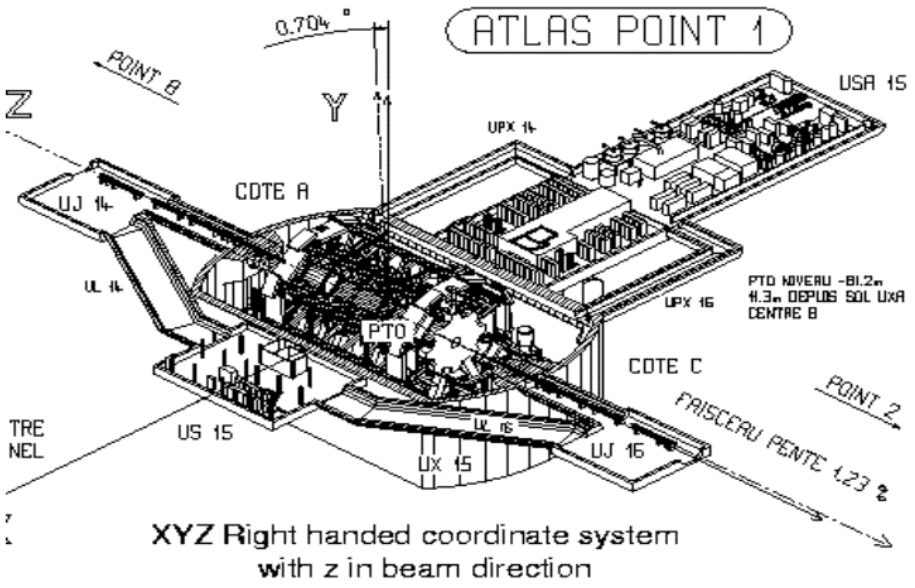

Figure 2.4: ATLAS coordinate system.

2.2 The ATLAS Detector

To fully exploit the LHC capabilities the ATLAS detector [5] [6] has been designed as a general purpose detector with special attention to maximize the angular coverage. It has cylindrical symmetry around the beam axis and is composed of concentric shells of sub-detectors. The cylinder has a total length of 42 m, and a radius of 11 m and its overall weight is about 7000 tons. Figure 2.5 shows a three-dimensional view of the final design of the ATLAS apparatus which will be installed at the interaction point 1 of LHC.

The ATLAS coordinate system (fig.2.4) is right-handed with the z-axis along the beam line and the x-axis pointing toward the center of LHC ring. The y-axis points from the interaction point upward. Given the symmetry of the detector, a cylindrical coordinate system (z, φ, θ) is used. Instead of the polar angle θ, in hadron colliders, it preferable to use the pseudorapidity variable η, defined as :

$$\eta = -\ln(\tan(\theta/2))$$

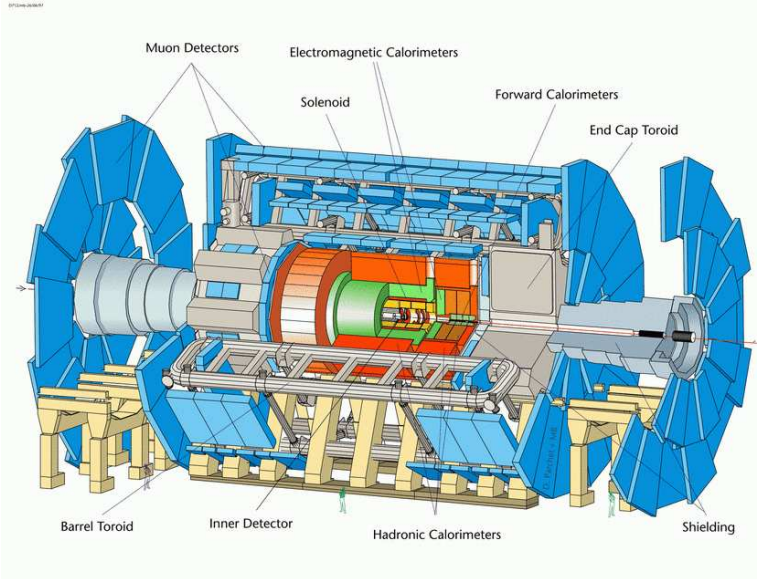

Figure 2.5: Overview of the Atlas detector layout.

The pseudorapidity distinguish four different regions in each half part of the cylinder : *Forward*($|\eta| \geq 2.7$), *Endcap* ($1.4 \leq |\eta| \leq 2.7$), *Transition* ($1 \leq |\eta| \leq 1.4$) and *Barrel* ($|\eta| < 1$).

From inner to outer radius, the ATLAS subdetectors are: an inner tracker, a calorimetric system (Electromagnetic and Hadronic) and a muon spectrometer. Moreover, the inner tracker and the muon spectrometer are in a magnetic field, in order to bend the charged particles trajectories. To exploit the full physics potential of LHC the ATLAS detector have to fulfill some basic design requirements:

- microvertex tracking for b-quark tagging as well as τ and heavy flavor vertexing and reconstruction capability;
- an excellent electromagnetic calorimetry for electron and photon identification and measurements, complemented by hermetic calorimetry;
- an accurate hadronic calorimeter for missing energy measurements;
- an efficient tracking for good momentum resolution and charge determination, provided by the inner tracker for low energetic tracks and by the large lever arm muon spectrometer for high energy muons;

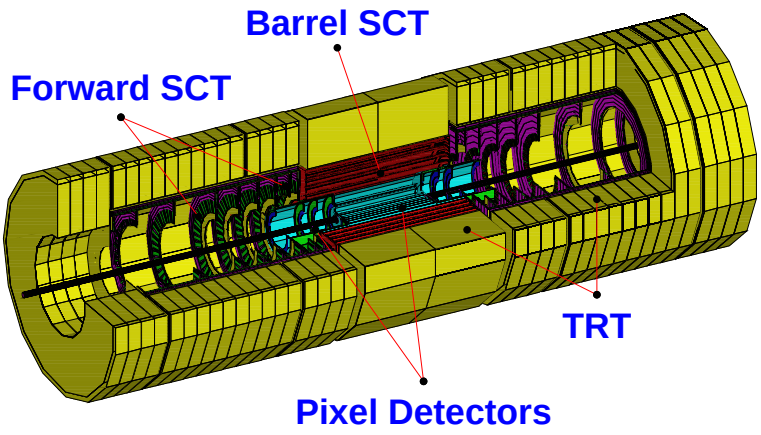

Figure 2.6: The layout of the Atlas inner tracker.

- stand-alone precision muon-momentum measurements up to highest luminosity, and low-p_T trigger capability at low luminosity;
- a large acceptance and maximum η coverage.

In the following all the sub-systems of the ATLAS detector are briefly described with a particular emphasis on the Muon Spectrometer.

2.2.1 Inner Detector

The ATLAS Inner Detector (ID) [15] [16] is shown in fig.2.6. It has a cylindrical geometry with a diameter of 2.3 m and a length of 6.8 m and is is in a magnetic field provided by a central solenoid. It combines two high-resolution semiconductor tracking detectors (pixel and SCT) at inner radii with a continuous straw tube tracker (TRT) at outer radii. The ID can be divided into three parts: a barrel region extending over $\pm$80 cm in z and two endcaps. The ID will reconstruct, with high resolution, the charged particles tracks and will provide the primary and secondary decays vertexes positions.

2.2.1.1 Pixel Detector

The innermost layers consist of silicon-pixel vertex-detectors [17]: there are three barrel layers of 140 million pixels, with dimensions of 50 μm in R-φ and 300 μm in z. On each side there are five disks, between radii of 11 cm and 20 cm; they have a dimension of 50 μm in R-φ and 350 μm in R. The design point resolution is of $\sigma_{R\varphi}$ = 12 μm and σ_z = 60 μm. The fine granularity ensures good performances in the expected high track densities and its high resolution allows to reconstruct the secondary decay vertices's of the particles.

2.2.1.2 Semiconductor Tracker

The silicon strip detectors - Semi Conductor Tracker (SCT) - are mounted in eight layers, arranged in pairs and rotated with respect each other of a stereo angle of 40 mrad. This design allows for a z measurements in the barrel and for radius measurement in the endcap regions. The strips in the barrel have a pitch of 80 μm and a length of 12.8 cm. In the endcap, in order to obtain an optimal η coverage, the lengths of the strips varies between 6 and 12 cm; the pitch in the endcaps varies too, the average size being about 85 μm. SCT provide precision measurements per track, contributing to the measurement of momentum, impact parameter and vertex position. The spatial resolution will be $\sigma_{R\varphi}$ = 18 μm and σ_z = 580 μm.

2.2.1.3 Transition Radiation Tracker

The Transition Radiation Tracker (TRT) is the outermost sub-system of the inner tracker and consists of 420,000 proportional drift tubes with a diameter of 4 mm. In the barrel the straw tubes are arranged in layers along z, while in the endcaps they are radially, mounted in wheels. The detector works with a $Xe/CF_4/CO_2$ gas mixture optimized for the detection of the X-rays created as transition radiation in stacks of thin radiators between the tubes. The single-wire resolution for the tracking hits is about 170 μm and the efficiency will be greater than 50% even for the highest rates. The TRT has two different discriminator thresholds in order to distinguish between tracking hits (only lower threshold) and transition-radiation hits (both thresholds).

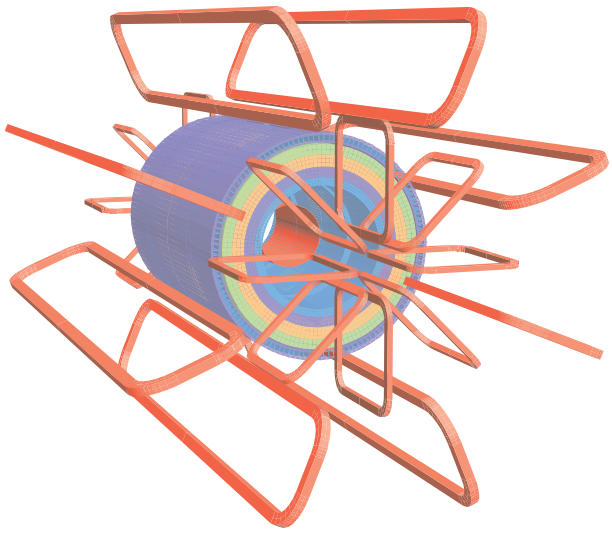

Figure 2.7: Geometry of the magnetic windings and masses; there are eight barrel toroid coils, with the endcap coils interleaved. The solenoid winding lies inside the calorimeter volume.

The overall vertex resolution is parameterized in $\mathrm{R}\varphi$ and z as:

$$\sigma(\mathrm{R}\varphi) = (11 + \frac{60}{\mathrm{p_T(GeV)}}\sin(\theta))(\mu\mathrm{m})$$

$$\sigma(\mathrm{z}) = (70 + \frac{100}{\mathrm{p_T(GeV)}}\sin^3(\theta))(\mu\mathrm{m})$$

2.2.2 The Magnet System

The Atlas Magnet System [18] consists of an hybrid configuration of solenoidal and toroidal coils with light and open structures (see figure 2.7).

Superconducting magnets produce the bending power for the momentum measurements of charged particles. The inner tracker is placed in a 2 T solenoidal magnetic field generated by a solenoid located within the electromagnetic calorimeter. The field is quite homogeneous in the barrel section and decreases rapidly with z in the end-cap region (Figure 2.8(a)). The toroidal design for the magnet is optimized for an high-resolution, a large acceptance and a robust stand-alone Muon Spectrometer. It consists of three air-core super-conducting toroids with an open structure to minimize the contribution of multiple scattering to the momentum resolution. Another important advantage of the toroidal magnetic field is the fact that the bending power increases with higher

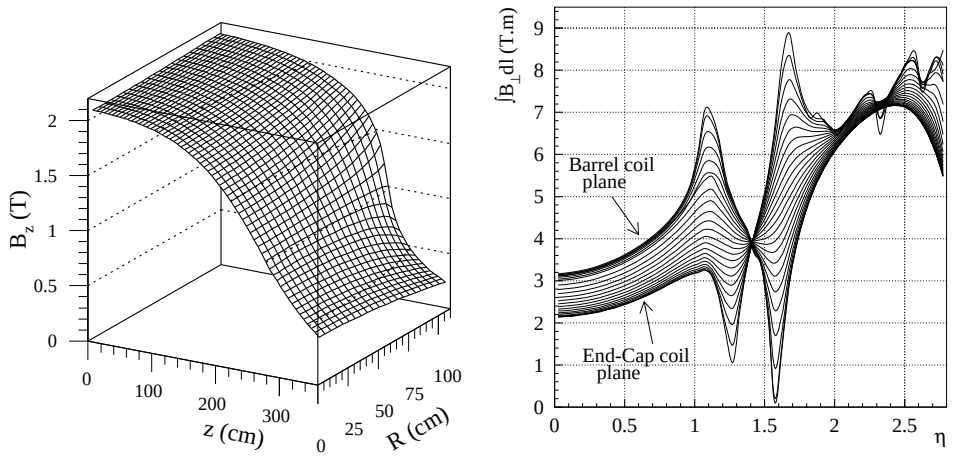

(a) (b)

Figure 2.8: The z component of the magnetic field in the inner tracker (a). The field integral versus pseudorapidity for infinite momentum muons, each curve corresponds to a fixed azimuthal range (b)

pseudo-rapidities, because the particles cross all the η range almost perpendicular to the field lines. The air-core toroid magnet configuration provides a peak field of 3.9 T in the barrel and of 4.1 T in the endcap.

The barrel toroid is composed of eight coils and extends over a length of 25 m, with an inner bore of 9.4 m and an outer diameter of 20.1 m.

The two end-cap toroids are inserted in the barrel at each end. Each endcap toroid consists of eight flat coils assembled radially and symmetrically around the beam axis. They are shifted by 22.5° in φ with respect to the barrel coils, and have a length of 5 m, an inner bore of 1.64 m and an outer diameter of 10.7 m. The disadvantage is the existence of regions with a highly non-uniform field, especially in the transition region as can be seen in Figure 2.8 (b).

2.2.3 The Calorimetric System

The ATLAS calorimeter system [19] [20] is shown in Figure 2.9. It is composed by an electromagnetic (ECAL) and an hadronic (HCAL) calorimeter. A barrel cryostat around the inner cavity contains the barrel electromagnetic Liquid Argon (LAr) calorimeter and the coil of the solenoid magnet. Two end-cap cryostats enclose the electromagnetic and hadronic end-cap calorimeters

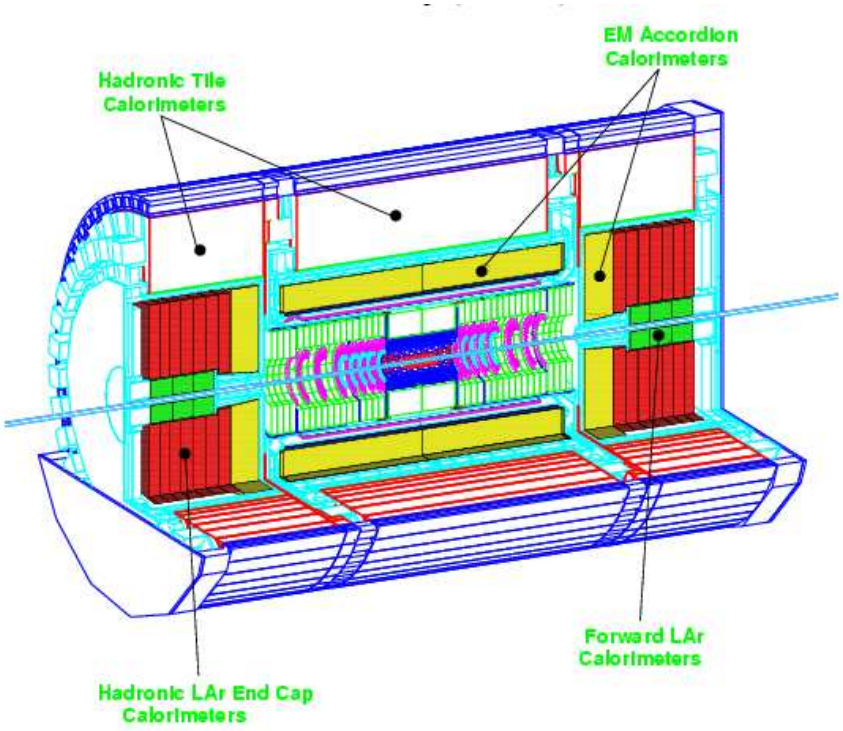

Figure 2.9: Layout of the Atlas calorimetric system.

as well as the integrated forward calorimeter (FCAL). The overall system encapsulates the inner tracker; it extends up to an outer radius of 4.25 m and has a length of 6.7 m in z. A presampler is placed in front of the calorimeter, which covers the region of $|\eta|$ <1.8; it allows for a correction of the energy lost in the material in front of the ECAL. In the 1.0< $|\eta|$ <1.6 region, there is, additionally, a scintillator slab which is used for the same purpose.

2.2.3.1 The Electromagnetic Calorimeter

The electromagnetic calorimeter is a lead-LAr detector with accordion shaped electrodes and lead absorber plates and covers the region up to η =3.2. The LAr sampling technique is radiation resistant and provides long-term stability of the detector response; it has excellent hermeticity, good energy resolutions, and the detector calibration is relatively easy. The total thickness of the electromagnetic calorimeter is greater than 24 X_0 in the barrel part and greater than 26 X_0 in the forward region. The segmentation of the calorimeter will be $\Delta\eta \times \Delta\varphi$ = 0.025×0.025, an energy

resolution of

$$\frac{\Delta E}{E} = \frac{10\%}{\sqrt{E}} + 1\% \text{ (E in GeV)} \tag{2.2}$$

will be achieved. The resolution in θ of the shower angular direction will be about 50 mrad/$\sqrt{E}$ (E in GeV).

2.2.3.2 The Hadronic Calorimeter

The hadronic calorimeter consists of different devices optimized for the different requirements and the radiation environment. The total thickness is 11 interaction lengths λ at η = 0, including 1.5 λ of the outer support. In the range of $|\eta| < 1.6$ a sampling calorimeter is used with iron as absorber material and scintillating tiles (3 mm thick) as active material (TILE Calorimeter). The signals produced on both sides of the scintillating tiles are read out by wavelength-shifting fibers into two separate photo-multipliers. The resulting segmentation of the hadronic calorimeter will be $\Delta\eta \times \Delta\varphi$ = 0.1×0.1.

In the range of $1.5 < |\eta| < 4.9$ an hadronic LAr calorimeter is used. The end-cap hadronic calorimeter extends up to $|\eta| < 3.2$, it is a copper-LAr detector with parallel plate geometry.

The high-density forward calorimeter covers the region of $3.2 < |\eta| < 4.9$ with the front face about 5 m from the interaction point and suffering of an high level of radiation. It is based on rods filled with LAr in a copper and tungsten matrix. The forward calorimeter is moved further out by 1.2 m with respect to the ECAL in order to reduce the number of backscattered neutrons into the inner tracker. The expected energy resolution for the hadronic calorimeter is

$$\frac{\Delta E}{E} = \frac{50\%}{\sqrt{E}} + 3\% \text{ (E in GeV)} \tag{2.3}$$

for $|\eta| < 3$, and

$$\frac{\Delta E}{E} = \frac{100\%}{\sqrt{E}} + 10\% \text{ (E in GeV)} \tag{2.4}$$

for $3 < |\eta| < 4.9$.

2.3 The Muon Spectrometer

The Muon Spectrometer [21] is in the outermost part of the ATLAS and have a double task: to trigger events, together with the electromagnetic calorimeter, giving momentum measurements and to provide the position measurements of the second coordinate (φ).

The conceptual design of the Muon Spectrometer is illustrated in fig.2.10 where it is possible to see the four different chamber types :

- Trigger Chambers
  Monitored Drift Tubes (MDT) and *Cathode Strip Chambers* (CSC)
- Tracking Chambers
  *Resistive Plate Chambe*rs (RPC) and *Thin Gap Chambers* (TGC)

The Muon Spectrometer is divided into three regions, as can be seen from fig. 2.11(top): a barrel extending in the pseudorapidity region $|\eta| < 1.2$ and two endcaps covering the regions $1 < |\eta| < 2.7$.

In the φ projection (fig.2.11,bottom), in both barrel and endcap region, the detector is divided into 16 towers with a sequence of large and small stations, defined as large and small sectors.
In the barrel region ($|\eta| < 1$), muon tracks are measured in chambers arranged in three cylindrical layers (*stations*) at radii of about 5 m, 7.5 m and 10 m defined as *Inner Medium and Outer* planes. The endcap chambers will cover the pseudo-rapidity range $1 < |\eta| < 2.7$, and are arranged in four disks at distances of 7 m, 10 m, 14 m and 21-23 m from the interaction point. Barrel chambers are rectangular while the endcap one have trapezoidal shapes. In the two lower barrel sectors, rails carrying the calorimeter and their supports require dedicated shaped chambers to maximize the detector acceptance. Moreover, there is a crack in the central R-φ plane, at η = 0, for the passage of the cables and services of the Inner Detector, the Central Solenoid and the calorimeters.

The design of the ATLAS Muon Spectrometer [21] was oriented to build an high-resolution muon spectrometer with stand-alone triggering and momentum measurement capability over a wide range of transverse momentum, pseudorapidity and azimuthal angle, fulfilling the following conditions:

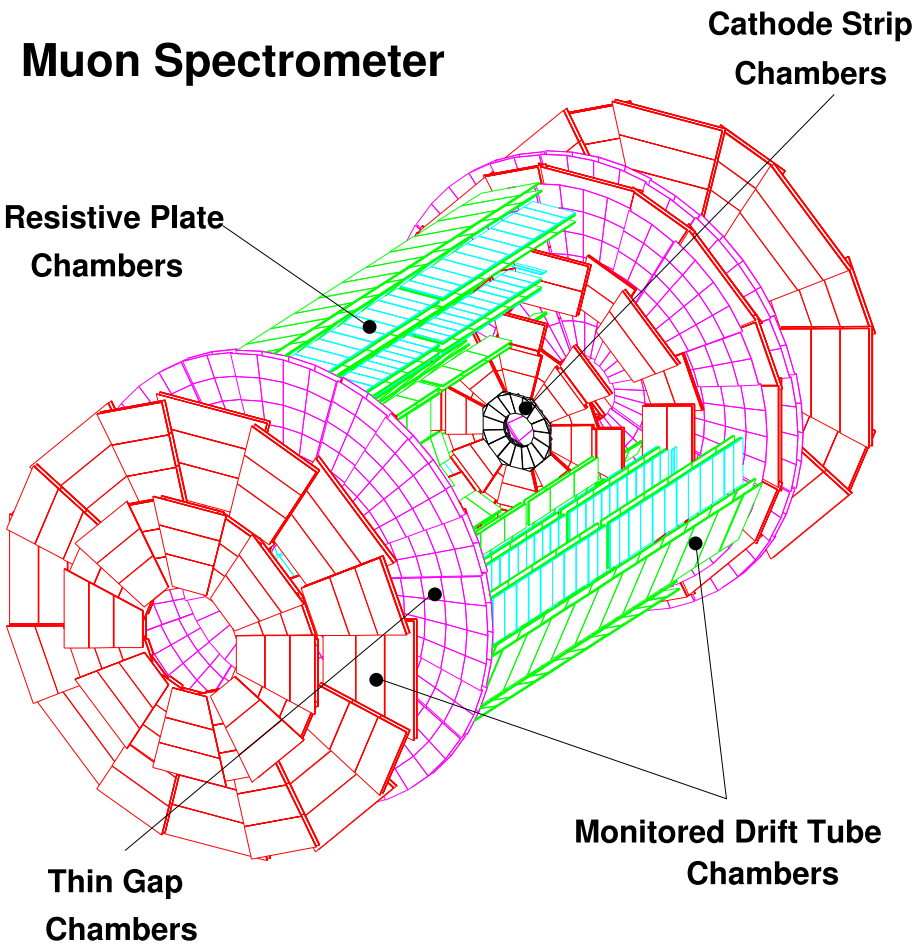

Figure 2.10: Muon spectrometer layout.

- A transverse-momentum resolution of 1% in the low $\mathrm{p_T}$ region ($\mathrm{p_T}$ <20 GeV/c^2). This limit is set by the requirement to detect the $\mathrm{H} \rightarrow \mathrm{ZZ}^*$ decay in the muon channel with a high suppression of the background.
- At the highest $\mathrm{p_T}$ the muon system should have sufficient momentum resolution to give good charge identification for $\mathrm{Z}' \rightarrow \mu^+\mu^-$ decay.
- A pseudorapidity coverage $|\eta| < 3$. This condition guarantees a good detection efficiency for high-mass particles decaying into muons within the acceptance region.
- An hermetic system to prevent particles escaping through holes.
- Measurement of both η and φ coordinates to provide good mass resolution.

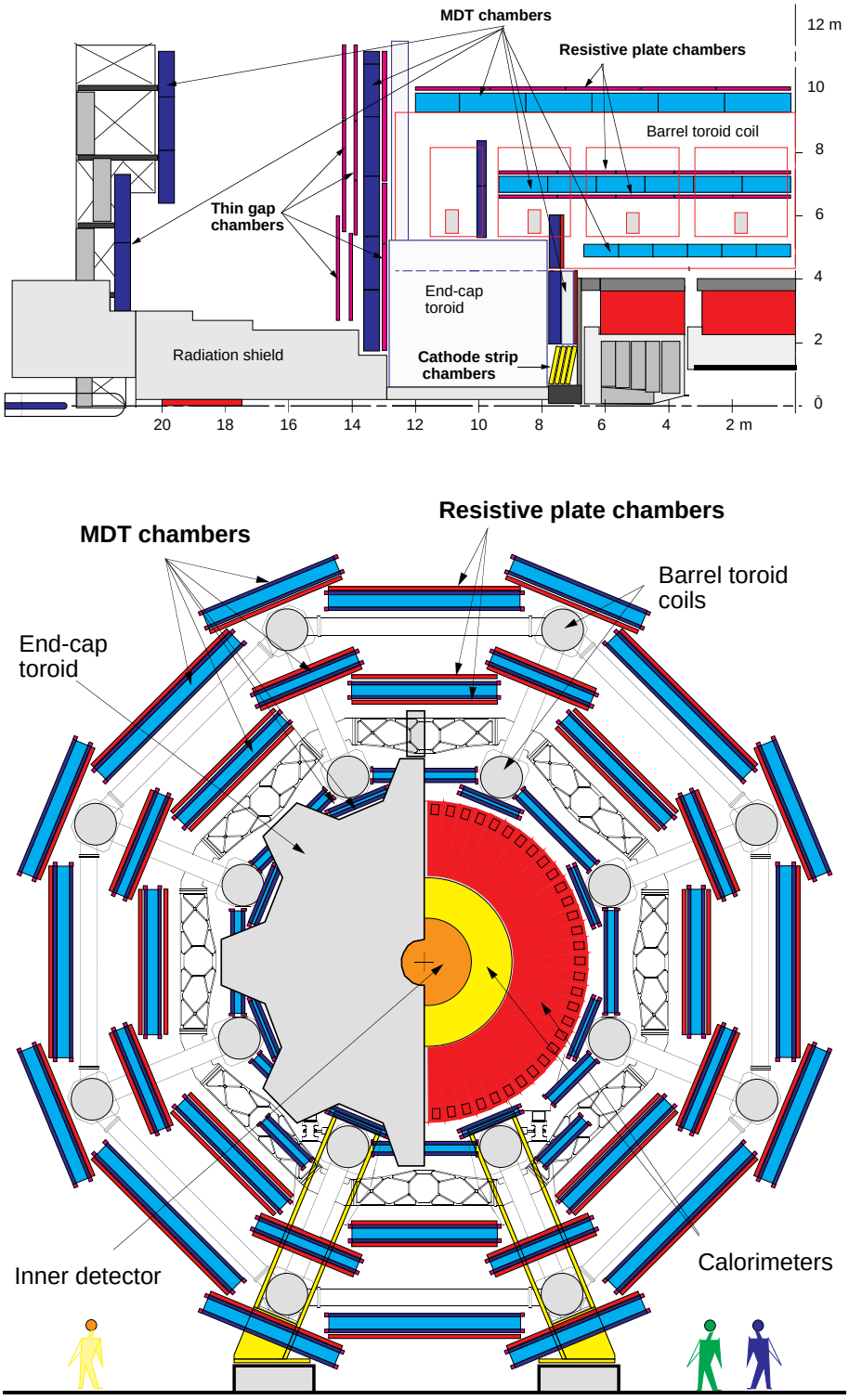

Figure 2.11: Side (top) and transverse (bottom) view of the Atlas Muon Spectrometer.

- A reduced rate of both punch-through hadrons and fake tracks.
- A trigger capability for almost all physics channels. For B physics a maximal coverage for muons with transverse momentum down to 5 GeV/c is required.

The stand-alone momentum resolution of the Muon Spectrometer is limited by different contributions depending on the momentum range. For momenta below 10 GeV/c, the fluctuation on the energy loss of muons in the calorimeters limits the resolution to about 6-8%. For momenta up to 250 GeV/c the resolution is affected mainly from the multiple scattering in the materials present in the spectrometer and is limited to about 2%, while for higher momenta the spatial accuracy of the chambers and the knowledge of their calibration and alignment give the largest contribution to the resolution.

As an example, a 1 TeV/c momentum muon is measured with a 10% resolution. To improve the muon measurement resolution at low momenta (below 100 GeV/c) it is possible to use a combined reconstruction of the muon trajectory using also the Inner Tracker. In this case the Muon Spectrometer is used mainly for the identification of the muon. Figure 2.12 shows the stand-alone resolution for the Inner Tracker and the Muon Spectrometer, together with the combined one obtained with the MOORE and MUID reconstruction packages [22].

In the Barrel, the muon momentum measurement is obtained measuring the sagitta of the muon trajectory produced by the magnetic field. The trajectory is sampled in three measuring stations equipped with MDT and arranged in three cylindrical layers around the beam axis. Each station measures the muon positions with a precision of about 50 μm. It also provides angular information on the measured track segments, which is then used to improve the pattern recognition for the reconstruction of the full muon track. In the two outer stations of the Barrel spectrometer, specialized trigger detectors RPC are present. In the middle station two layers, each comprising two RPC detectors, are used to form a low $\mathrm{p_T}$ trigger ($\mathrm{p_T} > 6$ GeV/c). In the outer station only one layer with two RPC detectors is used to form, together with the low $\mathrm{p_T}$ station, the high $\mathrm{p_T}$ trigger ($\mathrm{p_T} > 20$ GeV/c). The RPCs measure both the bending and the non-bending coordinate, and the trigger formation requires fast (< 25 ns) coincidences pointing to the interaction region.

In the endcap regions the measurement of the muon momentum is accomplished using three measuring stations of chambers mounted to form three big disks called wheels that are perpendicular to the beam direction, and measuring the angular displacement of the muon track when passing

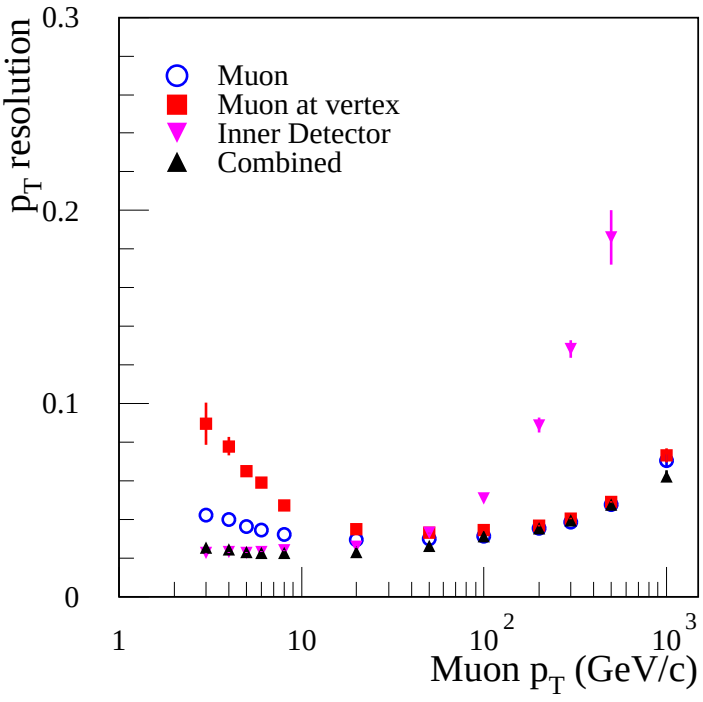

Figure 2.12: Resolution as a function of the transverse momentum for the stand-alone Muon Spectrometer reconstruction, the stand-alone Inner Detector and the combined one.

in the magnetic field (the toroids are placed between the first and the second tracking stations). In this case the volume of the toroids is not instrumented: a sagitta measurement is not possible hence a point-angle measurement is performed. MDT chambers are used for precise tracking in the full angular acceptance, with the exception of the inner station where the region $2 < |\eta| < 2.7$ is equipped with CSC which exhibit a smaller detector occupancy which is crucial in the high η zone. The CSCs have a spatial resolution in the range of 50μm.

The trigger acceptance in the End-Cap is limited to $|\eta| < 2.4$ where TGC are used to provide the trigger. The TGCs are arranged in two stations: one made of two doublets of two layers each, used for the low $\mathrm{p_T}$ trigger, and one made of three layers used for the high $\mathrm{p_T}$ trigger in conjunction with the low $\mathrm{p_T}$ stations. The high $\mathrm{p_T}$ station is placed in front of the middle precision tracking wheel and the low $\mathrm{p_T}$ station is behind it. The TGCs provide also the measurement of the second coordinate and for this reason there is a TGC layer also in the first tracking wheel.

A description of the different chambers used in the Muon Spectrometer is given in the following subsections.

2.3.1 The Tracking Chambers : MDT and CSC

Figure 2.10 shows the positioning of the MDT and CSC chambers used as tracking chambers in the Muon Spectrometer of ATLAS.

- **The Monitored Drift Tubes: MDT.**

  The precision tracking in ATLAS is performed in almost all the spectrometer by the Monitored Drift Tubes chambers [23]. The basic element for these chambers is a thin walled (400 μm) aluminum tube of a diameter of 3 cm with a length varying from 0.9 to 6.2 m, in which a 50μ W-Rn wire is strung with high mechanical precision. These tubes are assembled in two multilayers which are kept separated by three cross-plates, as shown in fig. 2.13

  The multilayers are formed by 3 or 4 layers of tubes, four-layer chambers being used in the inner stations. The mechanical accuracy in the construction of these chambers is extremely tight: the precision in wire positions inside a chamber should be better than 20 μm r.m.s. This has been checked on the first chambers produced measuring the wire position inside a chamber with an accuracy of less than 5 μm [24]. The resolution crucially depends also on the single tube resolution, defined by the operating point, the accurate knowledge of the calibration (r-t relation) and on the alignment of the chambers.

  The chambers are filled with a gas mixture of Ar 93% and CO_2 7%, at 3 bar absolute pressure, and are operated at a gas gain of 2×10^4 applying 3.1 kV on the wires. High pressure ensures high spatial resolution up to large drift radii, an average resolution of about 80 μm per wire is obtained.

  The r-t relation of the tubes in ATLAS should be measured using only information coming from the MDTs. An autocalibration procedure [25] has been developed to obtain the required spatial resolution.

  Moreover for achieving the desired resolution at high transverse momentum an excellent alignment system is needed enabling the monitoring of the position of the different chambers in the spectrometer with a precision better than 30 μm. The basic elements of this system are

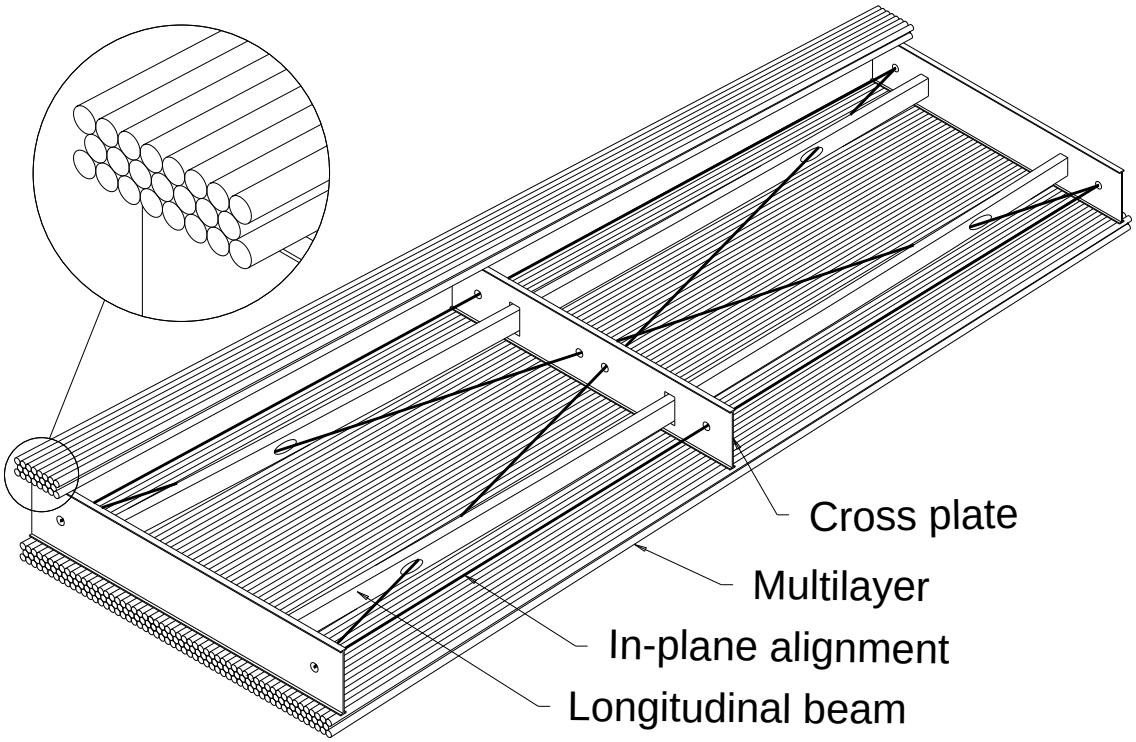

Figure 2.13: Schematic view of an MDT chamber.

RASNIK [26] optical straightness monitors, formed by three elements along a view line: a laser which illuminates a coded target mask at one end, a lens in the middle and a CCD sensor at the other end. This system provides a very accurate measurement of the relative alignment of three objects (1 μm r.m.s.) and is used both for checking the in-chamber deformations (in-plane alignment), and the relative displacement of different chambers (axial-praxial and projective alignment). Figure 2.14 shows the conceptual design of the alignment system in the barrel region.

The accuracy of the barrel and endcap alignment system has been tested during the 2002 ATLAS Muon System Test at the H8 beam line at CERN, using muons of 20 GeV/c demonstrating the correctness of the alignment concept in ATLAS.

- **The Chatode Strip Chambers: CSC**

  The Cathode Strip Chambers [27] are multiwire proportional chambers with cathode strip read-out. A schematic cutout view of the Cathode Strip Chamber is shown in figure 2.15.

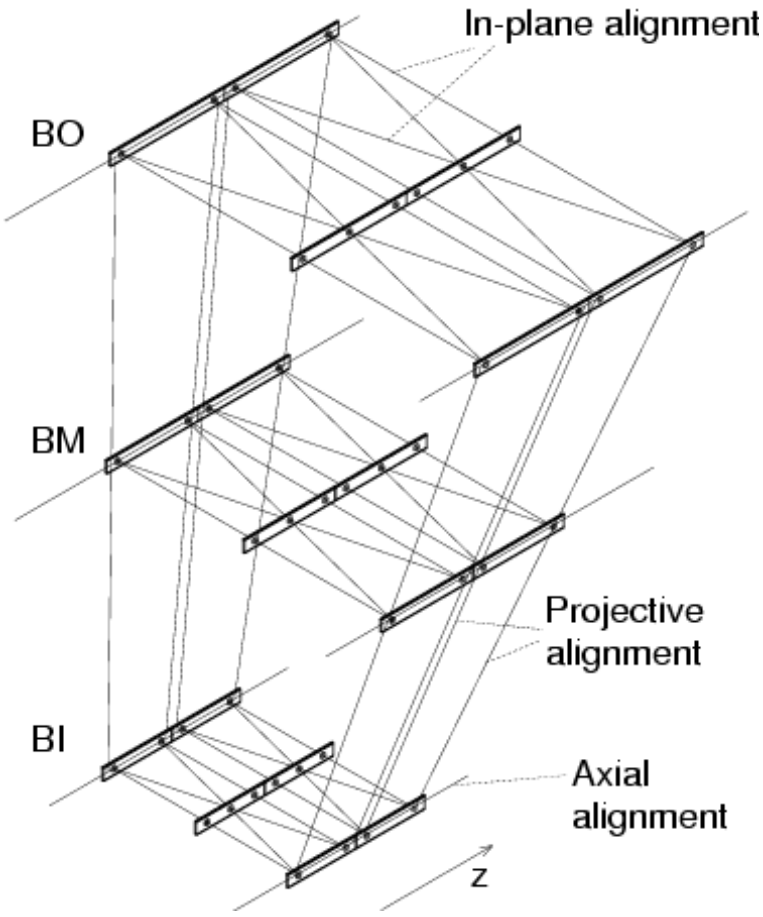

Figure 2.14: The projective alignment system in the barrel region.

The pitch of the anode wires is 2.54 mm and the cathode readout pitch is 5.08 mm. The cathode planes are equipped with orthogonal strips and the precision coordinate is measured determining the charge interpolation between neighboring strips. The typical resolution obtained with this read-out scheme is about 50μm. The reduced size of the basic cell implies also small maximum drift time (about 30 ns) which is beneficial to sufficiently reduce the chamber occupancy. The gas mixture used is based on Ar (30%), CO_2 (50%) and CF_4 (20%), the wires are supplied by 2.6 kV, resulting in a gas gain of 10^4. In ATLAS the CSCs will be arranged in two layers, each containing 4 layers of cells, enabling 8 high precision measured points on a single track. The shape of the chambers is trapezoidal and they will be mounted on the inner tracking wheel for $2 < |\eta| < 2.7$. In this region the counting rate due to photons and neutrons is of the order of 1 $\mathrm{kHz/cm^2}$, and this could cause a degradation of

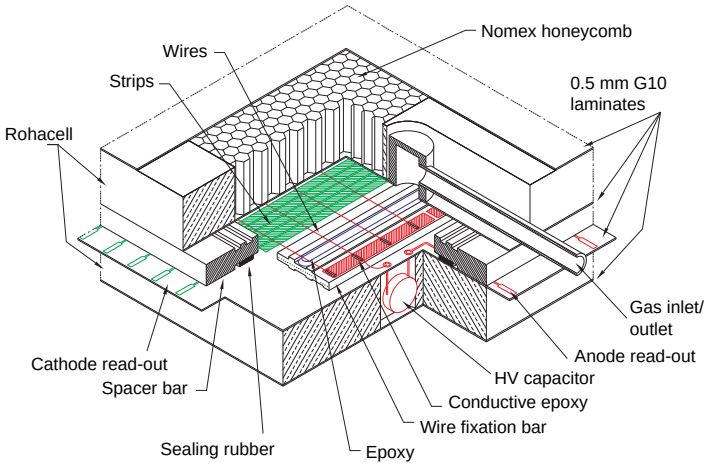

Figure 2.15: Cutout view of the CSC layer.

efficiency and resolution measurements. Tests have been carried out at CERN to study the dependence of efficiency and resolution on the counting rate [28] showing a degradation of the single plane resolution with the rate down to 70μm fora rate of about 2 $\mathrm{kHz/cm^2}$.

2.3.2 The Trigger Chambers : RPC and TGC

The RPCs and TGCs trigger chambers are positioned in the Muon Spectrometer following the schematic layout of fig. 2.16.

- **The Resistive Plate Chambers: RPC.**

  The RPCs (see fig. 2.17) are gaseous detectors made of two parallel resistive bakelite plates (of bulk resistivity $\sim 10^{11\pm1}\ \Omega cm$) separated by insulating spacers which form a 2 mm gas gap. High voltage is applied on these plates through graphite electrodes, and electrons produced by an ionizing particle in the gas gap are multiplied into avalanches. The electrical signals produced in the gas gap are induced on two read out copper strip planes placed on both sides of the gap, and then amplified and discriminated by fast electronics. The gas composition used is: $\mathrm{C_2H_2F_4}$ 94.7%, $\mathrm{C_4H_10}$ 5% and $\mathrm{SF_6}$ 0.3%, resulting in a non-flammable and environmentally safe one. $\mathrm{SF_6}$ is used to limit the charge produced in each pulse and

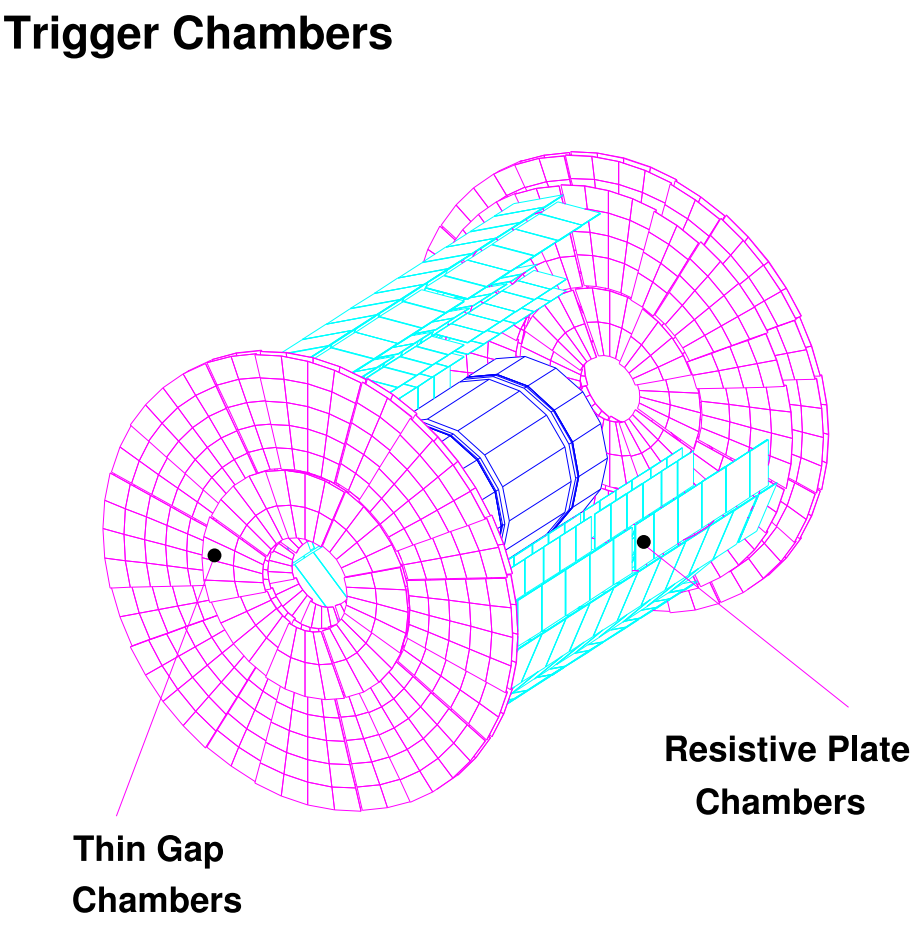

Figure 2.16: Trigger detectors of muon spectrometer.

to reduce the streamer probability. A typical value for the electric field is 5.0 kV/mm and typical space-time resolutions of 1 cm $\times$ 1 ns are achieved.

- **The Thin Gap Chambers: TGC.**

  The Thin Gap Chambers [29] have been chosen as trigger chamber in the endcap sectors of the ATLAS Muon Spectrometer because of their very good rate capability and ageing characteristics. They are multiwire proportional chambers with a smaller distance between the cathode and the wire plane compared with the distance between wires (fig. 2.18).

  The main dimensional characteristics of the chambers are a cathode distance of 2.8 mm, a wire pitch of 1.8 mm and a wire diameter of 50μ. The gas composition is 55% CO_2 and 45% n-pentane, which results in a highly quenching gas mixture that permits the operation in

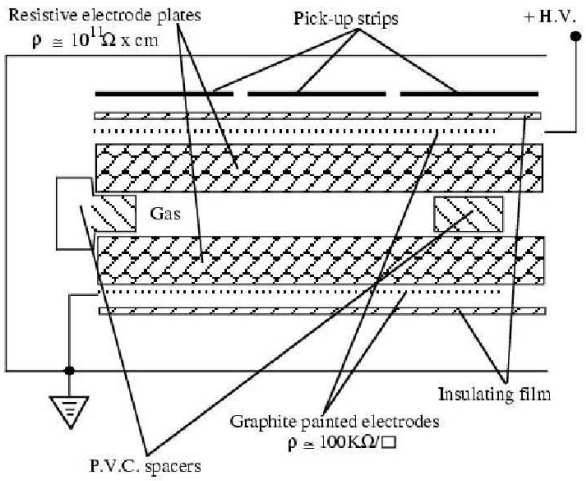

Figure 2.17: Basic schema of a Resistive Plate Chamber

saturated avalanche mode. This mode of operation enables a small sensitivity to mechanical deformations, a small dependence of the pulse height on the crossing angle and a very small streamer formation probability. The chambers are operated at an high voltage of about 3 kV. The operating condition and the electric field configuration provide for a short drift time, enabling a good time resolution of about 4 ns. The read-out of the signals is done both from the wires (which are grouped together in variable numbers between 4 and 40, according to the desired trigger granularity as a function of the pseudorapidity) and from a pick-up strip plane placed on the cathode. The wire planes and the strips are perpendicular to each other enabling the measurement of two orthogonal coordinates, only the wire signals are used in the trigger logic.

2.4 Trigger System

The role of the trigger system is to select bunch crossings containing interesting interactions. The data acquisition will be able to record events with a rate of 200 Hz (10-100 MB/s). Hence the task of the trigger is to reduce the huge interaction rate of 40 MHz to 100 Hz of interesting events. The ATLAS trigger scheme is based on three levels: LVL1 [30], LVL2 and EF (Event Filter), figure 2.19 shows the architecture.

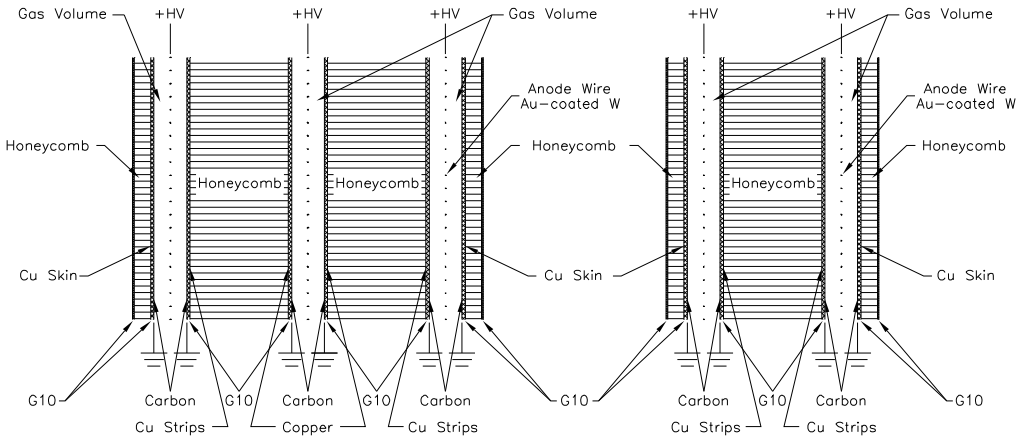

Figure 2.18: Cross section of a triplet (left) and a doublet (right) of TGCs. The gas gap is not drawn on the same scale as the other elements.

Each successive step takes into account more and more refined information and can work at a lower rate. The LVL2 and the EF are commonly referred as the High Level Trigger (HLT) system [31]; they share the overall trigger selection framework and differ mostly in the amount of the data they can access.

The LVL1 [30] trigger is hardware based and accepts data at the full LHC bunch-crossing rate of 40 MHz (every 25 ns). The latency, which is the time to form and distribute the LVL1 trigger decision, is 2 μs and the maximum output rate is limited to 100 kHz by the capabilities of the subdetector readout systems and the LVL2 trigger. During the LVL1 processing, data from the Calorimeters and the Muon Spectrometer are quickly analyzed to obtain an accept or reject decision.

The calorimeter selections are based on reduced-granularity informations from all the calorimeters. The algorithm searches for isolated electromagnetic clusters with transverse energy above 30 GeV, or high energy hadronic jets and large missing transverse energy. The muon trigger system (see fig.2.20) has been designed in order to supply both low (6 GeV) and high (20 GeV) transverse momentum trigger signal. The lower trigger threshold in the barrel uses the two innermost RPC layers, in the $medium$ plane. Here there is an MDT station between two RPC stations. The closer RPC station to the interaction point is called the *Low p_T confirmation plane* while the second RPC station is called the *Pivot plane*. In both the η and φ projections, a coincidence in three out of four strip planes is required. In the endcaps, the low $\mathrm{p_T}$ trigger is realized by a three out of four

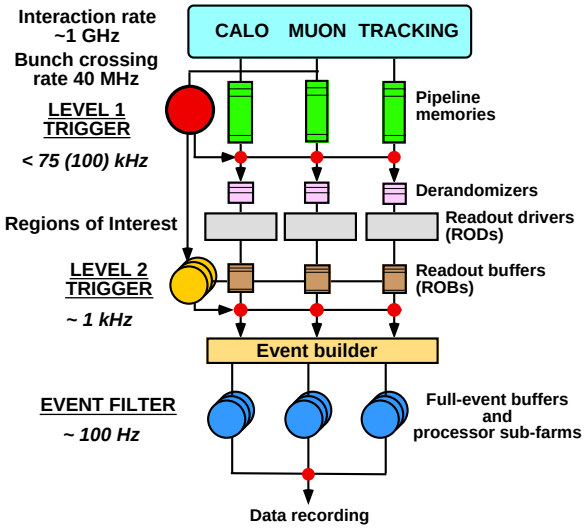

Figure 2.19: Trigger architecture of the ATLAS experiment.

coincidence in the two outermost layers. The high $\mathrm{p_T}$ trigger is obtained by requiring an additional hit in each projection of the $Outer$ RPC layer (called *High p_T confirmation plane*) or a two out of three coincidence in the bending plane of the triplet of the innermost TGC chambers plus one out of two coincidence in the azimuthal strip planes. A low-$\mathrm{p_T}$ trigger is generated analyzing data coming only from the RPCs located in the Middle Station of the Spectrometer: if an hit is generated in the second plane (*Pivot*), hits are searched in the first plane (*Low p_T confirmation plane*) within a road (*Coincidence Window*) whose center is defined by the line of conjunction of the hits in the two RPC planes and the interaction point, corresponding to an infinite momentum track, and whose widths depend on the cut on $\mathrm{p_T}$. The high-$\mathrm{p_T}$ trigger algorithm operate in a very similar way involving also the outer stations (*High p_T confirmation plane*) and requiring in addition also the low-$\mathrm{p_T}$ coincidence.

The LVL1 system identifies the interesting bunch crossing and provides the so called *Region of Interest* (RoI) to the next trigger level. The RoIs contain information about the position, the threshold and the deposited energy of a small fraction of the detector.

Accepted events are passed to the software based LVL2 trigger at a rate of 75 kHz which must take a decision within an average latency of 10 ms, reducing the rate from about 100 kHz after LVL1 to 1 kHz; in this step data from different RoIs are processed in parallel. It performs a more detailed reconstruction to be able to validate and further refine the physics objects. The Inner Detector is

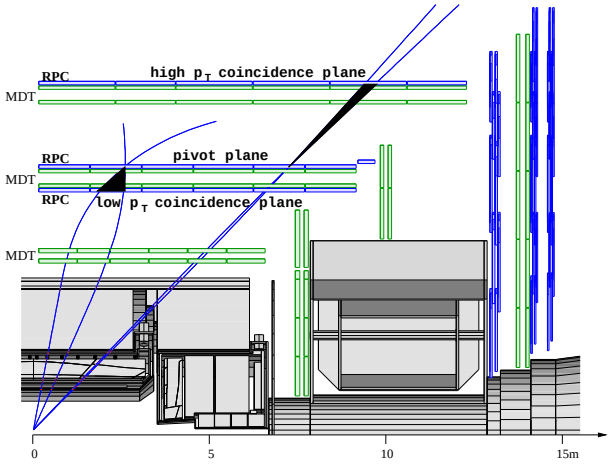

Figure 2.20: Level-1 muon trigger scheme.

also involved in the LVL2 trigger.

After an event is accepted, the full data are sent to the EF processors, via the event builder, which provide the final selection of physics events that will be written to mass storage for the full offline analysis. At the EF stage, a complete event reconstruction is possible with decision times up to about 1 s, it will employ the offline algorithms and methods, adapted to the online environment, and will use the calibration and alignment information. The EF system must achieve a data storage of 10-100 MB/s by reducing the event rate and the event size.

For some triggers, such as Higgs boson candidates, the full event size of about 1 MB will be recorded. Table 2.2 summarizes the input rate, the output rate and the latency for the three levels.

Trigger Level	**Input Rate**	**Outpour Rate**	**Latency**
LVL1	40 MHz	100 kHz	2 μs
LVL2	100 kHz	1 kHz	10 ms
EF	1 kHz	200 Hz	1 s

Table 2.2: Input/output data rates and latency of the three Atlas trigger levels

Chapter 3

Experimental search for Supersymmetry

In this chapter I will present the current status on experimental search for Supersymmetry at LEP and Tevatron colliders, the constraints set by WMAP experiment on the study of Dark Matter, strictly connected to the search for Supersymmetry, and the results from indirect measurements such as $b \rightarrow s\gamma$ decay and the anomalous magnetic moment of the muon. It will be sketched, furthermore, the strategy of the search for Supersymmetry at LHC, in particular with the ATLAS detector.

3.1 Constraints on Supersymmetry

As already said, Supersymmetry is one of the best motivated models for physics beyond the Standard Model because it does not contradict the precise measurements of electroweak parameters, it predict a light Higgs boson, it gives rise to a better unification of the gauge couplings at the Grand Unification Scale, it includes, in a natural way, the gravity, it solves the naturalness problem and it could represent a very good candidate for the cold dark matter. All of that explains why Supersymmetry is one of the main subjects of High Energy Physics experiments: no direct experimental evidence for supersymmetric particles is there so far, in fact, experiments at colliders like LEP (e^+e^-) and TEVATRON ($p\bar{p}$), have only set numerous constraints on Supersymmetry. It will be the new collider LHC (pp) which can explore directly, for the first time, all physics, particularly the Supersymmetry, at an energy scale up to ~ 1 TeV so that it will be able to discover low-energy

(TeV scale) SUSY or, eventually, to reject it definitively.
In the following I will describe some of the constraints on SUSY provided by LEP and TEVATRON.

3.1.1 LEP and Tevatron SUSY constraints

Using a hadron collider allows to reach a greater center of mass energy in comparison with a lepton collider but, at the same time, the former has the disadvantage of operating in an environment dominated by a huge QCD background making harder the measurement of experimental observables. In this sense the LEP and TEVATRON searches have been complementary [36] as it is possible to see in figure 3.1

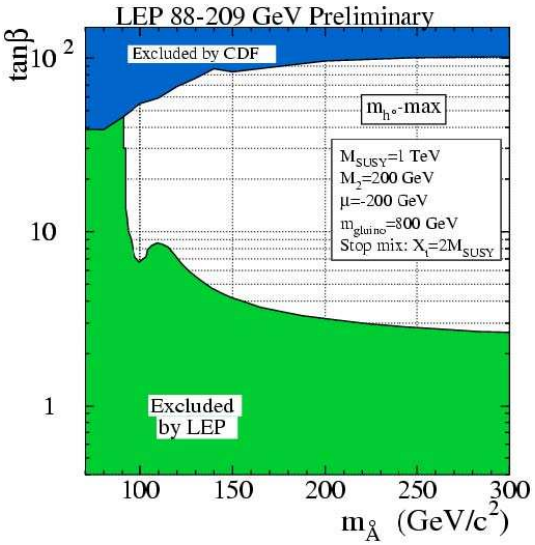

Figure 3.1: The regions of the CMSSM plane m_A-tanβ excluded (at the 95% CL) by the Higgs searches: at LEP in green (light shaded); at Tevatron (CDF experiment) in blue (dark shaded)

At LEP only the search for hZ and hA channels is possible (the other Higgs bosons are predicted to be too heavy), particularly for $m_A < 100$ GeV the relevant process is hA while for $m_A > 100$ GeV it is the hZ process which gives rise to similar final states as the HZ Standard Model processes. So LEP has excluded the low-tanβ region (m_h increases with tanβ so the lower limit on the former at ~ 114 GeV corresponds to a lower limit on tanβ). TEVATRON, has a center-of-mass energy such

as to produce any neutral Higgs boson in association with a $b\bar{b}$ pair up to masses of ~ 300 GeV. Furthermore the rates of these processes are greater for large values of tanβ so that the absence of any signal has allowed to exclude the large tanβ region as showed in fig. 3.1.
In general at lepton e^+e^- collider like LEP can be produced, more or less with similar cross sections, all kinematically accessible supersymmetric particles, except gluinos, by means of tree level processes $e^+e^- \to \tilde{\chi}_i^+\tilde{\chi}_j^-, \tilde{\chi}_i^0\tilde{\chi}_j^0, \tilde{l}\tilde{l}, \tilde{q}\tilde{q}, \tilde{\nu}\tilde{\nu}$

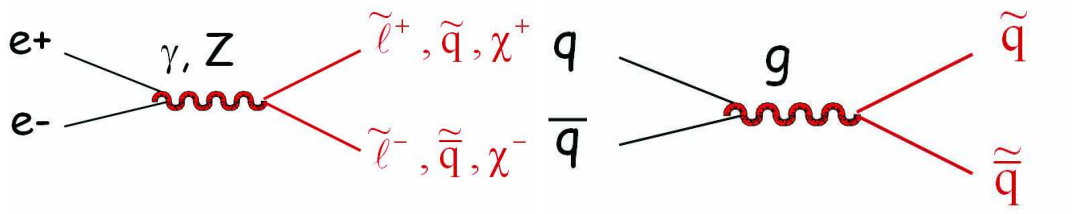

Figure 3.2: Main production diagrams: on the left at LEP; on the right at Tevatron.

with diagrams showed in fig. 3.2 (on the left) which take place with γ/Z bosons exchange (s-channel diagram). Once sparticles have been produced, they decay with the LSP in the final state (for instance $\tilde{l} \to l\tilde{\chi}_1^0$, $\tilde{q} \to q\tilde{\chi}_1^0$), giving rise to a big amount of missing energy in the detector (often, as in this case, the LSP (if R-parity is conserved) is identified with $\tilde{\chi}_1^0$ which is an electrically neutral and a weakly interacting particle). The resulting signature is therefore quite simple: two leptons or acoplanar jets plus missing energy due to the two escaping neutralinos. The SM background (e.g. WW, ZZ production) is not a big problem so that the experiments are sensitive to all sparticles and almost all decay modes even when the energy deposition in the detector is modest, thing which happens when the mass difference between the produced sparticle and the LSP, Δm, is small: in this way at LEP the mass search is limited by the available center-of-mass energy rather than by the physics conditions.
For what concerns hadron colliders (like Tevatron) $\tilde{q}\tilde{q}$, $\tilde{g}\tilde{g}$, $\tilde{q}\tilde{g}$ are mainly produced with diagrams in figure 3.2 (on the right).

Squarks and gluinos, which are expected to be very heavy according to the present experimental limits, decay through long decay chains terminating with a LSP in the final state. An example of such a decay chain is showed in figure 3.3.

The experimental signature of each SUSY event is therefore represented by many jets with high

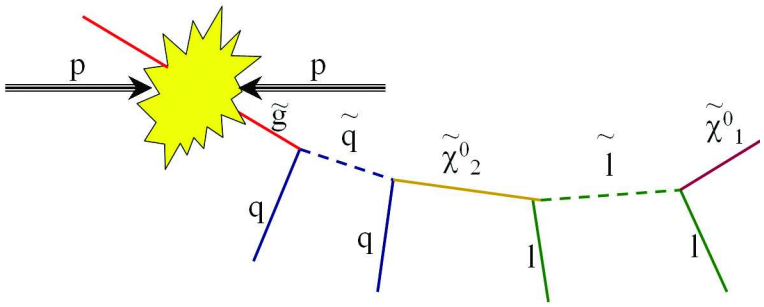

Figure 3.3: An example of possible decay chain at hadron colliders.

transverse momentum p_T plus leptons plus large missing transverse energy E_T^{miss} due again to the two escaping neutralinos. In this case the SM background is very huge but it is possible to reject it by means of strong requirements on number and p_T of jets and on E_T^{miss}: this latter requirements makes the low Δm region not accessible so that it is not possible to obtain mass limits valid for any choice of the parameters (as it happens for LEP) but, unlike lepton colliders, the mass reach for squarks and gluinos is very huge.

Both for lepton collider and for hadron collider the most important experimental observable for studying supersymmetry is the missing energy, sometimes associated with leptons and/or jets from the decay chains: this is true not only for models conserving R-parity but even for those not conserving it since a big missing energy is anyway expected due to energetic neutrinos in the final states.

Charginos

The best results for this search come from LEP, in particular from LEP2 with center-of-mass energy over the W pair production threshold, where take place processes $e^+e^- \rightarrow \chi^+\chi^-$ followed by $\chi^\pm \rightarrow W^*\chi_1^0$ for large values of m_0 or $\chi^\pm \rightarrow l\tilde{\nu} \rightarrow l\nu\chi_1^0$ if m_0 is small. So the final state presents missing energy from neutralinos associated with jets or with jets plus one lepton or two acoplanar leptons. Once the SM background is removed, one can obtain the lower limit on charginos mass of 103.6 GeV as showed in figure 3.4.

Neutralinos

The main process for $\tilde{\chi}_1^0$ production is $e^+e^- \rightarrow \chi_i^0\chi_j^0$ where $i,j = 1,2,3,4$ which proceeds via s channel Z exchange and via t channel selectron exchange. The process with the lowest threshold which gives rise to visible final states is $e^+e^- \rightarrow \chi_1^0\chi_2^0$ and leads to two relevant topologies:

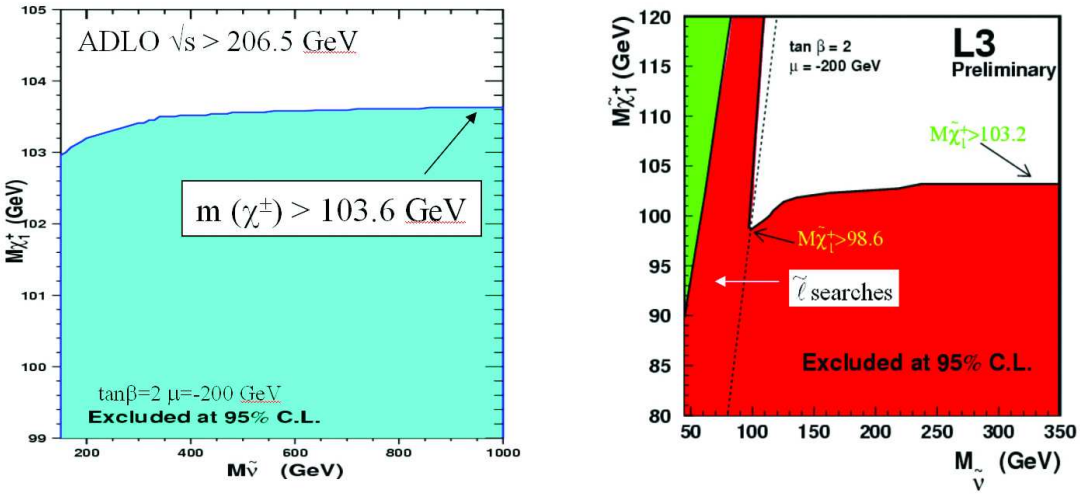

Figure 3.4: Mass limits for charginos searches at LEP in $m_{\tilde{\nu}} - m_{\tilde{\chi}_1^+}$. The left figures refers to the region in which it is kinematically not allowed the charginos decay into sleptons. The right figures refers to the case in which such a decay is possible.

acoplanar lepton pairs and acoplanar jets plus a large amount of missing energy. No events with those signatures have been observed beyond the expected Standard Model background. Combining this measurement with the results of other channels (this is possible because masses of the various sparticles are related) one obtains the lower limit on the neutralino mass as a function of the parameter tanβ, as showed in figure 3.5.

In this way it is found the absolute limit $m(\chi_1^0) > 45.6$ GeV at 95% CL asymptotically for tan$\beta \geq 20$ and small values of m_0.

Sleptons

Present experimental limits on search for sleptons come from LEP where slepton pair production has a much better signal-to-background ratio in comparison with the one at Tevatron, particularly best results were obtained at LEP2 with energy range between 184 GeV e 208 GeV. The experimental topology for these events is very simple: two acoplanar same flavour leptons plus a large amount of missing energy. The main source of SM background arises from processes such as $e^+e^- \rightarrow W^+W^-$ with missing energy originated by leptonic decays $W \rightarrow l\nu$. This background is almost irreducible even if the kinematics is sufficiently different from those expected from slep-

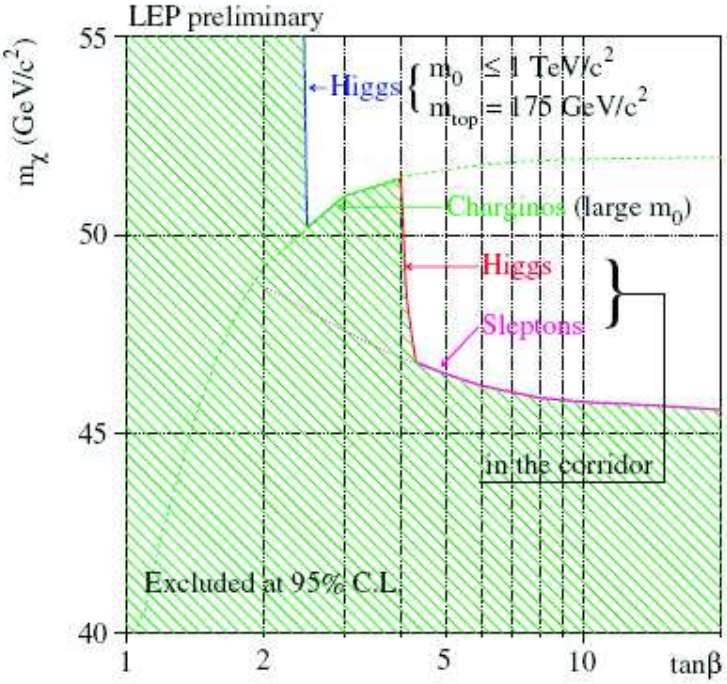

Figure 3.5: The 95% CL lower limit on the mass of the lighest neutralino, as a function of tanβ, as obtained in the constrained MSSM by combining the four LEP experiments. The searches used to set the limit in the various tanβ regions are indicated.

ton pair production: for instance, the typical momentum of muons from smuons decay is smaller than the one of muons from W decay and this feature becomes more and more enhanced as the neutralino mass increases.

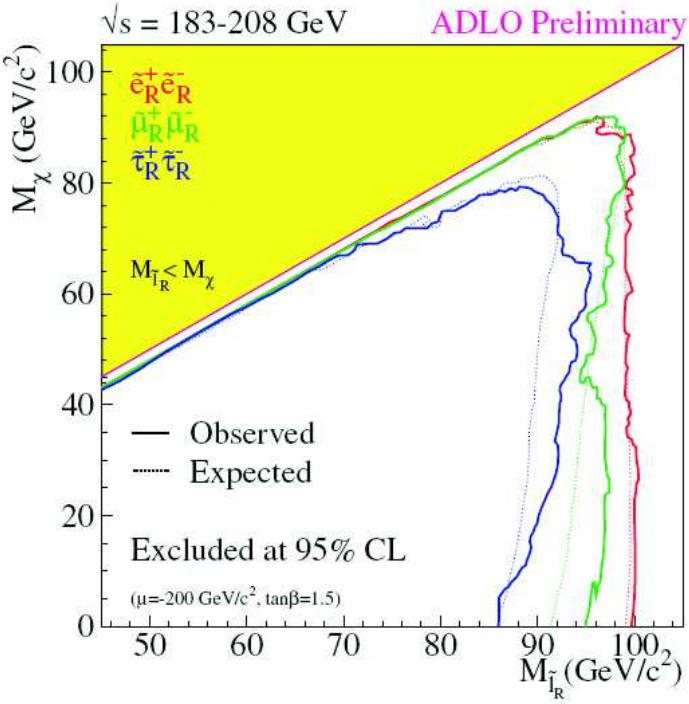

Figure 3.6: Experimental limits on slepton mass as obtained at LEP in the (slepton mass - LSP mass) plane at 95% CL: in blu, green and red are represented the limits for staus, smuons and selectrons respectively (full lines). The dashed lines indicate the corrisponding expected limits. The shaded region is theoretically forbidden.

These searches have found no deviations from the SM expectations and in figure 3.6 the derived mass limits are shown in the $m_{\chi^0_1} - m_{\tilde{l}}$ plane.
Finally, taking into account the lower limit on Higgs mass, $m_H > 114.1$ GeV, corresponding to the lightest MSSM Higgs boson, it is possible to combine slepton, chargino, Higgs boson and the Z width searches to derive some exclusion domains on mSUGRA parameters: figure 3.7 shows the SUSY constraints obtained by ALEPH [37] in the $(m_0, m_{1/2})$ plane for tan$\beta = 5, 10$, for $\mu > 0$ and $\mu < 0$, for $A_0 = 0$ assuming the top mass to be 175 GeV.

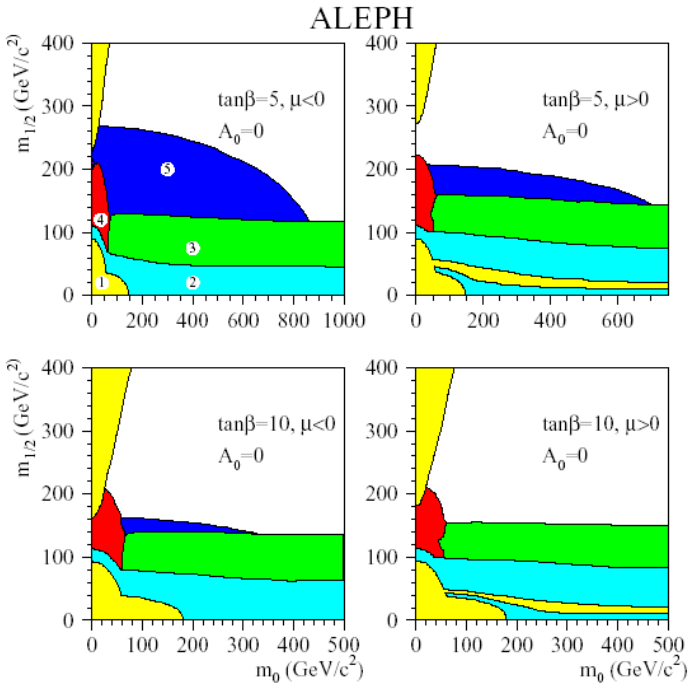

Figure 3.7: Excluded regions in the $(m_0, m_{1/2})$ plane given tan$\beta = 5$, 10 and $A_0 = 0$. Region (1) is theoretically forbidden; other regions are excluded by the study of width of Z at LEP1 (2), by measurements on chargino mass (3), by those on slepton mass (4) and by Higgs boson searches (5) at an center of mass energy of $\sqrt{(}s) = 201.6GeV$

Squarks and gluinos

Differently from LEP, Tevatron has the largest discovery potential for squarks and gluinos. In particular, the main signature for the pair production of these sparticles at Tevatron (at hadron colliders in general) is represented by a large amount of missing transverse energy E_T^{miss} from escaping neutralinos plus jets and/or leptons from decay chains. The main difficulties in this search is due to fake E_T^{miss} measurement because of resolution effects and cracks of the detector or from mismeasured QCD multijet events . In figure 3.8 is there an example of the experimental E_T^{miss} distribution at Tevatron which does not show any excess with respect to Standard Model distributions.

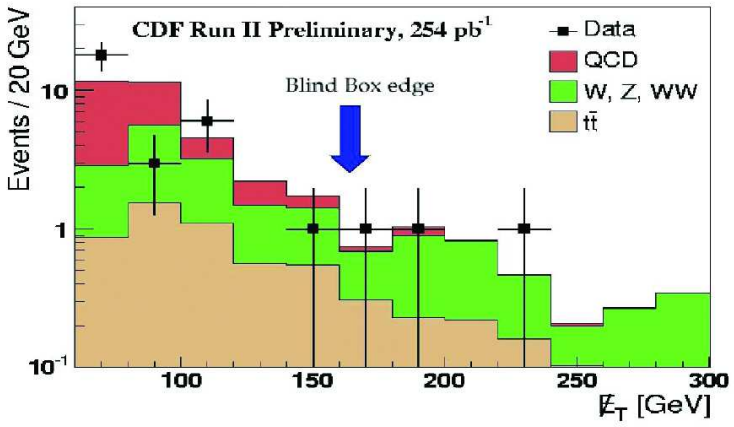

Figure 3.8: Missing energy distributions obtained at TEVATRON; points represent data while colored distributions indicate the Standard Model previsions (from Montecarlo).

From search for missing transverse energy plus jets signatures one obtains the most stringent limits on squarks and gluinos masses: $m_{\tilde{q}} \simeq m_{\tilde{g}} > 300$ GeV (namely $m_{\tilde{g}} > 300$ GeV for any value of the squark mass) as shown in figure 3.9.

Other processes can take place at Tevatron: namely $p\bar{p} \rightarrow \tilde{\chi}_2^0 \tilde{\chi}_1^{\pm}$ with further $\tilde{\chi}_2^0 \rightarrow l^+ l^- \tilde{\chi}_1^0$ and $\tilde{\chi}_1^{\pm} \rightarrow l\nu\tilde{\chi}_1^0$ decays. In this case the signature consists of three isolated leptons plus missing transverse energy and, in spite of the low cross section, with a very low component of Standard Model background; being these processes very model dependent one can only place limits on SUSY cross section as a function of chargino masses by making standard assumptions on model (cfr. fig. 3.10).

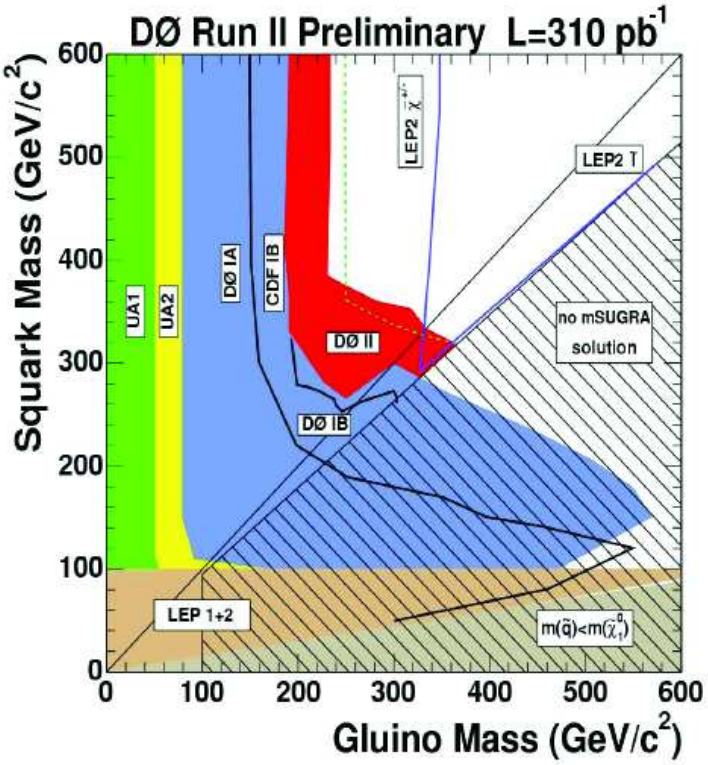

Figure 3.9: Regions of the plane squark mass versus gluino mass excluded at the 95% CL by CDF, D0, and LEP. The hatched region at the bottom right corner is theoretically forbidden.

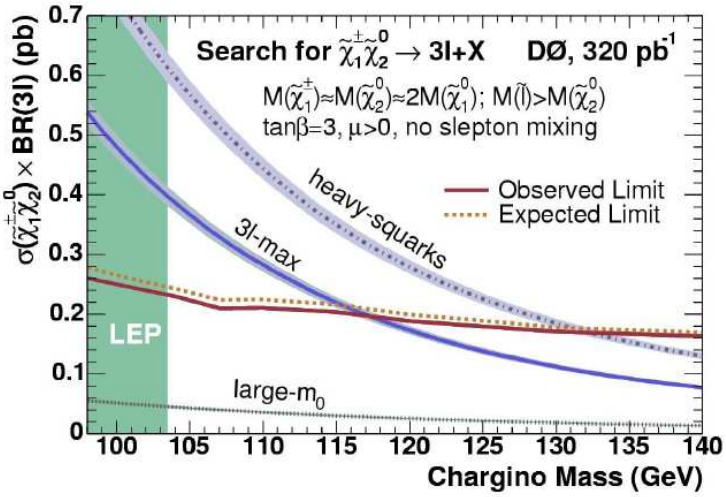

Figure 3.10: Experimental limits on branching ratios for chargino and neutralino decay into three leptons as a function of chargino mass at TEVATRON (RUN II a): 3l-max indicates the limit obtained when the slepton mass is almost degenerate with the $\tilde{\chi}_2^0$; heavy-squark indicates the limit when the destructive contribution to the t process via squark exchange is minimum due to the large squark mass; large m_0 indicates that for these values the slepton mass is very large while the probability decay into leptons is small; dashed lines are relative to expected limit, full lines represent experimental limits.

3.1.2 Other constraints

Besides the LEP and Tevatron constraints on supersymmetry there are those imposed by measurement of $b \to s\gamma$ branching ratio [32] and of the anomalous magnetic moment of the muon [33]; they are processes which can receive contributions from radiative corrections involving some supersymmetric particles. Such measurements, when compared with the Standard Model predictions, allow to obtain the forbidden or preferred regions in $m_0 - m_{1/2}$ plane for fixed tanβ, A, μ as showed in figure 3.11: in medium (green) shading is reported the forbidden region given by the first process, in medium (pink) shading band the 2σ preferred region by the second one.

Finally other constraints come from cosmology, in particular from data of WMAP (**Wilkinson Microwave Anisotropy Probe**) experiment which is a mission designed to determine the geometry, content and evolution of the universe by studying the full sky map of the temperature anisotropy of the cosmic microwave background radiation.

WMAP data reveal that the content of the Universe (cfr. fig. 3.12) includes 4% atoms, the bricks of stars and planets. Dark matter, different from atoms, does not emit or absorb light and it has only been detected indirectly by its gravity. It comprises 22% of the Universe. 74% of the Universe is composed of dark energy that acts as a sort of anti-gravity and, distinct from dark matter, is responsible for the present-day acceleration of the universal expansion. Before talking about the WMAP results and how they are related to Supersymmetry is useful to introduce some ideas. Specifically, WMAP provides a measurement of the matter density [34] of the universe, $\Omega_m h^2 = 0.135^{+0.008}_{-0.009}$, and the baryon density, $\Omega_b h^2 = 0.0224 \pm 0.0009$, where $\Omega_{m,b} = \rho_{m,b}/\rho_c$ where $\rho_{m,b}$ is the matter (baryon) density, ρ_c is the mass density needed to close the Universe, h is the Hubble parameter in units of 100 km/s/Mpc. Assuming that the difference of the two is practically (WMAP data tell us that very little of dark matter can be hot neutrino or warm gravitino/photino dark matter) cold dark matter (CDM), one finds that the relic CDM density in the universe, according to WMAP data, is given by $\Omega_{CDM} h^2 = 0.1126^{+0.008}_{-0.009}$: that is about 85% of matter in the universe is cold dark matter. Supersymmetry gives us possible dark matter candidates with the following explanation: in the very early universe high energetic processes occurred frequently creating among others SUSY particles. Most of these would be, after a while, decayed to LSPs and these, in their turn, could again annihilate to new particles creating an equilibrium. This process stopped (freeze-out) when the density in the universe got too low. Some requirements for SUSY dark matter candidates are therefore the following: it should not decay and should only interact through gravity and weak

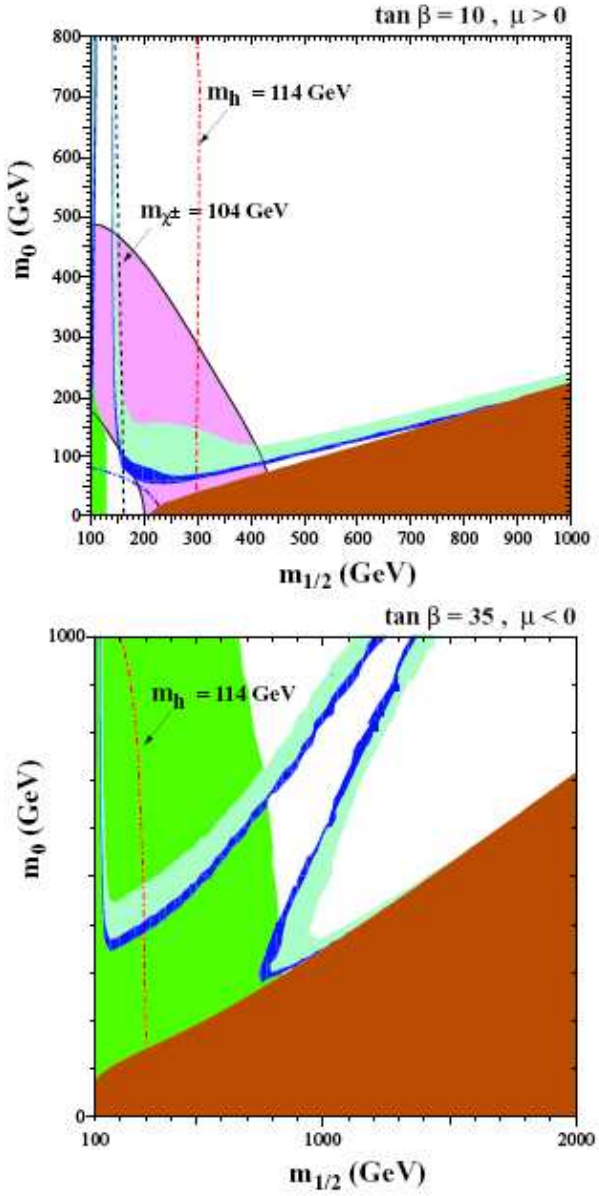

Figure 3.11: The ($m_{1/2}$; m_0) planes for (a) tan$\beta = 10$, $\mu > 0$, (b) tan$\beta = 35$, $\mu < 0$. In each panel, the region allowed by the older cosmological constraint $0.1 \leq \Omega_\chi h^2 \leq 0.3$ has medium shading, and the region allowed by the newer cosmological constraint $0.094 \leq \Omega_\chi h^2 \leq 0.129$ has very dark shading. The disallowed region where $m_{\tilde{\tau}_1} < m_\chi$ has dark (red) shading. The regions excluded by $b \to s\gamma$ have medium (green) shading, and those in panels (a) that are favoured by $g_\mu - 2$ at the 2-σ level have medium (pink) shading. A dot-dashed line in panel (a) delineates the LEP constraint on the $\tilde{e}$ mass and the contours $m_{\chi^\pm} = 104$ GeV ($m_h = 114$ GeV) are shown as near-vertical black dashed (red dot-dashed) lines in panel (a) (each panel).

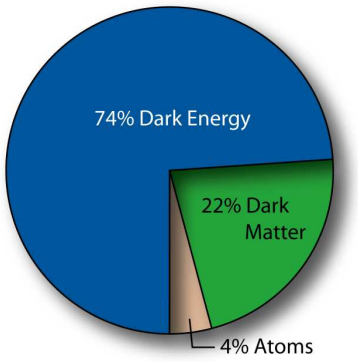

Figure 3.12: Universe content as obtained by WMAP experiment.

force: it is clear the best SUSY candidate is the $\tilde{\chi}_1^0$ in R-parity conserving models and the constraint on relic density becomes

$$0.094 \lesssim \Omega_\chi h^2 \lesssim 0.129 \text{ [35]}$$

where $\Omega_\chi \sim \frac{m_\chi}{\sigma_{ann}(\chi\chi\to\ldots)}$ and the typical annihilation[1] cross section is $\sigma_{ann} \sim 1/m_\chi^2$. In this way one can obtain as showed again in figure 3.11 the cosmologically preferred regions in light (turquoise) shaded area.

3.2 SUSY at LHC

Surely, the first motivation of the LHC physics program is to discover the Higgs boson, the scalar particle responsible for the mechanism of electroweak symmetry breaking. This particle, as suggested by theory, is supposed to have a mass less than about 1 TeV and could explain elegantly the observed mass spectrum of the Standard Model particles. Nevertheless, it has been already said in chapter 1 that, the SM can not be the ultimate theory (for example it suffers for the fine tuning problem), so the search for new physics phenomena remains anyway the main aim of the new experiments at LHC, in particular for the general purpose experiments as ATLAS and CMS. The best candidate for new physics models is undoubtedly Supersymmetry but it is not possible to completely exclude from search other theoretical frameworks like for example the Universal Extra

[1] annihilation processes are needed otherwise the relic the number of neutralinos would be too large and so the relic density.

Dimension (UED); moreover, Supersymmetry itself is described by several models and also for a given model the particle phenomenology (masses, decays, couplings etc.) could change for any of the infinite choices of the parameters. It is clear, therefore, that the first goal of the experiments at LHC is to show some deviation on what expected from Standard Model previsions through inclusive studies: they will allow to perform a first discrimination among the candidate models and will determine the future search strategies.

3.2.1 Inclusive searches

In figure 3.13 are reported the cross section as a function of the SUSY mass scale for supersymmetric production processes as expected at LHC.

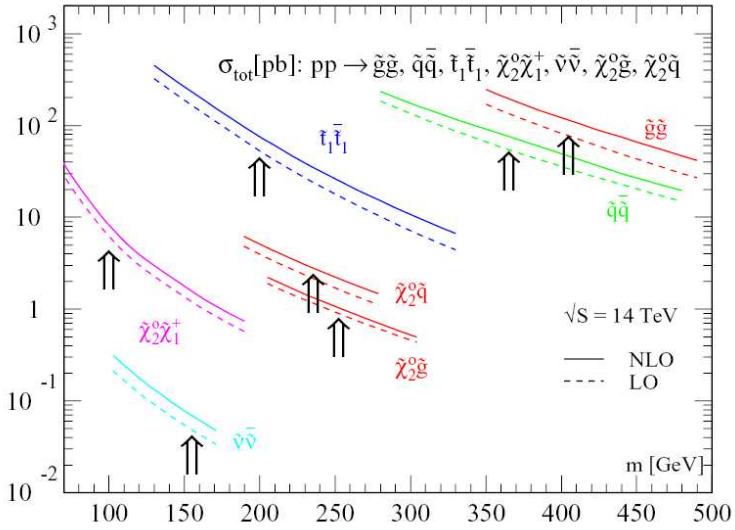

Figure 3.13: SUSY production cross sections as a function of sparticle masses foreseen at LHC: full lines (LO) indicate cross sections evaluated by taking into account the leading order perturbative QCD calculations; dashed lines indicate next-to leading order QCD perturbative evaluation.

The SUSY particles have the same couplings of Standard Model partners so SUSY events are dominated by production of colored gluinos and squarks: as it is possible to observe in figure 3.14 the production cross section for gluinos and squarks would be about 50 pb if the SUSY mass scale were of the order of 500 GeV and about 1 pb in case the mass scale were 1 TeV.

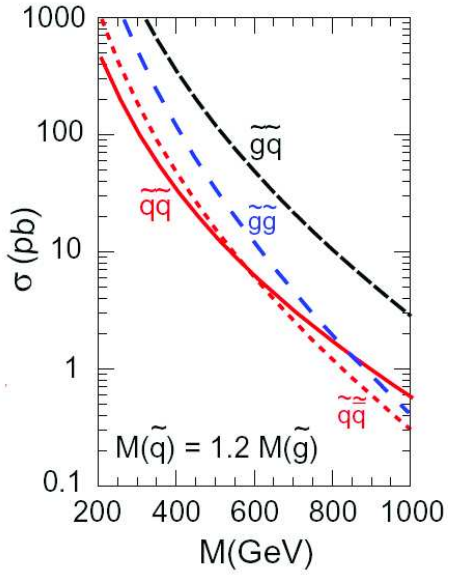

Figure 3.14: Main susy cross sections at LHC as a function of sparticle masses.

The main production processes are listed below:

- $q_i\bar{q}_i \rightarrow \tilde{g}\tilde{g}$;
- $gg \rightarrow \tilde{g}\tilde{g}$;
- $q_i q_j \rightarrow \tilde{q}_i\tilde{q}_j$
- $q_i\bar{q}_j \rightarrow \tilde{q}_i\bar{\tilde{q}}_j, (i \neq j)$;
- $q_i\bar{q}_i \rightarrow \tilde{q}_i\bar{\tilde{q}}_i$;
- $gg \rightarrow \tilde{q}_i\bar{\tilde{q}}_i$;
- $gq_i \rightarrow \tilde{g}\tilde{q}_i$ e $g\bar{q}_i \rightarrow \tilde{g}\bar{\tilde{q}}_i$;

where i,j denote the flavour indexes and, for simplicity, the chirality of squarks ($\tilde{u}$, $\tilde{d}$, $\tilde{s}$, $\tilde{c}$, $\tilde{b}_1$, $\tilde{b}_2$, $\tilde{t}_1$ and $\tilde{t}_2$) has been omitted.

An important feature for what we are going to study in this work is that, being LHC a proton-proton collider, more squarks and gluinos ($\tilde{q}$,$\tilde{g}$) than their corresponding antiparticles (namely $\bar{\tilde{q}}$,$\bar{\tilde{g}}$) will be

produced: this follows by the parton distribution functions for quarks and antiquarks as shown in figure 3.15.

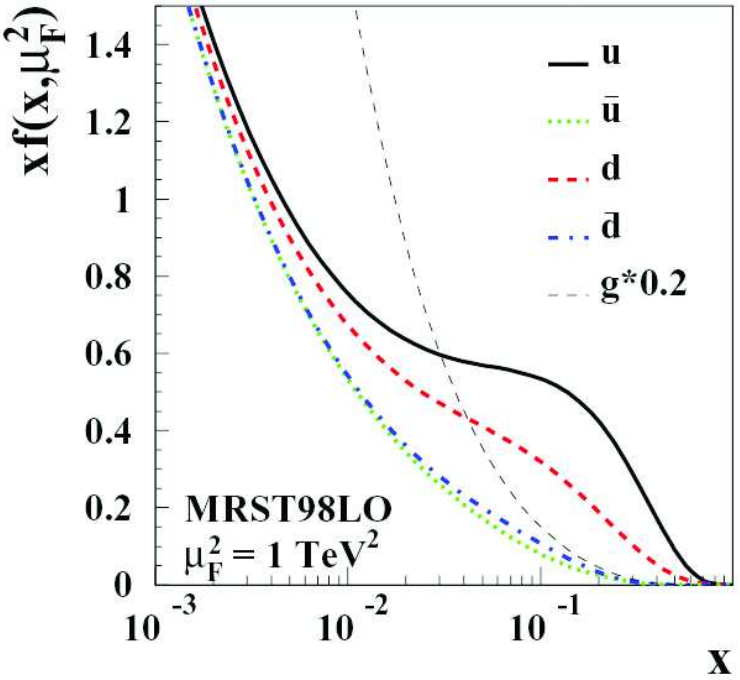

Figure 3.15: Parton distribution functions at LHC.

If R-parity is assumed to be conserved in mSUGRA model, then the produced SUSY particles will decay through one or more steps to the LSP which, if identified with the $\tilde{\chi}_1^0$, can only interact weakly thus escaping from detection. Thus supersymmetric events will be characterized by an excess of missing transverse energy in comparison with the Standard Model one, in association or not with multiple jets and/or leptons. The figure 3.16 shows, for example, missing transverse energy (E_T^{miss}) distributions for several Standard Model processes and for SUSY events at different SUSY mass scales: it can be seen that the smaller SUSY mass scale is, the bigger missing energy excess with respect to SM will be; in particular, at a mass scale of the order of 1.5 TeV the E_T^{miss} distribution is practically covered by the SM one because of the decreasing cross section.

It is easy to understand that a good signal significance can be achieved by optimizing the E_T^{miss} cut depending on the SUSY mass scale and therefore on mSUGRA parameters: as an example figure 3.17 shows, for given tan$\beta = 10$, $A = 0$, $\mu > 0$, the best missing E_T cut (measured in GeV) in the

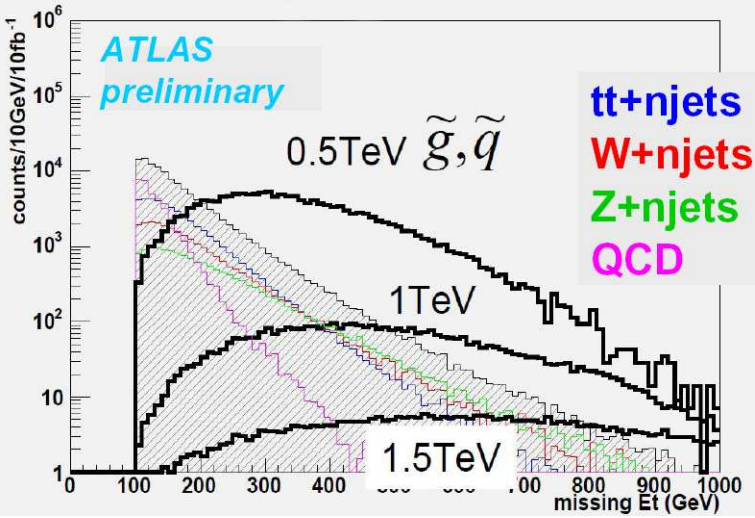

Figure 3.16: Missing transverse energy in the ATLAS detector for SUSY and SM at different susy mass scales.

$m_{1/2} - m_0$ plane. The optimal missing E_T is higher ($\mathcal{O}(1$ TeV $)$) in the range from ~ 700 GeV up to ~ 1 TeV for the $m_{1/2}$ value, while is less sensitive to m_0 since the LSP mass ($m(\chi_1^0)$) holds roughly $\sim 1/2m_{1/2}$: this also explains the lower values of E_T^{miss} cuts at small $m_{1/2}$, while at very large $m_{1/2}$ the cut gets low because the production cross section significantly decreases as already noted.

Among the main inclusive signatures at LHC listed below:

- missing transverse energy plus jets (E_T^{miss});
- missing transverse energy plus jets with lepton veto ($0l$);
- missing transverse energy plus jets plus one lepton ($1l$);
- missing transverse energy plus jets plus two opposite sign leptons ($2lOS$);
- missing transverse energy plus jets plus two same sign leptons ($2lSS$);
- missing transverse energy plus jets plus three leptons ($3l$);

the most powerful and model independent is surely the first one, as it is possible to observe in the ($m_0 - m_{1/2}$) reach plot (ATLAS 5σ discovery potential) in figure 3.18 (left) at an integrated

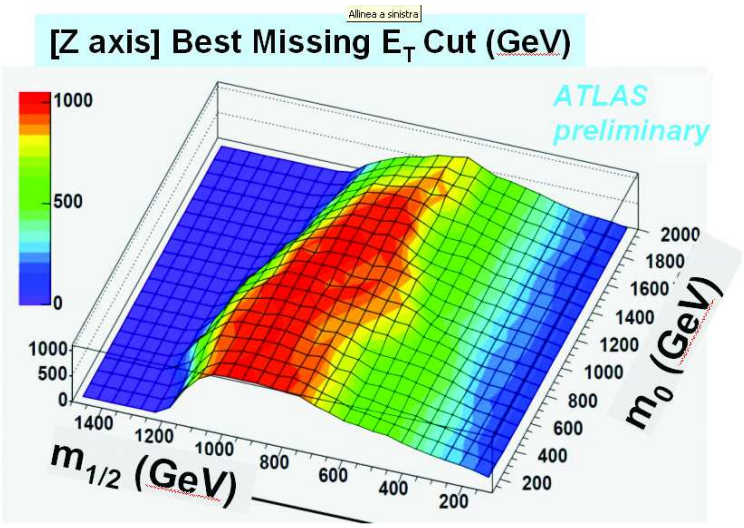

Figure 3.17: 3D plot showing the best cut on missing transverse energy in the $m_0 - m_{1/2}$ plane.

luminosity of 10 fb^{-1} (corresponding to 1 year of LHC data taking at the initial luminosity of 10^{33} cm^{-2}s^{-1}) and at fixed mSUGRA parameters, tan$\beta = 10$, $\mu > 0$, $A = 0$.

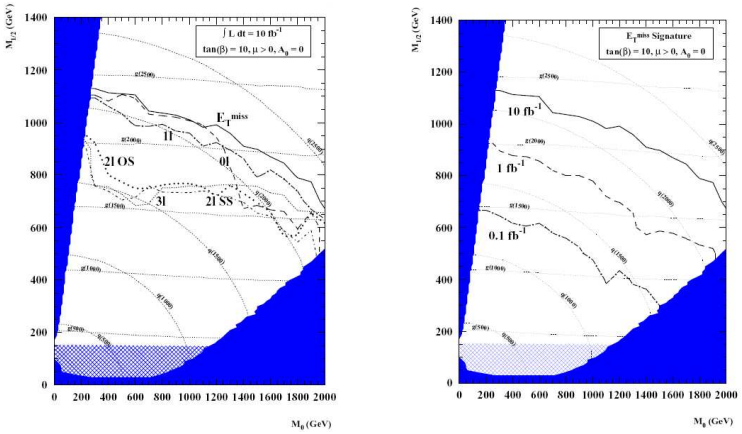

Figure 3.18: (left) Reach for $S/\sqrt{B} > 5$ for various SUSY inclusive signatures in the mSUGRA parameter space: in particular are given tanβ, $sign(\mu)$, A_0. E_T^{miss} plus jets, with or without requirements on leptons, then 1 lepton, 2 Same Sign leptons, 2 Opposite Sign leptons, 3 leptons. The most promising signature is represented by missing E_T plus jets; (right) the same plot but only for E_T^{miss} plus jets and as a function of integrated luminosity (that is as a function of data taking time).

Similarly figure 3.18 (right) shows the ATLAS discovery potential, at the same fixed mSUGRA

parameters, as a function of integrated luminosity relative just to the most promising signature, namely E_T^{miss} plus jets. It is therefore evident that in an ideal case with 0.1fb^{-1}, 1fb^{-1} and 10fb^{-1} (corresponding to roughly "one week", "one month" and "one year" of data taken respectively) it will be possible to obtain a mass reach of ~ 1.3 TeV, ~ 1.8 TeV and ~ 2.2 TeV respectively; in any case the ultimate reach is in the $2.5 - 3$ TeV region. Obviously these time scales are limited by a long time needed to understand detector performance (missing E_T tails, lepton identification, correct jet energy reconstruction, energy resolution, position of cracks etc.) and by time to collect enough statistic of SM control samples (W,Z plus jets, $t\bar{t}$) to correctly evaluate the background. Once Supersymmetry is discovered through inclusive signals, it will be interesting to simply estimate the SUSY masses involved, defined as it follows [38]:

$$M_{SUSY} = \frac{\sum_i \sigma_i m_i}{\sum_i \sigma_i}$$

where[2] m_i, σ_i are the masses of initial SUSY particles (two per event if R-parity conservation is assumed) and their production cross sections respectively. For this purpose is useful the "effective mass" variable

$$M_{eff} = E_T^{miss} + P_T^{(1)} + P_T^{(2)} + P_T^{(3)} + P_T^{(4)}$$

which is the scalar sum of the missing energy and the transverse momenta of the four hardest jets. In figure 3.19 is showed an example of M_{eff} distribution for SM and SUSY events corresponding to a mass scale of ~ 1 TeV.

The peak of the effective mass distribution is correlated to the SUSY mass scale (the area under the peak is correlated to SUSY cross section instead) and moves with it: so the scatter plot in figure 3.20 provides a measure of the mass scale of the strongly produced SUSY particles obtained by estimating the peak in M_{eff} by a gaussian fit to the background-subtracted signal distribution on a random set of models (several choices of the parameters) for mSUGRA and MSSM.

The correlation is excellent for mSUGRA and only acceptable for MSSM with uncertainties, due to intrinsic spread from model parameters, after one year at high luminosity (100fb^{-1}), of 2% and 10% for mSUGRA and MSSM respectively.

[2] If the LSP is of similar mass to the strongly interacting states one needs to correct the definition in the following way:

$$M_{SUSY}^{eff} = \left(M_{SUSY} - \frac{M_\chi^2}{M_{SUSY}} \right)$$

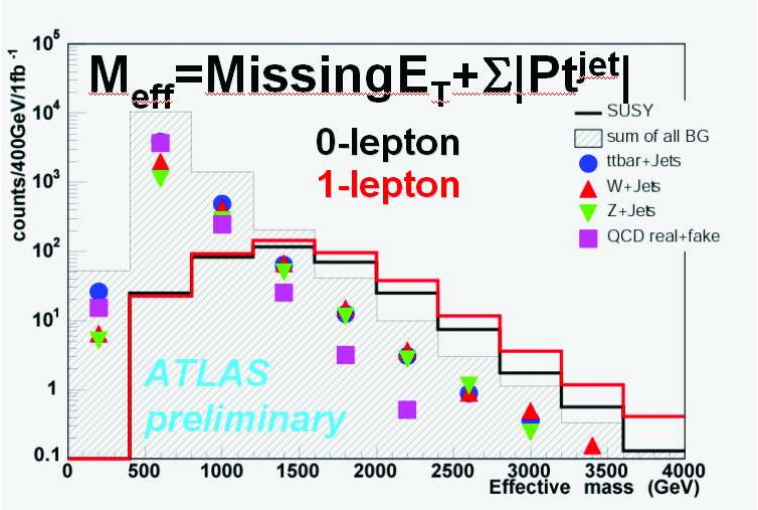

Figure 3.19: Effective mass distributions for SUSY and SM at 1 TeV of mass scale (for 0 lepton and 1 lepton signatures).

3.2.2 Exclusive searches

If inclusive studies show any deviation from Standard Model, once fixed the hypothetical SUSY mass scale, it will be necessary to verify if the new physics is actually Supersymmetry or rather something else. For this purpose one must demonstrate that:

- every SM particle has a superpartner;
- the spin of superpartners differs by a $1/2$ factor;
- their gauge quantum number and their couplings are identical;
- mass relations predicted by SUSY hold;
- finally one can measure the model parameters, opportunely scanning the parameter space of the most predictive models (like mSUGRA);

this is possible through precise measurements of masses, branching ratios, cross sections, angular distributions and so on. For what concerns the mass measurements, if R-parity conservation is assumed, there will be two undetected LSPs per event in the final state so that the invariant mass

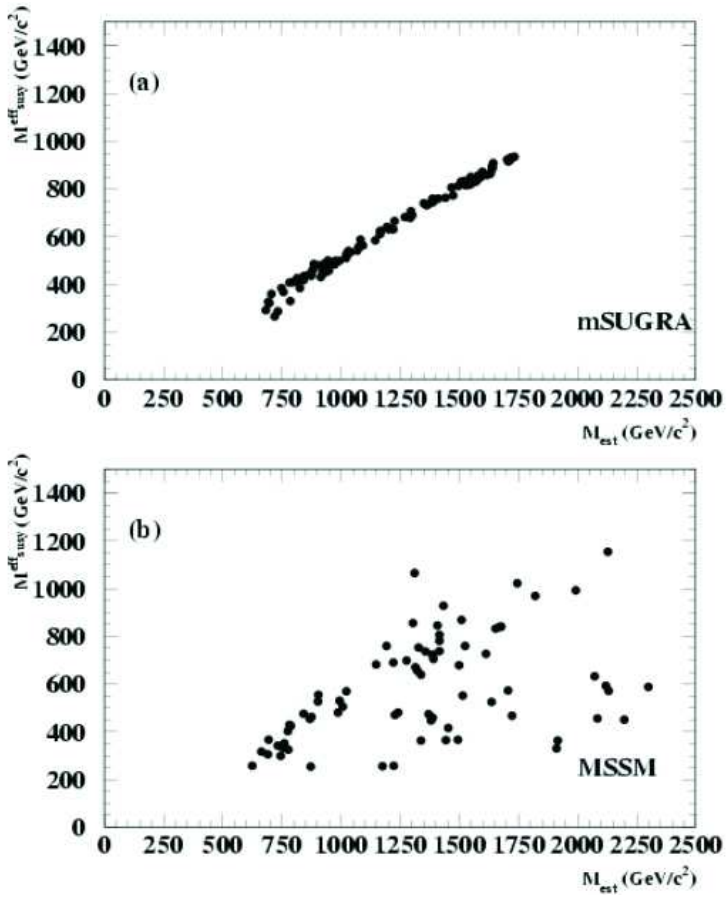

Figure 3.20: Correlation scatter plot between the effective mass scale and the SUSY mass scale for mSUGRA (5 parameters) and MSSM (constrained, 15 parameters).

distributions will not present any peak, but only kinematic edges and endpoints.
There are many works (see for instance [39] and [40]) which describe how to measure, in very long chains with at least three two-body decays, masses and momenta of involved supersymmetric particles in a model-independent way.

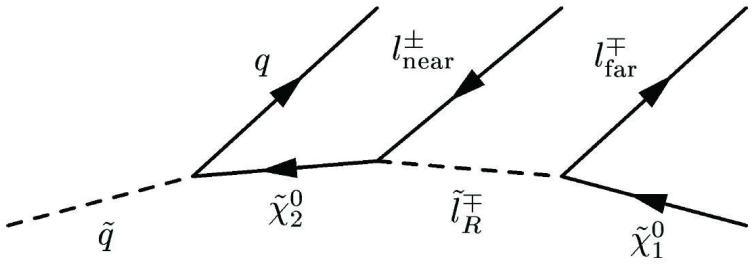

Figure 3.21: An example of a possible SUSY decay chain.

Such a decay chain is the one in figure 3.21 which is possible to schematize like a sequential cascade of successive two-body decays where, as defined in [39], the "near" lepton is the first emitted in the chain and the "far" lepton is the second one. If, for example, one wants to analytically evaluate the endpoint in the invariant mass distribution of the $l^{near}l^{far}$ system it is possible to operate in the following way:

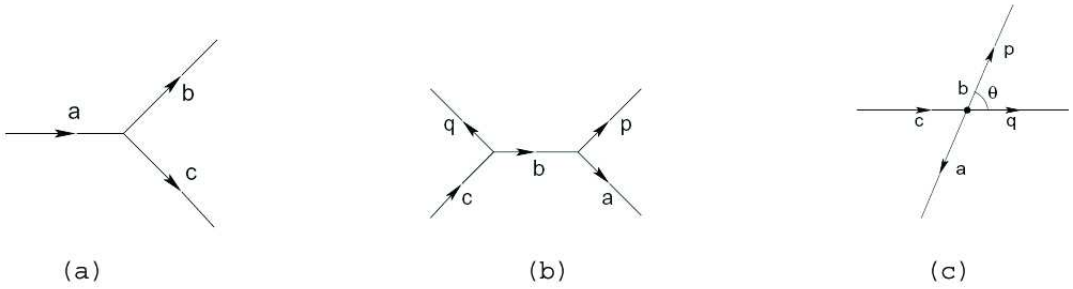

Figure 3.22: Useful diagrams.

referring to figure 3.22 (b) and identifying $p, q \equiv l^{near}, l^{far}$, $c \equiv \tilde{\chi}^0_2$, $b \equiv \tilde{l}_R$ and $a \equiv \tilde{\chi}^0_1$ we can write in the rest frame of particle b (figure 3.22 (c)):

$$m^2_{qp} = (E_q + E_p)^2 - (\vec{p}_q + \vec{p}_p)^2 = m^2_q + m^2_p + 2(E_q E_p - |\vec{p}_q||\vec{p}_p| \cos\theta)$$

and it has maximum value when q and p are back-to-back, so:

$$(m_{qp}^{max})^2 = m_q^2 + m_p^2 + 2(E_q E_p + |\vec{p}_q||\vec{p}_p|)$$

By considering the SM particles as massless (in particular the two leptons) we get

$$(m_{qp}^{max})^2 = 2(E_q E_p + |\vec{p}_q||\vec{p}_p|) = 4E_q E_p = 4|\vec{p}_q||\vec{p}_p|$$

To evaluate the momenta of leptons we refer to figure 3.22 (a) in the rest frame of particle a:

$$\vec{p}_b + \vec{p}_c = 0 \Rightarrow |\vec{p}_b| = |\vec{p}_c| = |\vec{p}|$$

$$m_a^2 = (p_b + p_c)^2 = (E_b + E_c)^2; \quad m_a^2 = m_b^2 + m_c^2 + 2|\vec{p}|^2 + 2\sqrt{m_b^2 + |\vec{p}|^2}2\sqrt{m_c^2 + |\vec{p}|^2}$$

and solving for $|\vec{p}|$ we get

$$|\vec{p}|^2 = [m_b^2, m_a^2, m_c^2] \equiv \frac{m_b^4 + m_a^4 + m_c^4 - 2(m_b^2 m_a^2 + m_b^2 m_c^2 + m_a^2 m_c^2)}{4m_a^2}$$

In conclusion

$$(m_{qp}^{max})^2 = 4|\vec{p}_q||\vec{p}_p| = 4\sqrt{[0, m_{\tilde{\ell}_R}^2, m_{\tilde{\chi}_1^0}^2]}\sqrt{[0, m_{\tilde{\ell}_R}^2, m_{\tilde{\chi}_2^0}^2]} \Rightarrow (m_{\ell\ell}^{max})^2 = \frac{(m_{\tilde{\chi}_2^0}^2 - m_{\tilde{\ell}_R}^2)(m_{\tilde{\ell}_R}^2 - m_{\tilde{\chi}_1^0}^2)}{m_{\tilde{\ell}_R}^2}$$

where $(m_{\ell\ell}^{max})$ represents the value of the endpoint in the $\ell\ell$ invariant mass distribution which can be experimentally evaluated by a triangular resolution fit, smeared by a gaussian, as showed in figure 3.23.

In a similar way (see for example [39] and [41]) one can get all of the relations in table 3.24 so that it is possible to obtain the values of masses of the supersymmetric particles involved in the chain by opportunely combining some of those. For what concerns the spin measurement by the study of angular distributions (related, as we will see later, to some invariant mass distribution) it is the main subject of this thesis and will be widely described in following chapter.

3.3 Supersymmetry in ATLAS

As already said mSUGRA is the most useful model in searching for supersymmetry because of the small number of free parameters. Anyway it would not be possible and useless to study all of

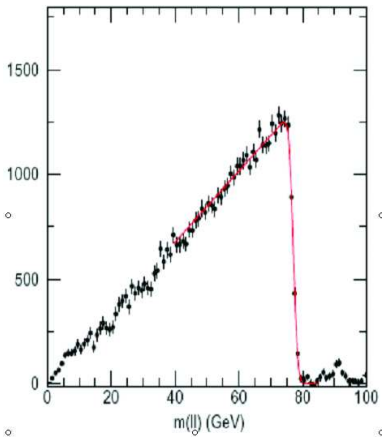

Figure 3.23: Dilepton inv mass distribution fitted with a triangle convoluted with a gaussian.

the infinite points in the mSUGRA parameter space: useful is instead to study some point having particular features. ATLAS collaboration has set these points in such a way to be compatible with the WMAP data on relic density of cold dark matter which is the most attractive motivation for SUSY, namely:

1. SU1, in the so-called *Coannihilation region* ($m_0 = 70$GeV; $m_{1/2} = 350$GeV; $A_0 = 0$; $\tan\beta = 10$; sign(μ)=+);
2. SU2, in the *Focus region* ($m_0 = 3000$GeV; $m_{1/2} = 215$GeV; $A_0 = 0$; $\tan\beta = 10$; sign(μ)=+);
3. SU3, in the *Bulk region* ($m_0 = 100$GeV; $m_{1/2} = 300$GeV; $A_0 = -300$; $\tan\beta = 6$; sign(μ)=+);
4. SU4, in the *Low Mass region* ($m_0 = 200$GeV; $m_{1/2} = 160$GeV; $A_0 = -400$; $\tan\beta = 10$; sign(μ)=+);
5. SU5x, which is called *Scan point* (m_0 in the range from 130 up to 4000 GeV; $m_{1/2} = 600, 1000$GeV; $A_0 = 0$; $\tan\beta = 10$; sign(μ)=+);
6. SU6, in the *Funnel region* ($m_0 = 320$GeV; $m_{1/2} = 375$GeV; $A_0 = 0$; $\tan\beta = 50$; sign(μ)=+).

Related edge	Kinematic endpoint
l^+l^- edge	$(m_{ll}^{\max})^2 = (\tilde{\xi} - \tilde{l})(\tilde{l} - \tilde{\chi})/\tilde{l}$
l^+l^-q edge	$(m_{llq}^{\max})^2 = \begin{cases} \max\left[\frac{(\tilde{q}-\tilde{\xi})(\tilde{\xi}-\tilde{\chi})}{\tilde{\xi}}, \frac{(\tilde{q}-\tilde{l})(\tilde{l}-\tilde{\chi})}{\tilde{l}}, \frac{(\tilde{q}\tilde{l}-\tilde{\xi}\tilde{\chi})(\tilde{\xi}-\tilde{l})}{\tilde{\xi}\tilde{l}}\right] \\ \text{except for the special case in which } \tilde{l}^2 < \tilde{q}\tilde{\chi} < \tilde{\xi}^2 \\ \text{and } \tilde{\xi}^2\tilde{\chi} < \tilde{q}\tilde{l}^2 \text{ where one must use } (m_{\tilde{q}} - m_{\tilde{\chi}_1^0})^2. \end{cases}$
Xq edge	$(m_{Xq}^{\max})^2 = X + \frac{(\tilde{q}-\tilde{\xi})}{2\tilde{\xi}}\left[\tilde{\xi} + X - \tilde{\chi} + \sqrt{(\tilde{\xi} - X - \tilde{\chi})^2 - 4X\tilde{\chi}}\right]$
l^+l^-q threshold	$(m_{llq}^{\min})^2 = \begin{cases} [\ 2\tilde{l}(\tilde{q}-\tilde{\xi})(\tilde{\xi}-\tilde{\chi}) + (\tilde{q}+\tilde{\xi})(\tilde{\xi}-\tilde{l})(\tilde{l}-\tilde{\chi}) \\ \quad -(\tilde{q}-\tilde{\xi})\sqrt{(\tilde{\xi}+\tilde{l})^2(\tilde{l}+\tilde{\chi})^2 - 16\tilde{\xi}\tilde{l}^2\tilde{\chi}}\ ]/(4\tilde{l}\tilde{\xi}) \end{cases}$
$l^\pm_{\text{near}}q$ edge	$(m_{l_{\text{near}}q}^{\max})^2 = (\tilde{q} - \tilde{\xi})(\tilde{\xi} - \tilde{l})/\tilde{\xi}$ (unobservable)
$l^\pm_{\text{far}}q$ edge	$(m_{l_{\text{far}}q}^{\max})^2 = (\tilde{q} - \tilde{\xi})(\tilde{l} - \tilde{\chi})/\tilde{l}$ (unobservable)
$l^\pm q$ high-edge	$(m_{lq(\text{high})}^{\max})^2 = \max\left[(m_{l_{\text{near}}q}^{\max})^2, (m_{l_{\text{far}}q}^{\max})^2\right]$
$l^\pm q$ low-edge	$(m_{lq(\text{low})}^{\max})^2 = \min\left[(m_{l_{\text{near}}q}^{\max})^2, (\tilde{q} - \tilde{\xi})(\tilde{l} - \tilde{\chi})/(2\tilde{l} - \tilde{\chi})\right]$
$\tilde{l}\bar{\tilde{l}}$ edge	$\Delta M^{\max} = (m_{\tilde{l}}^2 - m_{\tilde{\chi}_1^0}^2)/(2m_{\tilde{l}})$

Figure 3.24: The absolute kinematic endpoints of invariant mass quantities formed from decay chains of the types mentioned in the text for known particle masses. The following shorthand notation has been used: $\tilde{\chi} = m^2_{\tilde{\chi}_1^0}$, $\tilde{l} = m^2_{\tilde{l}_R}$, $\tilde{\xi} = m^2_{\tilde{\chi}_2^0}$, $\tilde{q} = m^2_{\tilde{q}}$ and X is m_h^2.

By looking again at the figures 3.11 are evident three main regions not excluded by WMAP data:
Coannihilation region (including SU1) is characterized by small values of m_0 with increasing values of $m_{1/2}$ (see dark blue line in the top figure 3.11 at small m_0). In this region the LSP ($\tilde{\chi}_1^0$) can co-annihilate with a non-LSP SUSY particle and such a process is enhanced when this latter is degenerated or very close in mass: thus LSP co-annihilate with the so-called Next Lightest Supersymmetric Particle (NLSP) which is usually the lighter $\tilde{\tau}$. Furthermore, in this region, the difference between right-handed and left-handed sleptons is small as well sleptons and first neutralinos mass difference so that usually leptons are very soft in energy.
Bulk region (including SU3) at small values of m_0 ($0 < m_0 < 100$ (GeV)) and $m_{1/2}$ ($100 < m_{1/2} < 200$ (GeV)) is another typical region in mSUGRA where LSP is bino-like and the LSP annihilation process through slepton exchange is enhanced because the right sleptons are sufficiently light: its name is due to the fact that in the very early studies on SUSY this was the widest region in the parameter space not excluded by WMAP. Only recently new WMAP results have reduced the region to a very narrow band.
Funnel region (including SU6) is clearly visible in the bottom figure 3.11 represented by the two dark blue lines forming a sort of way in the parameter space. At high value of tanβ, when the LSP mass is roughly half of the mass of a Higgs boson, it can take place the rapid annihilation of LSP through a resonant heavy Higgs exchange.
Focus region (including SU2) is visible in figure 3.25 and is characterized by a large value of m_0 and relatively small values of $m_{1/2}$. Furthermore, in this region, the LSP is mostly higgsino-like, unlike the most part of the parameter space, so that the LSP annihilation cross section through a virtual Z exchange enhances making therefore cosmologically acceptable the relic density of the LSP. Finally the SU4 point is called Low Mass point and it allows to continue the search for SUSY beyond the present limits set by TEVATRON Run II while SU5.X is called scan point because it is possible to study about ten similar points which differ each other, by the value of m_0 and only in few cases by the one of $m_{1/2}$. Some of ATLAS benchmark points are reported in figure 3.25.

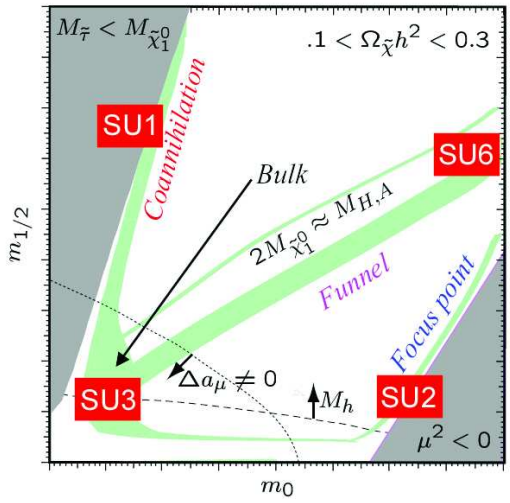

Figure 3.25: Benchmark points in the mSUGRA space parameter chosen by ATLAS collaboration for SUSY studies.

Chapter 4

Second lightest neutralino spin measurement

In this chapter I will illustrate the basic idea by which it is possible to get information about the second lightest neutralino ($\tilde{\chi}_2^0$) spin. The starting point is a particular decay chain, which is kinematically allowed for several mSUGRA regions: by studying suitable invariant mass distributions one can distinguish the zero-spin case from the $1/2$-spin case for $\tilde{\chi}_2^0$. After an introduction to the measurement method, it will be given the description of the kinematic features and the properties of the considered decay chain for the two benchmark points, namely SU1 in the stau-coannihilation region and SU3 in the bulk region of the allowed mSUGRA parameter space, studied to investigate the feasibility of such a spin measurement by performing fast simulation analyses (through the ATLAS software called ATLFAST). Then the topology of the signal events and the possible background sources (from both SUSY and SM channels), the event selection, the background studies, the invariant mass reconstruction and the charge asymmetry plots will be presented. Finally I will discuss the statistical methods used for estimating charge asymmetries and the final results on their detectability.

4.1 Spin measurement method

A very interesting decay chain (represented in figure 4.1), which allows the $\tilde{\chi}_2^0$ spin measurement, is the following:

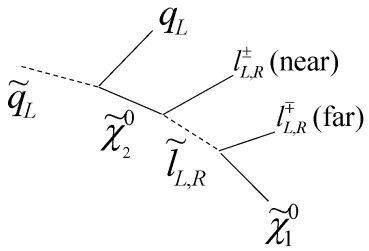

Figure 4.1: Decay chain considered for performing second lightest neutralino spin measurement: the first emitted lepton in the chain is named "near" lepton, the second is named "far" lepton.

$$\tilde{q}_L \;\rightarrow\; \tilde{\chi}_2^0\, q \;\rightarrow\; \tilde{l}^{\pm}_{L,R}\, l^{\mp}\, q \;\rightarrow\; l^+\, l^-\, q\;\; \tilde{\chi}_1^0\,, \tag{4.1}$$

in this chain the $\tilde{q}_L$ decays into $q_L\tilde{\chi}_2^0$ with $q_L = u_L, d_L, c_L, s_L$ followed by the $\tilde{\chi}_2^0$ decay into $\tilde{l}^{\pm}\, l^{\mp}$ where the slepton, in its turn, decays into $l^{\mp}\, \tilde{\chi}_1^0$ with $l = e, \mu$ and $\tilde{\chi}_1^0$ being the LSP. From now on we will refer to the first lepton emitted in the decay chain as "near" lepton and to the second one as "far" lepton (see [39]). According to MSSM, squarks and sleptons are scalar particles (spin-0 particles) so that their decays are spherically symmetric while the second lightest neutralino, $\tilde{\chi}_2^0$, is a spin-$1/2$ particle and its polarization is proved by a not isotropic angular distribution of its decay products. It is clear that spin measurement means to study a suitable angular variable distribution: referring to the figure 4.1 we define the angle θ^* between the quark (z axis) and near lepton in the $\tilde{\chi}_2^0$ rest frame. Assuming the SM particles as massless (this assumption is justified because at LHC the momenta are much greater than the mass of the SM particles) it is possible to verify ([42]) that that θ^* is connected to the near lepton-quark invariant mass:
considering for example the chain with the right-handed negative charged slepton we get

$$m^2_{q_L l^{near}} = (p+q)^2 \simeq 2\vec{p}\cdot\vec{q} = 2|\vec{p}||\vec{q}|(1-\cos\theta^*) = (m^{max}_{q_L l^{near}})^2 \sin^2\frac{\theta^*}{2}\,,$$

where

$$(m^{max}_{q_L l^{near}})^2 = 4|\vec{p}||\vec{q}| = (m^2_{\tilde{q}_L} - m^2_{\tilde{\chi}_2^0})(m^2_{\tilde{\chi}_2^0} - m^2_{\tilde{l}_R})/m^2_{\tilde{\chi}_2^0}$$

which represents, as already seen in chapter 3, the kinematic endpoint in the invariant mass distribution $m_{q_L l^{near}}$ and from which we can define the adimensional variable $\hat{m} = m_{q_L l^{near}}/m^{max}_{q_L l^{near}} = \sin\frac{\theta^*}{2}$. Now if the spin correlations, due to the $\tilde{\chi}^0_2$ spin, were ignored (spin-0 $\tilde{\chi}^0_2$ hypothesis) and particles were allowed to decay according to the only phase-space factor[1], then the angular probability would be

$$\frac{dP}{d\cos\theta^*} = \frac{1}{2}$$

that is a flat distribution where $1/2$ is a normalization factor. By performing a change of variable ($\cos\theta^* \rightarrow \hat{m}$) we get

$$\frac{dP}{d\cos\theta^*} = \frac{1}{2} \Rightarrow \frac{dP}{d\hat{m}} = \frac{1}{2}\left|\frac{d\cos\theta^*}{d\hat{m}}\right| = 2\hat{m}$$

so that we can now study an invariant mass distribution instead of an angular distribution. The behavior of this probability distribution is shown in figure 4.2 indicated with the black line: it

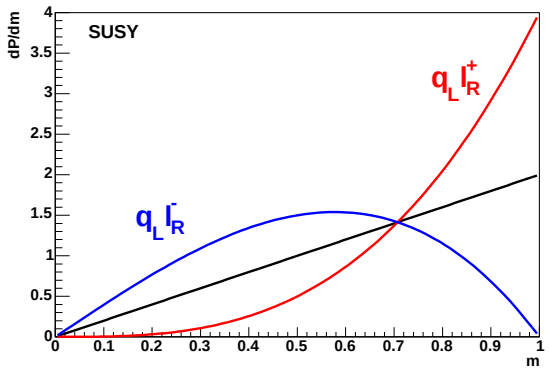

Figure 4.2: Idealised shapes of the ql^{near} invariant mass distributions in terms of the rescaled adimensional invariant mass variable $\hat{m}$. The solid balck line shows the case in which spin correlations due to the spin-1/2 of second lightest neutralino are ignored. Red and blue lines refer to ql^+ and ql^- systems respectively when spin correlations are taken into account.

is interesting to note that the invariant mass distribution has the same shape both for $q_L(l^+)^{near}$

[1]The decay probability for a process $P \rightarrow p\,q$ is given by $d\Gamma(P \rightarrow pq) = \frac{1}{2M}|\mathcal{M}|^2(2\pi)^4\delta^4(P - p - q)\frac{d^3\vec{p}}{(2\pi)^3 2E_p}\frac{d^3\vec{q}}{(2\pi)^3 2E_q}$. The angular behavior in our case is due to the $d\Omega$ factor when we write for example $d^3\vec{p} = p^2 dp d\Omega$.

and $q_L(l^-)^{near}$ systems, so that the invariant mass is charge (charge of the near lepton) symmetric. Taking into account the spin correlations we have to consider extra spin projection factors in the amplitude $|\mathcal{M}|^2 \propto |<\tilde{\chi}_2^0|l_R>|^2$. In the SM massless particles approximation the following relations hold:

$$l_L^{-(near)} = l_R^{+(near)} = \begin{pmatrix} 0 \\ 1 \end{pmatrix} \equiv |-\rangle\,;\;\; l_L^{+(near)} = l_R^{-(near)} = \begin{pmatrix} 1 \\ 0 \end{pmatrix} \equiv |+\rangle\,;$$

furthermore, referring to figure 4.3, it is clear that, being the $\tilde{q}_L$ a scalar particle, the $\tilde{\chi}_2^0$ has the

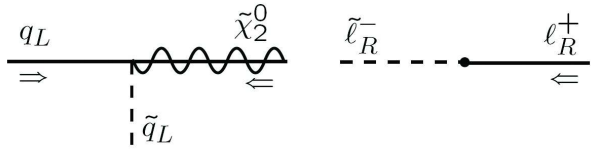

Figure 4.3: Scheme showing helicity of the involved particles.

same helicity (negative) as q_L so that, recalling that the z axis is taken to be the motion direction of the quark, we get

$$q_L = \begin{pmatrix} 0 \\ 1 \end{pmatrix} \equiv |-\rangle\,;\;\; \tilde{\chi}_2^0 = \begin{pmatrix} 1 \\ 0 \end{pmatrix} \equiv |+\rangle$$

Defining now the versor $\hat{n}$, motion direction of the near lepton $l_R^{+(near)}$, as

$$\hat{n} = \hat{i}\sin\theta\cos\phi + \hat{j}\sin\theta\sin\phi + \hat{k}\cos\theta$$

we can obtain the spin projection along the $\hat{n}$ direction

$$s_n = \vec{s}\cdot\hat{n} = \frac{i\hbar}{2}\vec{\sigma}\cdot\hat{n} = i\frac{\hbar}{2}\left(\sigma_x\sin\theta\cos\phi + \sigma_y\sin\theta\sin\phi + \sigma_z\cos\theta\right) =$$

$$i\frac{\hbar}{2}\begin{pmatrix} \cos\theta & \sin\theta\left(\cos\phi - i\sin\phi\right) \\ \sin\theta\left(\cos\phi + i\sin\phi\right) & -\cos\theta \end{pmatrix} =$$

$$i\frac{\hbar}{2}\begin{pmatrix} \cos\theta & \sin\theta e^{-i\phi} \\ \sin\theta e^{i\phi} & -\cos\theta \end{pmatrix}.$$

where $\vec{\sigma} = (\sigma_x, \sigma_y, \sigma_z)$ are the Pauli matrices[2]. The diagonalization of this matrix leads to the following eigenstates:

$$|+\rangle_n = \cos\frac{\theta}{2}\,|+\rangle + e^{i\phi}\sin\frac{\theta}{2}\,|-\rangle\,;$$
$$|-\rangle_n = \sin\frac{\theta}{2}\,|+\rangle - e^{i\phi}\cos\frac{\theta}{2}\,|-\rangle\,.$$

corresponding to the eigenvalues $s_n = \pm\frac{\hbar}{2}$ respectively. It follows that the spin correlation factors depend on the helicity of near lepton and quark:

$$|\langle\tilde{\chi}_2^0|\, l_R^{+(near)}\rangle|^2 = |\langle+|-\rangle_n|^2 = \sin^2\frac{\theta^*}{2},$$

for l^+q system (near lepton has the same helicity as quark) and

$$|\langle\tilde{\chi}_2^0|\, l_R^{-(near)}\rangle|^2 = |\langle+|+\rangle_n|^2 = \cos^2\frac{\theta^*}{2},$$

for l^-q system (near lepton has opposite helicity to quark) so that the angular probability distributions become:

$$\frac{dP}{d\cos\theta^*} = \sin^2\frac{\theta^*}{2} \quad \textit{for } l^+q \textit{ system}$$
$$\frac{dP}{d\cos\theta^*} = \cos^2\frac{\theta^*}{2} \quad \textit{for } l^-q \textit{ system}$$

Finally by performing again a change of variable we get

$$\frac{dP}{d\hat{m}} = 4\hat{m}^3 \qquad \textit{for } l^+q \textit{ system}$$
$$\frac{dP}{d\hat{m}} = 4\hat{m}(1-\hat{m}^2) \quad \textit{for } l^-q \textit{ system}$$

for the invariant mass probability distributions whose shapes are shown in figure 4.2 with red (in particular it is evident that near antileptons and quarks are preferentially emitted back-to-back) and blue lines respectively[3]. There are in this way two different shapes giving rise to a charge (charge

[2]
$$\sigma_x = \begin{pmatrix} 0 & 1 \\ 1 & 0 \end{pmatrix}; \quad \sigma_y = \begin{pmatrix} 0 & -i \\ i & 0 \end{pmatrix}; \quad \sigma_z = \begin{pmatrix} 1 & 0 \\ 0 & -1 \end{pmatrix}$$

[3]It must be noted that if the studied decay chain is originated by an antisquark $\tilde{\bar{q}}_L$ then the helicity of $\bar{q}_L$ and $\tilde{\chi}_2^0$ will be opposite to the case explained in the text:

$$\bar{q}_L = \begin{pmatrix} 1 \\ 0 \end{pmatrix} \equiv |-\rangle\,; \;\; \tilde{\chi}_2^0 = \begin{pmatrix} 0 \\ 1 \end{pmatrix} \equiv |+\rangle$$

of near lepton) asymmetry in the invariant mass distributions which is possible to experimentally measure by the following formula:

$$A^{+-} = \frac{s^+ - s^-}{s^+ + s^-}$$

where

$$s^{\pm} = \frac{d\sigma}{d(m_{l^{\pm(near)}q_L})}$$

Nevertheless there are some experimental difficulties which have to be taken into account in performing such a measurement:

- generally, it is not possible to distinguish experimentally near from far lepton so we must include contributions from both leptons when we build invariant mass distributions: this leads to a dilution effect in the lepton charge asymmetry;
- another dilution effect comes from the fact that we can not distinguish a left squark from a left antisquark decay chain: $m(\bar{q}l)$ and $m(ql)$ give rise to opposite charge asymmetry and, in the limit, if squarks and antisquarks were produced in the same quantity, then such an asymmetry would cancel exactly. Anyway LHC is a proton-proton collider so it will produce more squarks than antisquarks thanks to numerous u, d valence quarks (see fig. 3.15). Thus the dilution effect will depend on the squarks/antisquarks ratio.

4.2 SUSY production and kinematics

In the previous section it has been shown the method to obtain spin information by studying charge asymmetries in the lepton-quark invariant mass distributions $m(lq)$ for the particular decay chain

so that the spin correlation factors will be in this case:

$$|\langle\tilde{\chi}_2^0|\, l_R^{+(near)}\rangle|^2 = |\langle -|-\rangle_n|^2 = \cos^2\frac{\theta^*}{2},$$

for l^+q system and

$$|\langle\tilde{\chi}_2^0|\, l_R^{-(near)}\rangle|^2 = |\langle -|+\rangle_n|^2 = \sin^2\frac{\theta^*}{2},$$

for l^-q system.

In a very similar way it is possible to show that the charge asymmetry is opposite when we consider in the decay chain a left slepton instead of a right slepton.

in fig. 4.1. Such a decay chain is allowed for both analyzed mSUGRA points, SU1 and SU3, but with some differences mostly due to their production and kinematic features.

4.2.1 SU1 - Stau-coannihilation point

One of the cosmologically favoured regions (from WMAP data) in the mSUGRA parameter space is the coannihilation region which SU1 point belongs to. In this region the relatively small mass difference between the LSP $\tilde{\chi}_1^0$ and the lightest stau slepton $\tilde{\tau}_1$ allows stau-neutralino coannihilation processes which give an acceptable relic density of cold Dark Matter. The selected point, SU1, has the following mSUGRA parameters:

$$m_0 = 70GeV;\ m_{1/2} = 350GeV;\ A_0 = 0GeV;\ \tan\beta = 10;\ sign(\mu) = +.$$

Particle	Mass (GeV)
$\tilde{d}_L,\ \tilde{s}_L$	765
$\tilde{u}_L,\ \tilde{c}_L$	760
$\tilde{\chi}_2^0$	264
$\tilde{\mu}_L,\ \tilde{e}_L$	255
$\tilde{\mu}_R,\ \tilde{e}_R$	154
$\tilde{\chi}_1^0$	137

Table 4.1: Masses of sparticles involved in the studied decay chain for SU1

The LSP $\tilde{\chi}_1^0$ is purely bino-like so that annihilation processes through $W^{\pm}$ or Z boson exchange are not allowed. The leading order (LO) cross section for all SUSY production is $\sigma = 7.8$ pb and is dominated by squarks and gluinos production as shown in table 4.2.

The heaviest SUSY particle is gluino with mass $m(\tilde{g}) = 832$ GeV and the lightest SUSY particle is $\tilde{\chi}_1^0$ with a mass of 137 GeV (see table 4.1). One/two left squark/s is/are directly produced in $32\%/8\%$ of all SUSY events and can also be indirectly originated in 20% of all gluino decays. Furthermore the observability of charge asymmetry is enhanced by a ratio of about 5 in $\tilde{q}/\bar{\tilde{q}}$. Again from table 4.1 it is clear that, being the $\tilde{\chi}_2^0$ heavier than both left and right sleptons (selectrons and smuons), the second lightest neutralino can decay into both sleptons:

$$\tilde{q}_L \rightarrow \tilde{\chi}_2^0\, q \rightarrow \tilde{l}_{L,R}^{\pm}\, l^{\mp}\, q \rightarrow l^+\, l^-\, q\ \tilde{\chi}_1^0\,. \tag{4.2}$$

initial states	σ(pb)	%
$\tilde{q}_R\tilde{g}$	1.757	22
$\tilde{q}_L\tilde{g}$	1.620	21
$\tilde{q}_L\tilde{q}_R$	0.885	11
$\tilde{q}_R\tilde{q}_R$	0.779	10
$\tilde{q}_L\tilde{q}_L$	0.665	8
$\tilde{g}\tilde{g}$	0.554	7
$\tilde{\chi}_2^0\tilde{\chi}_1^\pm$	0.258	3.3
$\tilde{b}_1\tilde{b}_1$	0.160	2
$\tilde{\chi}_2^0\tilde{q}_L$	0.154	2
$\tilde{\chi}_1^\pm\tilde{\chi}_1^\pm$	0.140	1.8
$\tilde{t}_1\tilde{t}_1$	0.049	0.06
$\tilde{t}_2\tilde{t}_2$	0.038	0.05
$\tilde{b}_2\tilde{b}_2$	0.032	0.04
$\tilde{l}\tilde{l}$	0.015	0.02

Table 4.2: Main SUSY production cross sections for SU1

where $\tilde{q}_L = \tilde{u}_L, \tilde{d}_L, \tilde{s}_L, \tilde{b}_L$, $\tilde{l}_{L,R} = \tilde{\mu}_{L,R}$, $\tilde{e}_{L,R}$ and $l = \mu, e$. Branching ratios for the involved decays are:

$$BR(\tilde{q}_L \to q\tilde{\chi}_2^0) = 31.5\ \%, \quad BR\ (\ \tilde{\chi}_2^0\ \to\ \tilde{l}_L\, l\ ) = 6\ \%,$$
$$BR\ (\ \tilde{\chi}_2^0\ \to\ \tilde{l}_R\, l\ ) = 3\ \%, \quad BR(\tilde{l}_{L,R} \to \tilde{\chi}_1^0\, l) = 100\ \%.$$

and the decay 4.2 represents about 1.6% of all SUSY production. SU1 shows an interesting feature due to its mass spectrum: the mass difference between $\tilde{\chi}_2^0$ and left slepton as well the mass difference between $\tilde{l}_R$ and $\tilde{\chi}_1^0$ are small ($m(\tilde{\chi}_2^0) - m(\tilde{l}_L) \simeq 10$ GeV and $m(\tilde{l}_R) - m(\tilde{\chi}_1^0) \simeq 20$ GeV respectively) giving rise to very important consequences for what concerns the possibility to distinguish near from far leptons as we will see in next sections.

4.2.2 SU3 - Bulk point

Another cosmologically favoured region in the mSUGRA parameter space is the so-called bulk region which SU3 belongs to. If SUSY exists, in this region its discovery would be expected to be easy. Here an acceptable relic density of cold Dark Matter is obtained thanks to the lightest neutralino (mostly bino) annihilation processes via t-channel slepton exchange. The point SU3 considered for these studies has mSUGRA parameters:

$$m_0 = 100\ GeV, \quad m_{1/2} = 300\ GeV, \quad A_0 = -300\ GeV, \quad tan\beta = 6, \quad sgn\mu = + .$$

Total SUSY leading order cross section is $\sigma = 19.3$ pb and is dominantly characterized (as for

Particle	Mass (GeV)
$\tilde{d}_L$, $\tilde{s}_L$	636.3
$\tilde{u}_L$, $\tilde{c}_L$	631.5
$\tilde{\chi}_2^0$	218.6
$\tilde{\mu}_L$, $\tilde{e}_L$	230.4
$\tilde{\mu}_R$, $\tilde{e}_R$	155.5
$\tilde{\chi}_1^0$	117.9

Table 4.3: Masses of sparticles involved in the studied decay chain for SU3

SU1) by gluino and squark production (see table 4.4). Also in SU3 point gluino is the heaviest SUSY particle ($m(\tilde{g}) = 717$ GeV) while the lightest SUSY particle is $\tilde{\chi}_1^0$ with a mass of 118 GeV (see table 4.3). Left squarks ($\tilde{u}_L$, $\tilde{d}_L$,$\tilde{s}_L$, $\tilde{b}_L$) occur in 67% of all SUSY events and can be produced either directly or from gluino decay ($BR(\tilde{g} \rightarrow \tilde{q}_L q) = 23\%$) and the squarks/anti-squarks production ratio is 2.5. Differently from the SU1 point (see table 4.3), the mass of the second lightest neutralino ($m(\tilde{\chi}_2^0) = 219$ GeV) is smaller than left slepton mass ($m(\tilde{l}_L) = 230$ GeV) (see also mass spectrum in fig. 1.7). As a consequence, decays of $\tilde{\chi}_2^0$ to left sleptons are forbidden and only decays to right sleptons are allowed in the considered left squark decay chain:

$$\tilde{q}_L \rightarrow \tilde{\chi}_2^0 q \rightarrow \tilde{l}_R^{\pm} l^{\mp} q \rightarrow l^+ l^- q\ \tilde{\chi}_1^0 . \tag{4.3}$$

This decay chain represents the 3.8% of all SUSY production and each decay has following branch-

initial states	σ(pb)	%
$\tilde{q}_R\tilde{g}$	4.469	22.9
$\tilde{q}_L\tilde{g}$	4.426	22.7
$\tilde{q}_L\tilde{q}_R$	2.086	10.7
$\tilde{q}_R\tilde{q}_R$	1.833	9.4
$\tilde{q}_L\tilde{q}_L$	1.716	8.8
$\tilde{g}\tilde{g}$	1.540	7.9
$\tilde{t}_1\tilde{t}_1$	0.872	4.5
$\tilde{\chi}_2^0\tilde{\chi}_1^\pm$	0.507	2.6
$\tilde{\chi}_1^\pm\tilde{\chi}_1^\pm$	0.279	1.4
$\tilde{l}\tilde{l}$	0.230	1.2
$\tilde{\chi}_2^0\tilde{q}_L$	0.195	1
$\tilde{b}_1\tilde{b}_1$	0.156	0.8
$\tilde{b}_2\tilde{b}_2$	0.109	0.6
$\tilde{t}_2\tilde{t}_2$	0.068	0.4

Table 4.4: Main SUSY production cross sections for SU3

ing ratios:

$$BR(\tilde{q}_L \to q\tilde{\chi}_2^0) = 32\ \%,\ BR(\tilde{\chi}_2^0 \to \tilde{l}_R\, l) = 17.6\%,\ BR(\tilde{l}_{L,R} \to \tilde{\chi}_1^0\, l) = 100\ \%,$$

.

4.3 Montecarlo simulation

4.3.1 MC samples and analysis tools

Events have been generated using HERWIG 6.505 [43],[44],[45] by means of the ISAWIG [46] interface with mass spectra and decay rates of supersymmetric particles given by ISAJET 7.69 and ISAJET 7.64 for SU1 and SU3 points respectively. ISAJET [47] is a Monte Carlo program which simulates pp, $\bar{p}p$ and e^+e^- interactions at high energies. ISAJET is based on perturbative

QCD (it incorporates cross sections, initial state and final state QCD radiative corrections) plus phenomenological models for parton and beam jet fragmentation. SUSY samples corresponding to integrated luminosities $L = 100$ fb^{-1} (out of 220 fb^{-1} generated and used for MC truth studies only) for SU1 point and $L = 30$ fb^{-1} for SU3 point have been analyzed: this statistics has been obtained by adding all the available official Rome productions and privately generated samples produced at Tier 2 farm facility in Napoli. Fast simulation studies on the most relevant Standard Model (SM) background have been also performed. In particular the processes considered in this report are indicated with: $t\bar{t}+$ N jets, $W+$ N jets, $Z+$ N jets produced with Alpgen $2.0.5$ [49]; they will be widely described in next sections. Generated data were passed through the fast simulation software package of ATLAS detector (ATLFAST-00-01-74 package) [50] and then converted into AOD (Analysis Object Data) by ATHENA release 10.0.4. A first analysis and the conversion from AOD to ntuple is done, again in ATHENA, with SUSYPlot package (SUSYPhysAlgs-00-04-02) so that it is possible to perform the final analysis by using ROOT, an object-oriented data analysis Framework provided by CERN for physics analysis. In ATLFAST electrons and muons were required to have transverse momentum $p_T > 6$ GeV, pseudorapidity $|\eta| < 2.5$ and were considered isolated if the deposited transverse energy $E_T^{isol} < 10$ GeV within a cone $\Delta R = \sqrt{\eta^2 + \phi^2} = 0.2$. Jets were reconstructed with a jet-cone algorithm with $\Delta R = 0.4$ and the minimum jet p_T required was 15 GeV in a region $|\eta| < 5$.

4.3.2 Experimental signature of the signal events for both SU1 and SU3

A typical final state signature of left squark decay chains 4.2 and 4.3 is represented by:

- large missing transverse energy from escaping LSPs (there are two LSPs: at LHC SUSY particles can be produced in pair so one comes from the considered decay chain and the other from the rest of the SUSY event);
- high-p_T jets from the left squark decay and from the decay of squark/gluino produced with left squark;
- two **S**ame **F**lavour **O**pposite **S**ign (SFOS) leptons.

As already said in section 4.1 the first emitted lepton is indicated as near, the second one as far lepton. The near lepton mainly contributes to the charge asymmetry in the invariant mass distri-

butions $m(ql^{\pm})$ but generally it is not possible to distinguish such a particles as for example it happens for SU3 so we have to consider both contributions with the only effect of diluting the asymmetry. The particular kinematics of SU1 point, instead, allows to distinguish the two leptons by making suitable requirements on their p_T depending on what kind of slepton, left or right, is emitted in the chain: in fact by table 4.1 one can observe that for the decay chain involving the left slepton (from now on this decay chain will be called "left decay chain" for simplicity) the mass differences $m(\tilde{\chi}_2^0) - m(\tilde{l}_L)$ and $m(\tilde{l}_L) - m(\tilde{\chi}_1^0)$ hold 9 GeV and 118 Gev respectively so that the near lepton is softer than the far one; the the opposite happens for the decay chain involving the right slepton (from now on this decay chain will be called "right decay chain" for simplicity) where $m(\tilde{\chi}_2^0) - m(\tilde{l}_R)$ and $m(\tilde{l}_R) - m(\tilde{\chi}_1^0)$ hold 110 GeV and 17 Gev respectively (see fig. 4.4).

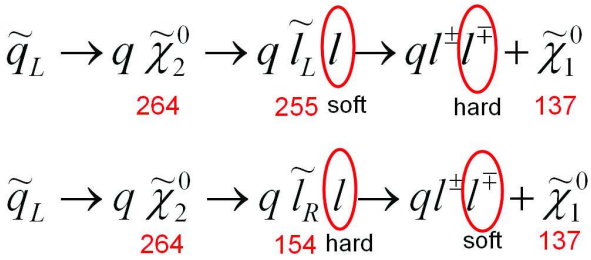

Figure 4.4: This scheme shows the masses of SUSY particles involved in the decay chain for SU1: in the chain with left slepton the near lepton is softer than far; the opposite happens for the decay chain with the right slepton.

The superimposed p_T distributions at truth level for near and far lepton (signal leptons of SU1 point) are shown in figure 4.5 for the left decay chain and in figure 4.6 for the right decay chain.

From these figures it is possible to note that for the left (right) decay chain the near lepton has a smaller (greater) p_T than the far lepton by a factor of over 100 GeV. Furthermore figures 4.7 show the distributions of p_T differences between near and far lepton for both the decay chain: near and far leptons are distinguishable with high probability according to their p_T; in particular one can select the near lepton of the left decay chain by observing that, event by event, $(p_T^{near} - p_T^{far}) < 0$ while the opposite, $(p_T^{near} - p_T^{far}) > 0$, holds in the case of the right decay chain.

Figure 4.8 shows that the previous considerations are not applicable for SU3 point: the mean values of the two distributions are very close and a requirement on the p_T differences does not allow to separate efficiently near and far lepton.

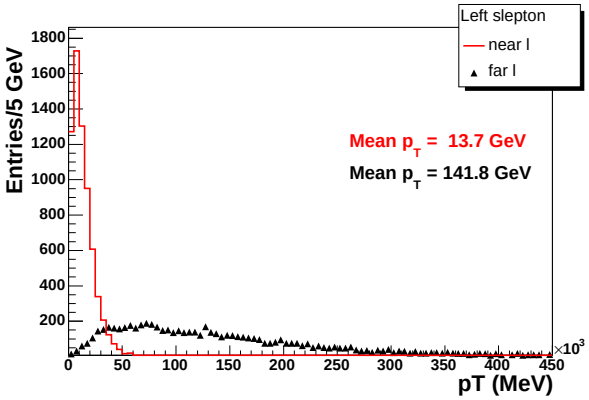

Figure 4.5: Superimposed p_T distributions at truth level for near and far lepton for the left decay chain of SU1: red line indicates near lepton p_T distribution; black triangles indicate far lepton p_T distribution.

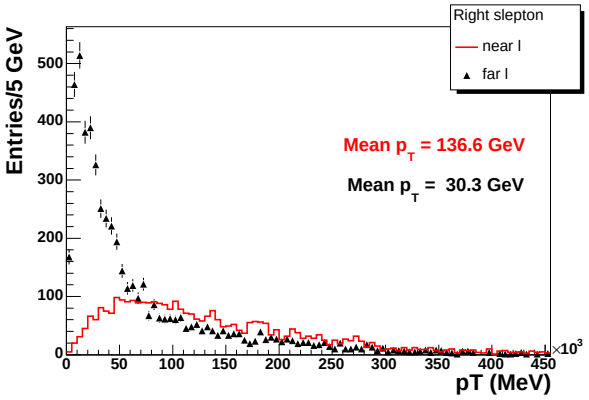

Figure 4.6: Superimposed p_T distributions at truth level for near and far lepton for the right decay chain of SU1: red line indicates near lepton p_T distribution; black triangles indicate far lepton p_T distribution.

4.3.3 Monte Carlo invariant mass distributions and charge asymmetries for SU1 and SU3

Starting from the three detectable particles l^+, l^-, q (where quark hadronizes to jet) in the final state of the left squark decay 4.2 or 4.3 four invariant masses can be formed: $m(ll)$, $m(qll)$, $m(ql^{near})$

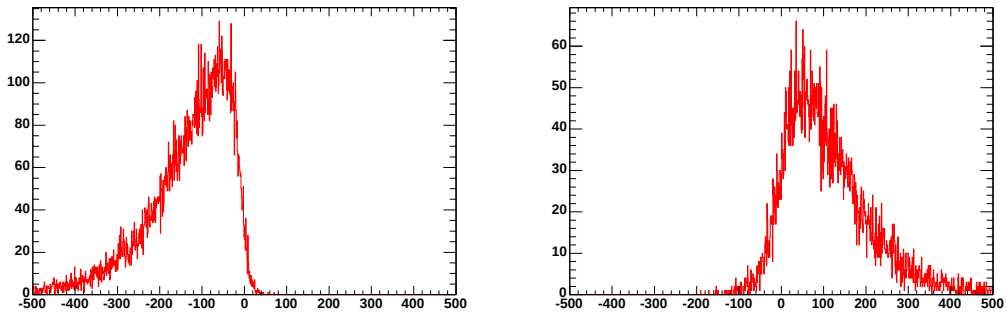

Figure 4.7: Distribution of p_T differences between near and far lepton ($P_T^{near} - P_T^{far}$): left plot refers to left decay chain; right plot refers to right decay chain.

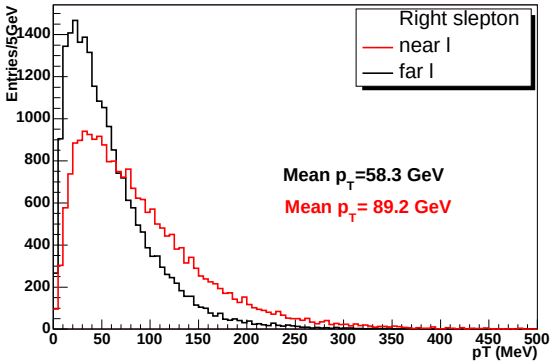

Figure 4.8: Superimposed p_T distributions at truth level for near and far lepton for the considered decay chain of SU3.

and $m(ql^{far})$. For each of them, expressions for kinematic maxima are given by (see table 3.24):

$$m(ll)^{max} = \left[\frac{(M^2_{\tilde{\chi}^0_2} - M^2_{\tilde{l}_{L,R}})(M^2_{\tilde{l}_{L,R}} - M^2_{\tilde{\chi}^0_1})}{M^2_{\tilde{l}_{L,R}}}\right]^{1/2} \tag{4.4}$$

$$m(qll)^{max} = \left[\frac{(M^2_{\tilde{q}_L} - M^2_{\tilde{\chi}^0_2})(M^2_{\tilde{\chi}^0_2} - M^2_{\tilde{\chi}^0_1})}{M^2_{\tilde{\chi}^0_2}}\right]^{1/2} \tag{4.5}$$

$$m(ql^{near})^{max} = \left[\frac{(M^2_{\tilde{q}_L} - M^2_{\tilde{\chi}^0_2})(M^2_{\tilde{\chi}^0_2} - M^2_{\tilde{l}_{L,R}})}{M^2_{\tilde{\chi}^0_2}}\right]^{1/2} \tag{4.6}$$

$$m(ql^{far})^{max} = \left[\frac{(M^2_{\tilde{q}_L} - M^2_{\tilde{\chi}^0_2})(M^2_{\tilde{l}_{L,R}} - M^2_{\tilde{\chi}^0_1})}{M^2_{\tilde{l}_{L,R}}}\right]^{1/2} \tag{4.7}$$

The corresponding values for these expressions depend on the mSUGRA point under consideration because the masses of involved sparticles change: such values are reported in table 4.5 for SU1 and SU3 points: in particular for SU1 point are present two different values (right and left) relative to the decay chain involving right or left slepton; for SU3 it is allowed only the decay chain involving right sleptons.

Masses	SU1		SU3
	Endpoint (GeV) *left*	*Endpoint* (GeV) *right*	*Endpoint* (GeV) *right*
$m_{l^+l^-}^{max}$	56.05	97.93	100.17
$m_{l^+l^-q}^{max}$	611.64	611.64	500.34
$m_{ql^{near}}^{max}$	180.14	580.09	417.74
$m_{ql^{far}}^{max}$	327.21	603.08	385.85

Table 4.5: Kinematic maxima of invariant mass distributions for SU1 and SU3.

When calculating endpoint values in table 4.5 the relative abundance of squarks was properly taken into account: in fact double more $\tilde{u}_L$ squarks than $\tilde{d}_L$ squarks is expected to be produced at the LHC proton-proton collider. Endpoints of $m(ll)$ and $m(qll)$ mass distributions for SU1 and SU3 points are clearly visible in figures 4.9 and 4.10.

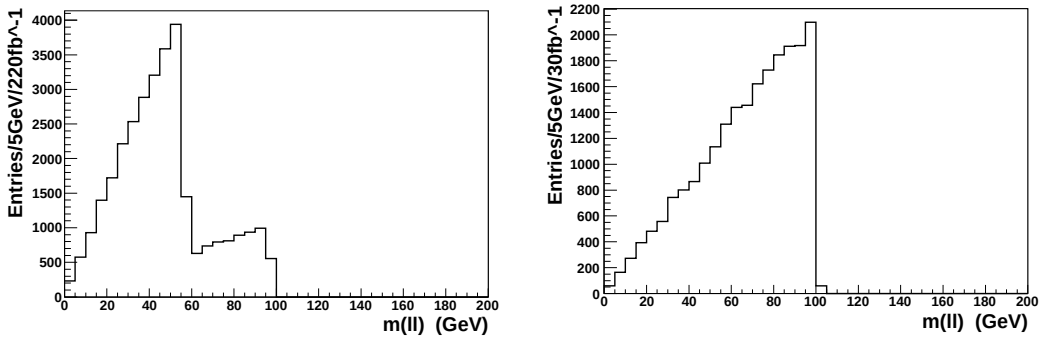

Figure 4.9: Dilepton invariant mass distributions: left plot shows the distribution for SU1 point; right plot shows the distribution for SU3 point.

In particular 4.9 (left plot) shows the two endpoints in the invariant mass distribution, close to 56 GeV and 100 GeV, respectively for left and right decay chain in SU1: this information (a suitable

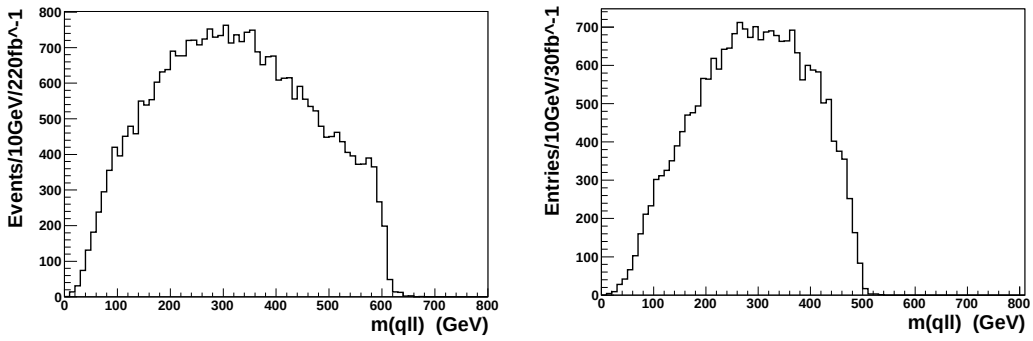

Figure 4.10: lepton-lepton-quark invariant mass distributions: left plot shows the distribution for SU1 point; right plot shows the distribution for SU3 point.

cut in the mass distribution allows to select left or right decay chain in the analysis) together with the requirements on p_T of leptons will allow to select, in the analysis, efficiently near and far lepton in both left and right decay chain under study. Truth level lepton-quark invariant mass distributions, with positively and negatively charged leptons superimposed, are illustrated for SU3 in figure 4.11 by considering both near and far contributions together; since for SU1 the two leptons are distinguishable figures 4.12 and 4.13 show, separately, distributions for ql^{near} and ql^{far} systems for both left and right decay chain.

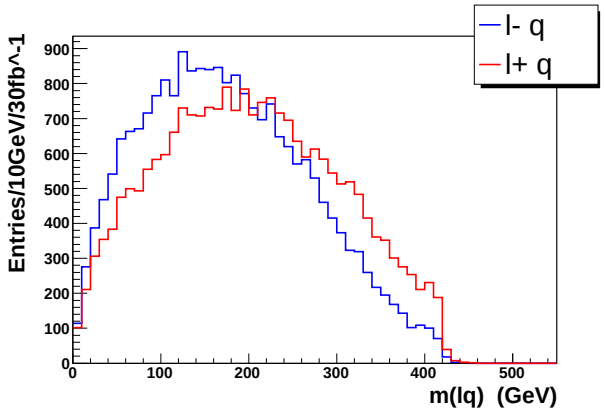

Figure 4.11: Truth level lepton-quark invariant mass distributions for SU3 point: red line refers to ql^+ system, blue line to ql^-.

As already said from lepton-quark invariant mass distributions it is possible to build the charge

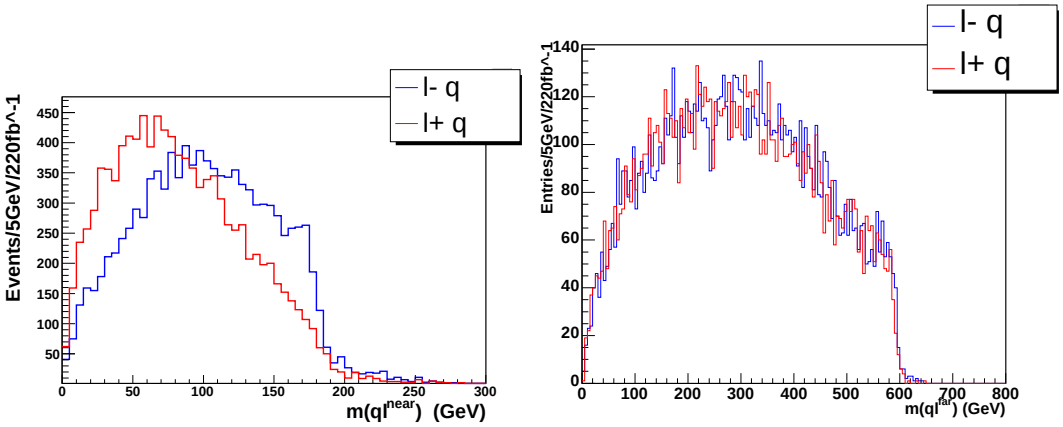

Figure 4.12: Truth level lepton-quark invariant mass distributions for SU1: red line refers to ql^+ system, blue line to ql^-. (left plot) shows the (near lepton, quark) contribution in the left decay chain; (right plot) shows the (far lepton, quark) contribution in the left decay chain.

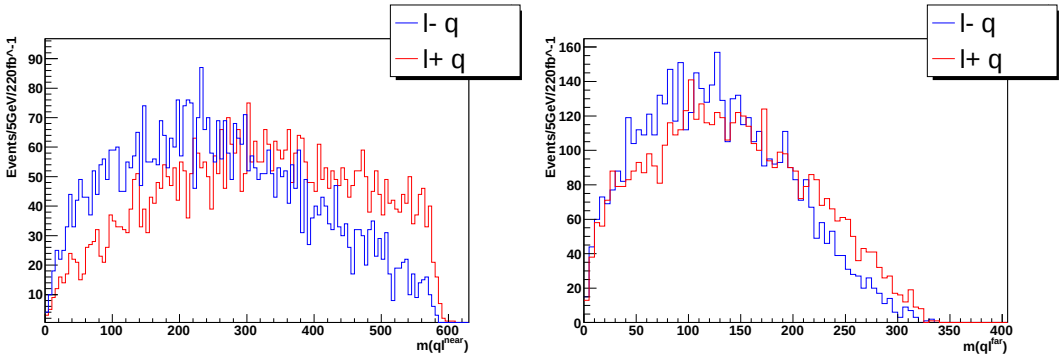

Figure 4.13: Truth level lepton-quark invariant mass distributions for SU1: red line refers to ql^+ system, blue line to ql^-. (left plot) shows the (near lepton, quark) contribution in the right decay chain; (right plot) shows the (far lepton, quark) contribution in the right decay chain.

asymmetry plots defining bin by bin the asymmetry $A = \frac{N^+ - N^-}{N^+ + N^-}$ where $N^\pm$ are the bin entries in the lepton-quark mass distribution for positive and negative leptons respectively. Thus charge asymmetries of $m(ql)$ distributions at MC truth level are shown in figure 4.14 for SU3 and in figures 4.15, 4.16 for all possible combinations in SU1 point.

Such figures show that the shapes of these asymmetries, particularly in the case of near lepton for both left and right decay chain in SU1 (see fig. 4.15 and 4.16 left plot) as well for both

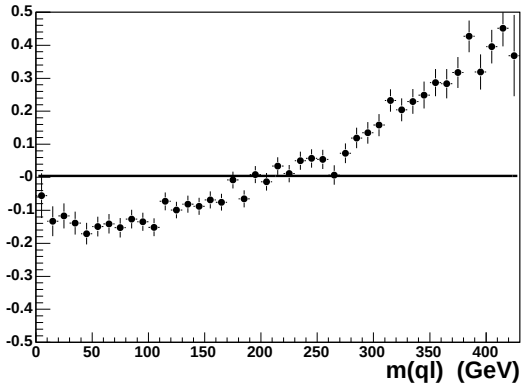

Figure 4.14: $m(ql)$ charge asymmetry at MC truth level in SU3 point for an integrated luminosity of 30 fb^{-1}.

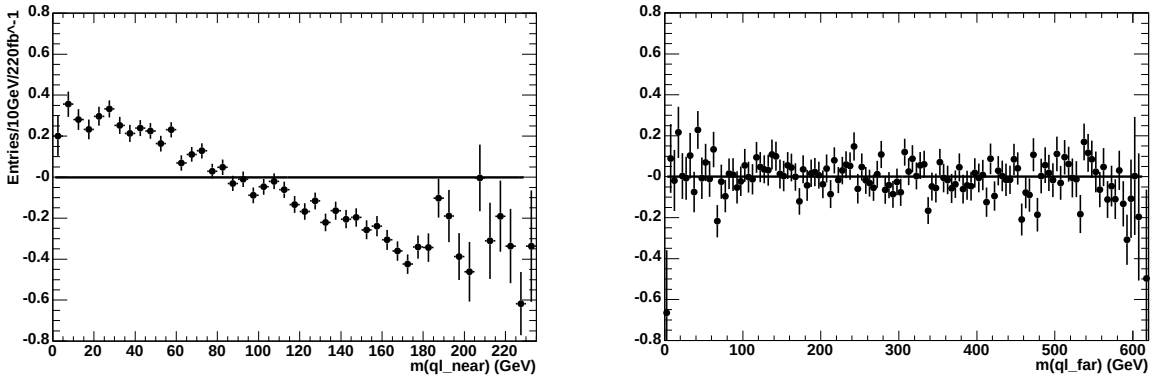

Figure 4.15: $m(ql)$ charge asymmetries at MC truth level in SU1 point for an integrated luminosity of 220 fb^{-1}. Plot on the left (right) corresponds to near (far) lepton plus quark system in the decay chain involving $\tilde{l}_L$.

near and far lepton together in SU3 (see fig. 4.14), are clearly inconsistent with a constant zero value (superimposed line in the plots). This demonstrates that, at parton level, asymmetries are still evident even after the diluting effects due to the presence of $\bar{\tilde{q}}_L$ and, in the SU3 case, also due to the undistinguishability of near/far leptons. Furthermore it is useful to observe that charge asymmetry is detectable with smaller statistics for the SU3 point, since cross sections and branching ratios for decay 4.3 are larger (despite the lower $\tilde{q}/\bar{\tilde{q}}$) ratio and the impossibility to distinguish near/far leptons). Concerning SU1 point, in the analysis described in the following, from now on, will be

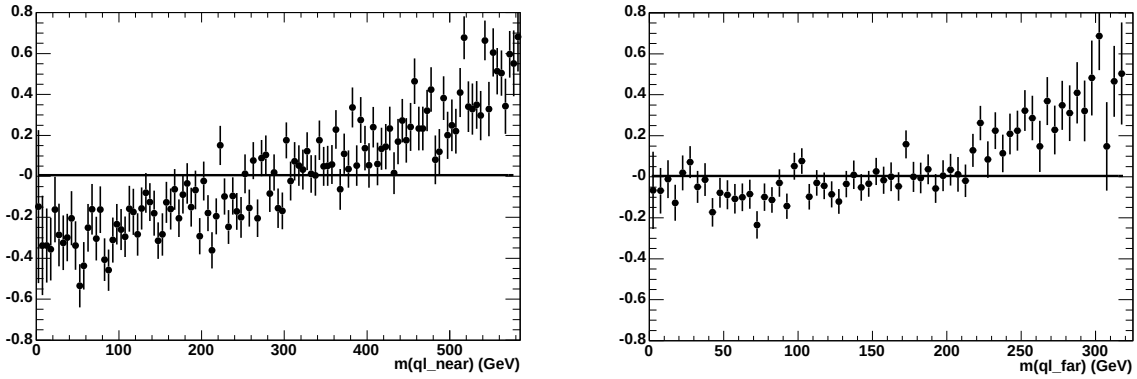

Figure 4.16: $m(ql)$ charge asymmetries at MC truth level in SU1 point for an integrated luminosity of 220 fb^{-1}. Plot on the left (right) corresponds to near (far) lepton plus quark system in the decay chain involving $\tilde{l}_R$.

considered only $m(ql^{near})$ in the $\tilde{l}_L$ decay chain, which represents the case with the most enhanced asymmetry (and with the largest statistics) already at MC truth level.

4.4 Analysis

4.4.1 Background

As already said signal events have a clear experimental topology: namely a large amount of missing transverse energy, high p_T multi-jets and two Same Flavour Opposite Sign (SFOS) leptons. There are both SM and SUSY processes with a very similar final state signature. Background can be classified as:

- irreducible if the two SFOS leptons ($e^{\pm}e^{\mp}$, $\mu^{\pm}\mu^{\mp}$) in the event are correlated;
- reducible if the two SFOS leptons are not correlated.

As an example irreducible background events are represented by the two correlated leptons coming from the decay of Z boson ($Z \rightarrow l^+l^-$). On the other hand, uncorrelated SFOS leptons

originate from two independent decays (or decay chains) in the event. In this case one can assume that the number of events with two uncorrelated SFOS leptons is equal to the number of events with two **O**pposite **F**lavour **O**pposite **S**ign (OFOS) leptons ($e^{\pm}\mu^{\mp}$) and that the invariant mass distributions containing leptons (for instance $m(ll)$, $m(llq)$, $m(lq)$) have the identical shapes for uncorrelated SFOS and OFOS leptons. Consequently reducible background can be reduced by applying SFOS-OFOS subtraction ($e^{\pm}e^{\mp} + \mu^{\pm}\mu^{\mp} - e^{\pm}\mu^{\mp}$) on invariant mass distributions. In general in performing such a subtraction one must take the different detection and reconstruction efficiencies for muons and electrons into account by means of the β factor defined as $\beta = \epsilon(\mu)/\epsilon(e)$ where $\epsilon(\mu, e)$ are the muon and electron efficiencies respectively: the right subtraction operation is $\beta^2 e^{\pm}e^{mp} + \mu^{\pm}\mu^{\mp} - \beta e^{\pm}\mu^{\mp}$. Nevertheless, since in ATLFAST muons and electrons are simulated with the same efficiencies, from now on $\beta = 1$ will be assumed.

SUSY background

As we will see in the following the main component of background is represented by SUSY background both for SU1 and SU3 point. Some example of irreducible background events are:

- Z bosons coming from the decay of heavier gauginos ($\tilde{\chi}_i^0 \rightarrow \tilde{\chi}_j^0 Z$, $i = 3, 4$, $j = 1, 2$ and $\tilde{\chi}_2^{\pm} \rightarrow \tilde{\chi}_1^{\pm} Z$) which further decay to lepton-antilepton pairs;
- $\tilde{\chi}_2^0$ directly produced (not from a left squark) or produced indirectly from stop, sbottom or heavier gaugino decays.

Examples of reducible events, which are eliminable by applying SFOS-OFOS subtraction, are:

- uncorrelated leptons originating from the decay of charginos ($\tilde{\chi}_1^{\pm} \rightarrow \tilde{l}_L \nu_l \rightarrow \nu_l l \tilde{\chi}_1^0$ and $\tilde{\chi}_2^{\pm} \rightarrow \tilde{\nu}_l l$);
- uncorrelated leptons from the decay $\tilde{\chi}_2^0 \rightarrow \tilde{\tau}_1 \tau$.

SM background

The considered SM processes are indicated as $t\bar{t}+$ N jets, $W+$ N jets, $Z+$ N jets [48] where N is the number of additional jets in the event due to the underlying event and pile-up. The decay $t \rightarrow bW^+(\bar{t} \rightarrow \bar{b}W^-)$, with the further leptonic decay of the W boson ($W^{\pm} \rightarrow l^{\pm}\nu_l/\bar{\nu}_l$) represents the main Standard Model background process: the final state is given by jets from

b hadronization, two, eventually, SFOS leptons and large missing transverse energy due to the neutrinos. Other SM processes like $W/Z+$ jets which decay into leptons or $t\bar{t} \rightarrow bWbW \rightarrow bbl\nu qq$ can be also considered as sources of background. The most powerful variable to reject SM events is the missing transverse energy E_T^{miss}: a kinematic hard cut on such a variable, on the number and p_T of jets can significantly remove this background. Finally SM events are further suppressed by applying SFOS-OFOS subtraction which eliminates the uncorrelated component.

4.4.2 Event selection

Preselection cuts

Preselection cuts represent a powerful way (almost model independent) to separate SUSY events from Standard Model background. The following cuts were applied for both SU1 and SU3 events:

- missing transverse energy $E_T^{miss} > 100$ GeV;
- number of jets greater than 3 ($n_{jets} > 3$);
- the transverse momentum of the most energetic jet greater than 100 GeV ($p_T(j1) > 100$ GeV);
- the transverse momenta of three next most energetic jets greater than 50 GeV ($p_T(j2), p_T(j3), p_T(j4) > 50$ GeV).

The E_T^{miss} distributions, normalized to the integrated luminosity of SUSY samples (100 fb^{-1} for SU1, 30 fb^{-1} for SU3), in all SUSY and SM events are shown in figure 4.17 for SU1 and SU3 points where SUSY events have been filtered according to the same standard cuts at the generator level reported in [48] and applied to the SM samples.

It is possible to note that the mean values of distributions for SUSY events, in SU1 and SU3, are much greater (more than double) than those of SM events: this is the reason of why the cut on E_T^{miss} represents the best cut to isolate SUSY from SM events. The superimposed p_T distributions of the four most energetic jets for SUSY and SM events are reported in figure 4.18 for the SU1 point (such distributions are very similar in SU3).

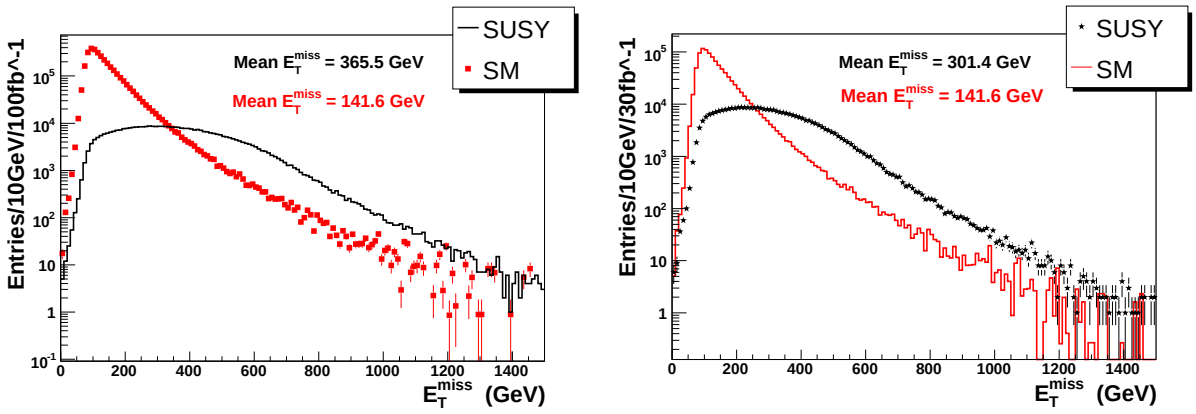

Figure 4.17: Missing transverse energy E_T^{miss} distribution for SUSY events (in black) and SM background (in red) for SU1 (on the left) and SU3 (on the right) points.

Also in this case the mean values of p_T distributions corresponding to SUSY events are, for each of the four considered jets, greater than those of SM events: going from the first jet to the fourth one the difference between mean values becomes smaller and smaller, so most of rejection of SM background is provided by the requirements on the first two most energetic jets. On both SU1 and SU3 points, the preselection cuts previously defined have been found by varying the minimum values required, for E_T^{miss} and $p_T(j_i)$, to provide a reasonable compromise between a high signal selection efficiency and a low SM background contamination.

Additional cuts Preselection cuts allow to reject from selection a lot of SM events; nevertheless it is necessary to apply further cuts to isolate the signal from SUSY background events: these cuts depend on the topology of signal events and on their kinematics (so depend on mSUGRA parameters). First of all we ask for:

- only two SFOS leptons in the event;
- lepton transverse momentum greater than 6 GeV (10 GeV) for SU1 (SU3) point (since in SU1, generally, leptons are less energetic than those in SU3, the cut on p_T of leptons in SU1 is softer than the one in SU3).

These cuts strongly reduce both SUSY and SM background: the number of leptons in the event is required to be exactly two since asking for a higher number provides only a negligible gain in the

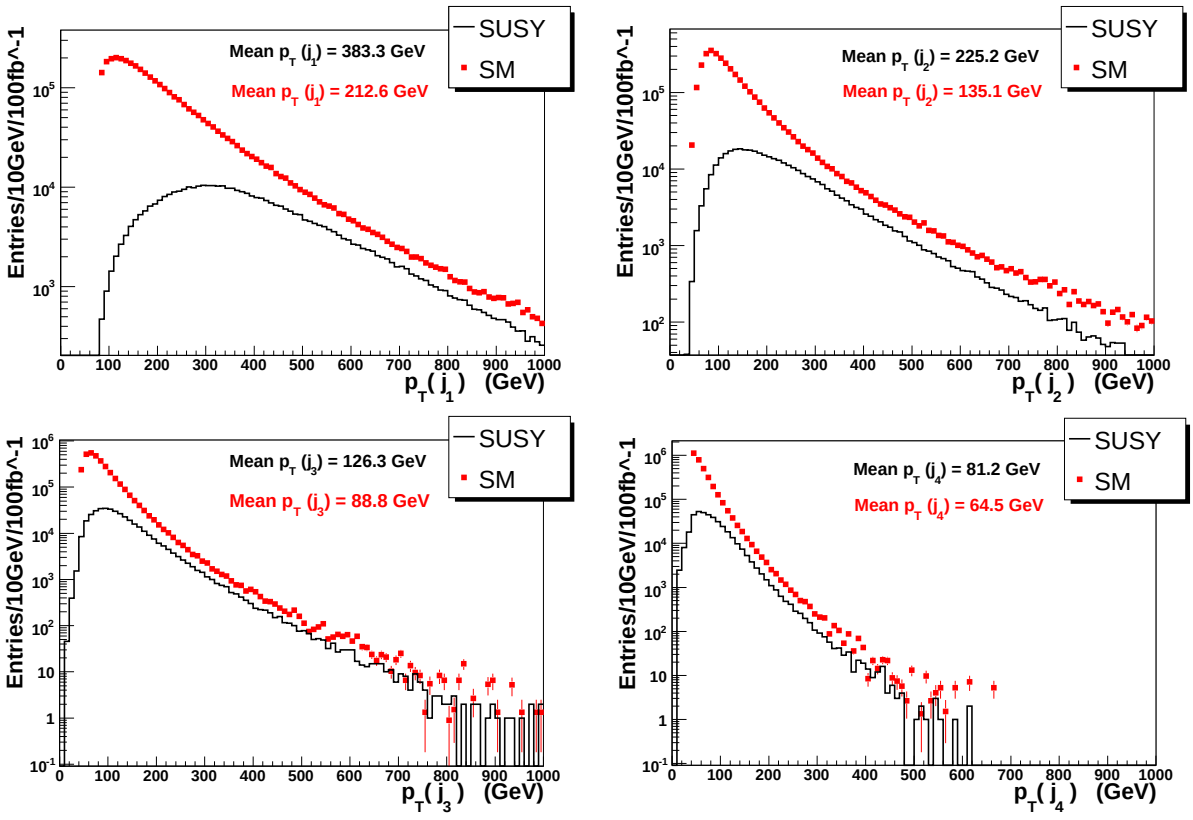

Figure 4.18: Transverse momentum distributions of the four most energetic jets for SU1 events (in black) and SM background (in red).

signal event selection and introduces other technical difficulties due to combinatorics (see in table 4.6).

For example the selection, in SU1 point, of three same flavour leptons, which give two different SFOS pairs, would allow to gain only 0.1% of signal and, moreover, in the selection would pass 0.4% additional SUSY background events. At this point it is possible to form the following invariant masses:

- lepton-lepton invariant mass $m(ll)$,
- lepton-lepton-jet invariant mass $m(llj)$;

where j is one of the two most energetic jets in the event. In fact MC studies showed that in about 80% of signal events one of these two jets originates from left squark decay: namely in

	SU1	Signal	SUSY background
3 leptons (same flavour)	0.5%	0.1%	0.4%
4 leptons (same flavour)	0.04%	0.01%	0.03%
2 SFOS muons + 2 SFOS electrons	0.03%	0.01%	0.02%

	SU3	Signal	SUSY background
3 leptons (same flavour)	0.5%	0.2%	0.3%
4 leptons (same flavour)	0.06%	0.04%	0.02%
2 SFOS muons + 2 SFOS electrons	0.05%	0.03%	0.02%

Table 4.6: Gain in selection, with respect to exactly 2 SFOS leptons, for different cuts on the number of leptons for SU1 and SU3 (after all cuts).

SU1 the most energetic jet is the right jet (that is correctly associated with the quark from left squark decay[4]) in about 50% of cases, while the second most energetic jet is the right one in about 33%. Similarly, in SU3, the first (second) most energetic jets is the right one in about 48% (31%) of signal events. Therefore two lepton-lepton-jet invariant masses are reconstructed on event by event basis: the larger lepton-lepton-jet invariant mass, $m(llj)^{high}$, and the smaller lepton-lepton-jet invariant mass, $m(llj)^{low}$ and the two jets are labelled *high* and *low* accordingly. Again to select the signal from SUSY and SM background the following kinematic cuts have been applied:

- $m(ll) < 100$ GeV, $m(llj) < 615$ GeV for the SU1 point;
- $m(ll) < 100$ GeV, $m(llj) < 500$ GeV for the SU3 point;

where the values of cuts are the kinematic endpoints in invariant distributions and j is the *low* jet (the one giving the smaller lepton-lepton-jet invariant mass). Efficiencies of all cuts described so far and the signal/background ratios after all cuts are reported in table 4.7 for SUSY and SM samples. From this table one can see that the main component of background is represented, in both SU1 and SU3 point, by SUSY itself, while the largest Standard Model background is given by $t\bar{t}+2$ or more jets (particularly when the final state contains 2 charged leptons and 2 neutrinos):

[4]The right jet is chosen by evaluating the angular variable $\Delta R = \sqrt{(\Delta\phi)^2 + (\Delta\eta)^2}$ between any jet and the signal quark, and by taking the jet which minimizes such a quantity

	Efficiency (SU1)	S/B (SU1)	Efficiency (SU3)	S/B (SU3)
Signal	(17.0 ± 0.3) %	/	(20.0 ± 0.3)%	/
SUSY Background	(0.94 ± 0.01)%	0.33	(0.75 ± 0.01)%	1
$t\bar{t}$ + 0 jets $(l\nu qq)$	$(1.3 \pm 0.3)\ 10^{-6}$	$\sim$80	$(4 \pm 1)\ 10^{-7}$	$\sim$1500
$t\bar{t}$ + 1 jets $(l\nu qq)$	$(2.9 \pm 0.2)\ 10^{-5}$	6.3	$(1.2 \pm 0.1)\ 10^{-5}$	90
$t\bar{t}$ + 2 jets $(l\nu qq)$	$(1.3 \pm 0.1)\ 10^{-4}$	3.5	$(5.9 \pm 0.4)\ 10^{-5}$	45
$t\bar{t}$ + ≥ 3 jets $(l\nu qq)$	$(5.3 \pm 0.2)\ 10^{-4}$	2.6	$(2.3 \pm 0.1)\ 10^{-4}$	37
$t\bar{t}$ + 0 jets $(l\nu l\nu)$	$(1.9 \pm 0.4)\ 10^{-6}$	$\sim$200	$(3.0 \pm 0.5)\ 10^{-6}$	$\sim$1000
$t\bar{t}$ + 1 jets $(l\nu l\nu)$	$(1.5 \pm 0.1)\ 10^{-4}$	4.8	$(2.2 \pm 0.1)\ 10^{-4}$	20
$t\bar{t}$ + 2 jets $(l\nu l\nu)$	$(2.93 \pm 0.04)\ 10^{-3}$	0.64	$(3.89 \pm 0.05)\ 10^{-3}$	2.9
$t\bar{t}$ + $\geq$ 3 jets $(l\nu l\nu)$	(1.65 ± 0.02) %	0.34	(2.10 ± 0.02) %	1.6
W + 4 jets $(l\nu l\nu)$	$(1 \pm 1)\ 10^{-5}$	24	$(2 \pm 2)\ 10^{-6}$	$\sim$1000
W + $\geq$ 5 jets $(l\nu l\nu)$	$(2 \pm 2)\ 10^{-5}$	50	$(1 \pm 1)\ 10^{-5}$	$\sim$500
Z + 3 jets	$(3.1 \pm 0.4)\ 10^{-5}$	$\sim$500	$(3.1 \pm 0.4)\ 10^{-5}$	$\sim$2000
Z + 4 jets	$(2.0 \pm 0.1)\ 10^{-3}$	27	$(1.7 \pm 0.1)\ 10^{-3}$	$\sim$200
Z + $\geq$ 5 jets	$(7.0 \pm 0.2)\ 10^{-3}$	24	$(5.6 \pm 0.2)\ 10^{-3}$	$\sim$200

Table 4.7: Efficiencies and S/B ratios for SUSY signal and background (SU1, SU3) and for the most relevant sources from SM background. No OFOS subtraction is applied.

this is true especially for SU1 point which has a smaller production cross section. Some channels ($t\bar{t}(allhadronic)$, $W + 1,\ 2,\ 3$ jets and $Z + 1,\ 2$ jets) are not reported in table 4.7 since their contribution is negligible (according to fast simulation results). At this stage events with two OFOS leptons are also selected and used to remove SUSY and SM combinatorial background by performing the SFOS-OFOS subtraction on all mass distributions containing leptons: after this operation the contribution of SUSY background to the finally selected sample is furtherly reduced and SM processes with two uncorrelated leptons become compatible with zero within errors. It is possible to see an example of the SFOS-OFOS subtraction referring to dilepton invarian mass $m(ll)$ for SU3 point.

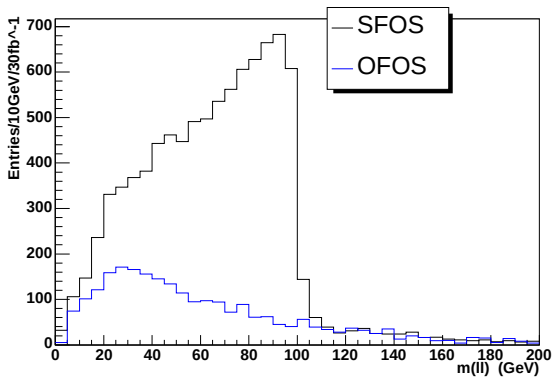

Figure 4.19: Reconstructed dilepton invariant mass of all event with two SFOS leptons (in black) passing all described cuts superimposed to the distribution relative to events with two OFOS leptons passing the same cuts (in blue) for the SU3 point.

Plot 4.19 shows the reconstructed $m(ll)$ invariant mass (in black) obtained by selecting all events with two SFOS leptons passing our selection, superimposed with the reconstructed $m(ll)$ (in blue) obtained, this time, by selecting events with two OFOS leptons passing the same cuts. It is evident that the reconstructed SFOS distribution does not represent exactly the dilepton invariant mass distribution in fig. 4.9 (right plot): it has a little excess of entries at small mass values (around 25 GeV) that is due to the OFOS component. In fact by performing SFOS-OFOS subtraction we obtain the plot in fig. 4.20 where the right triangular shape (black points) is now restored (even if the irreducible SUSY background is still present) and where the SM background (in red) is strongly suppressed and compatible with zero except a little SM component close to 90 GeV due to the

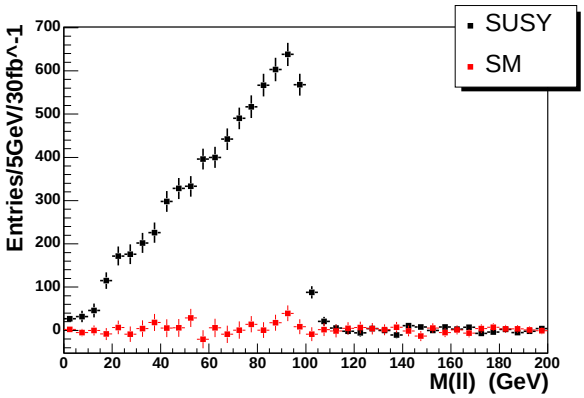

Figure 4.20: Reconstructed dilepton invariant mass of events passing all selection (after SFOS-OFOS subtraction) for SU3 events (in black) and SM background (in red).

irreducible contribution of $Z+$ jets sample. The reconstructed dilepton invariant mass in SU1 is shown in figure 4.21: both for SU1 and SU3 reconstructed endpoints are at the expected positions and shapes of the distributions are not significantly modified by SUSY and SM background, in particular for SU3 characterized by larger cross section and branching ratios for the decay under consideration. As already said before the two highest transverse momentum jets are correctly

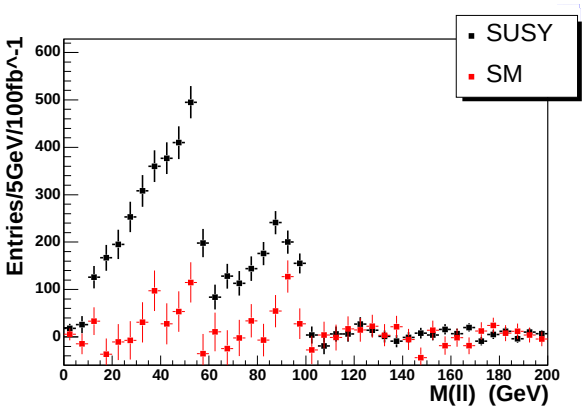

Figure 4.21: Reconstructed dilepton invariant mass of events passing all selection (after SFOS-OFOS subtraction) for SU1 events (in black) and SM background (in red).

associted with the quark from left squark decay in about 80% of cases, so, in order to reconstruct lepton-lepton-jet invariant mass larger and smaller, $m(llj)^{high}$ and $m(llj)^{low}$, mass distributions

are added together to obtain the $m(llj)$ presented in figure 4.22 for the SUSY events (black points) and SM background (red points) superimposed.

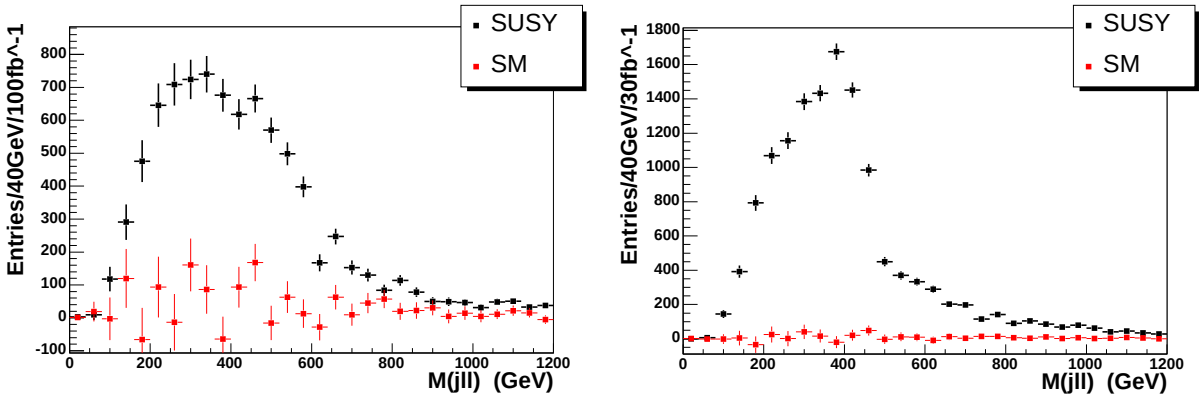

Figure 4.22: Reconstructed lepton-lepton-jet invariant mass of events passing all selection (after SFOS-OFOS subtraction): (left plot) for SU1 events (in black) and SM background (in red); (right plot) for SU3 events (in black) and SM background (in red).

4.4.3 Results on charge asymmetries

In order to obtain charge asymmetry plots it is necessary to form lepton-jet, antilepton-jet invariant mass distributions, $m(jl^{\pm}$. These latter are formed, similarly to lepton-lepton-jet mass distributions, by evaluating $m(jl^{\pm})^{low}$ and $m(jl^{\pm})^{high}$ (obtained by considering the *low* and *high* jet respectively, see section 4.4.2), which have then been added together to get $m(jl)$ distribution. In this way we can select the right jet in 80% of cases and, as it will be shown with more detail in the following, the choice of considering at least one wrong jet (i.e. not associated to the quark in the decay chain of interest) per event has the only effect to dilute charge asymmetry. For what concerns SU1 the particular kinematic properties of this point, as already observed in section 4.3.3, allow to distinguish near and far leptons in the two possible decay chains,involving respectively left and right sleptons. At this purpose the particular decay chain is selected by setting the following cuts:

- $m(ll) < 57$ GeV for the left slepton;
- 57 GeV $< m(ll) < 100$ GeV for the right slepton.

on dilepton invariant mass while near and far leptons are selected, as shown in section 4.3.2, according to their transverse momenta: in left decay chain case the near (far) lepton is the one with lower (higher) transverse momentum, and vice versa in the case of right decay chain. Therefore for this mSUGRA point it is possible to form four different lepton-jet invariant masses: $m(jl^{near})_L$, $m(jl^{far})_L$, $m(jl^{near})_R$ and $m(jl^{far})_R$. From figures 4.15 and 4.16 it is evident that, already at truth level, (near lepton - jet) systems generate most enhanced asymmetries; on the other hand, since right slepton selection does not allow to reject correlated leptons (forming a dilepton mass close to 90 GeV) coming from Z bosons and since branching ratio for the whole right decay chain is smaller (half) than the left one, we chose to reconstruct only $m(jl^{near})_L$ mass distributions even if its selection is affected by a contamination (15%) due to events with right slepton in which $m(ll) < 57$ GeV. In SU3 there is no way to distinguish leptons so lepton-jet invariant masses are formed with both of them. Reconstructed $m(jl^{\pm})$ mass distributions, for both SU1 (using the near lepton from the chain involving $\tilde{l}_L$) and SU3 (using both SFOS leptons per event) points, are reported in figures 4.23 after SFOS-OFOS subtraction.

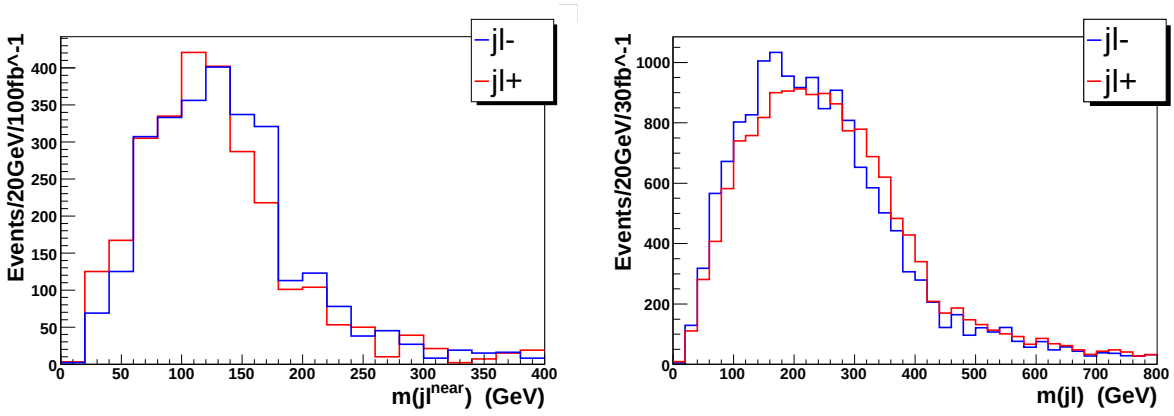

Figure 4.23: Reconstructed lepton-jet invariant mass of events passing all selection (after SFOS-OFOS subtraction): (left plot) using the near lepton from the chain involving $\tilde{l}_L$ in SU1 point. (right plot) using both near and far leptons in SU3 point.

Charge asymmetries

Starting from $m(jl)$ distributions shown above (after SFOS-OFOS subtraction) (figures 4.23) it has been possible to evaluate charge asymmetries bin by bin, with a bin width opportunely chosen.

Also the dependence of results on the choice of the binning has been checked and found to be negligible. The ranges, over which statistical tests (which I'm going to describe) have been applyed on $m(lj)$ charge asymmetries, are the following:

- $[0 - 220]$ GeV for SU1 (only for decay with left slepton and near lepton);
- $[0 - 410]$ GeV for SU3.

Such ranges are slightly larger than the expected kinematic endpoints of lepton-jet invariant mass (see table 4.5) to take into account for smearing effects on $m(jl)$ reconstruction due to resolution effects, jet misidentification, etc. The purpose of this work, as already said, is to verify that the neutralino has a non-zero spin: this means that it is not important the shape of the charge asymmetry plot but it is sufficient to demonstrate that it has not a flat behavior. Consequently, two different methods have been applied to check and estimate the presence of a non-zero charge asymmetry:

1. a comparison between asymmetry plot and constant function $y = 0$ (zero-asymmetry hypothesis) by means of a non parametric χ^2 test which provides a confidence level CL_{χ^2};
2. a *Run Test* method [51] for which, only a small number of runs (a run is defined here as a set of consecutive points of the same sign, i.e. positive or negative, in the asymmetry plot. Therefore the number of runs is the number of such sets.) have to occur with respect to the number of bins[5]. Also in this case it is possible to get a confidence level[6], CL_{RT}, for the hypothesis of no asymmetry, related to the number of runs and bins.

[5]Practically, in case of symmetry, a large number of runs is expected due to the statistical fluctuations of points around $y = 0$. Vice versa in case of asymmetry.

[6]If one has to verify the null-hypothesis then it is expected a large number of runs relatively to n (number of negative points) and p (number of positive points). Probability to have a number of runs equal to *r* is defined as it follows:

Methods (1) and (2) are independent and their probabilities can be combined (see fot instance [51]) providing a final confidence level[7] CL_{comb} which does not depend on shape of the eventual charge asymmetry. Charge asymmetries for $m(jl^{near})_L$ is SU1 point and for $m(jl)$ (with both leptons) in SU3 are reported in figure 4.24: confidence levels obtained with the two methods separately, CL_{χ^2} and CL_{RT}, and combined together, CL_{comb}, are shown for each asymmetry plot (the horizontal line at 0 is drawn as a reference and it represents the null hypothesis).

It is evident that the value of CL_{comb}, for SU1 point with 100 fb^{-1}, is well below 1% while just 30 fb^{-1} are sufficient to get a very low ($< 10^{-9}$) confidence level in the case of SU3 point. As expected charge asymmetry in the decay chain under study with left slepton (SU1 point) behaves in opposite way to the case in which the right slepton is involved (SU3): the former one goes from positive values to negative ones; vice versa holds for the latter case. As already discussed, the SFOS-OFOS subtraction procedure has the advantage of statistically removing the contribution of the reducible SFOS background: in order to demonstrate that such a operation does not affect the

$$P(r=2k) = 2\frac{\begin{pmatrix} n-1 & p-1 \\ k-1 & k-1 \end{pmatrix}}{\begin{pmatrix} n+p \\ n \end{pmatrix}}; \tag{4.8}$$

$$P(r=2k-1) = 2\frac{\begin{pmatrix} n-1 \\ k-2 \end{pmatrix}\begin{pmatrix} p-1 \\ k-1 \end{pmatrix} + \begin{pmatrix} n-1 \\ k-1 \end{pmatrix}\begin{pmatrix} p-1 \\ k-2 \end{pmatrix}}{\begin{pmatrix} n+p \\ n \end{pmatrix}}.$$

depending on whether *r* is even ($r = 2k$) or odd ($r = 2k-1$). Such distributions have a mean value and variance:

$$E(r) = \frac{2np}{n+p} + 1\,; \quad V(r) = \frac{2np(2np-n-p)}{(n+p)^2(n+p-1)}. \tag{4.9}$$

If n,m are large (> 10), the probability distributions can be approximated by standard normal distributions: in order to get the confidence level we choose the following estimator variable:

$$s = \frac{r - E(r)}{\sqrt{V(r)}}.$$

The confidence level is, in this way, defined by $CL(s) = 1 - \int_s^\infty f(y)dy$, where $f(y)$ is the normal distribution.

[7] If number of measurements are sufficiently large the two probability distributions can be approximated by a continuous function uniformely distribuited over $[0,1]$. The combined function $u = -2(\ln P_1 + \ln P_2)$ corresponds to a $\chi^2(4)$ distribution (4 is the number of degree of freedom) from which it is possible to get a new confidence level

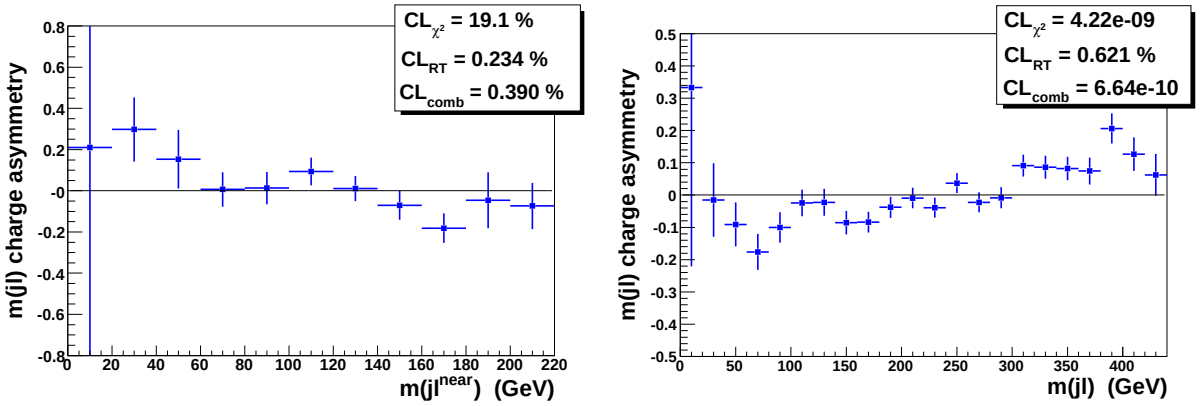

Figure 4.24: Charge asymmetries for lepton-jet invariant masses after SFOS-OFOS subtraction. Left: using the near lepton from the chain involving $\tilde{l}_L$ in SU1 point. Right: using both near and far leptons in SU3 point.

observability of the charge asymmetry, the same statistical tests have been applied on asymmetry plot obtained by $m(jl)$ distributions of all OFOS events passing the selection steps.

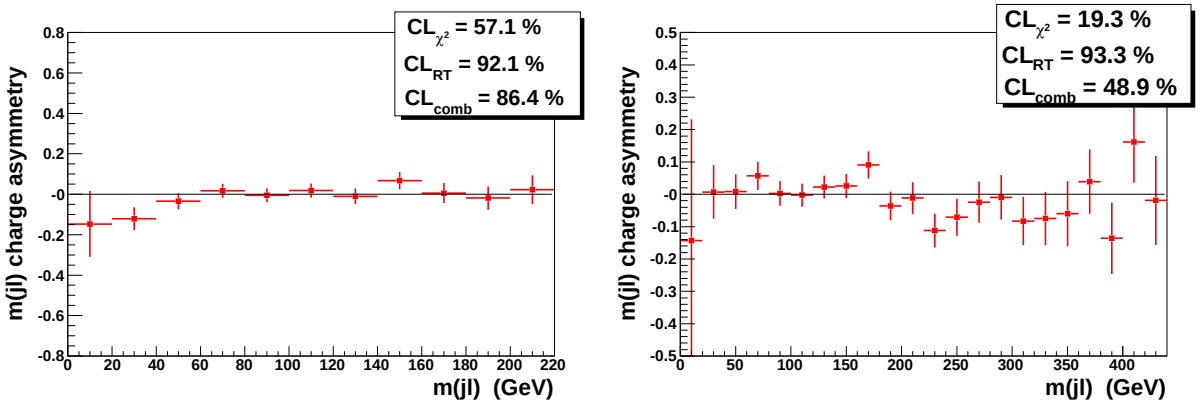

Figure 4.25: Charge asymmetries for $m(jl)$ obtained in SUSY events with OFOS leptons pairs. Left: using the near lepton from the chain involving $\tilde{l}_L$ in SU1 point. Right: using both near and far leptons in SU3 point.

Plots and results are shown in figure 4.25 for SU1 and SU3 points: the combined confidence level measured in SU3 is larger than 50% and even better in SU1 case, giving, in this way, a quantitative evidence for the flatness of the plots. The OFOS subtraction does not allow to eliminate all SUSY

background events, whose contribution is not negligible after selection (see table 4.7), especially for SU1 point: nevertheless they do not introduce relevant biases in the charge asymmetry as it is possible to observe in figure 4.26, which shows charge asymmetry plots, in SU1 and SU3 point, for SFOS background events only.

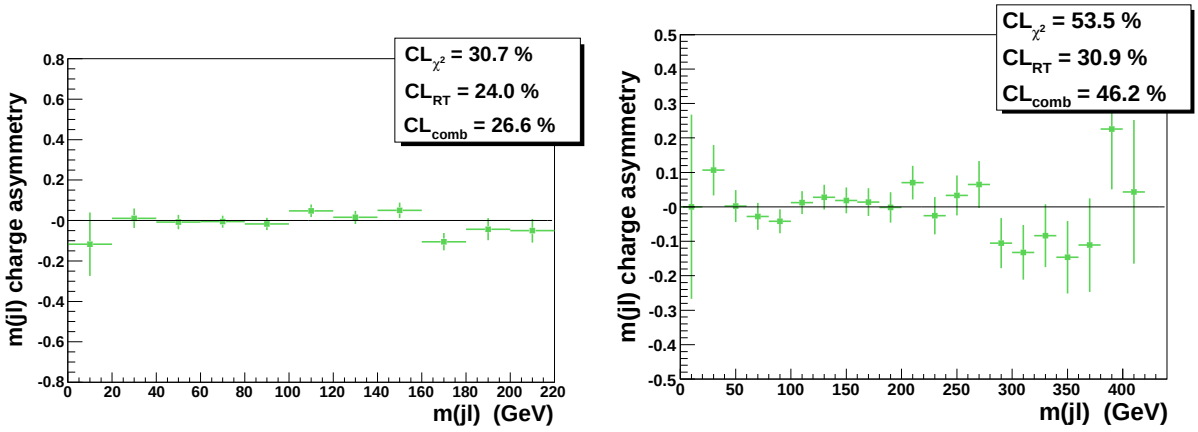

Figure 4.26: Charge asymmetries for $m(jl)$ distributions obtained considering only the selected SUSY background events. Left: using the near lepton from the chain involving $\tilde{l}_L$ in SU1 point. Right: using both near and far leptons in SU3 point.

The obtained CL_{comb} is, in both cases, high compared to the whole selected final sample including signal. Again, a similar check it has been performed, on both SFOS and OFOS charge asymmetries, formed by using Standard Model events passing cuts only: this is done, depending on point, over different $m(jl)$ ranges ($[0-220]$ GeV for SU1; $[0-420]$ GeV for SU3).

Figure 4.27 shows that a combined confidence level CL_{comb} of more than $60-70\%$ is obtained in this case, except in the most critical condition represented by the $m(jl^{near})_L$ charge asymmetry in SFOS events of SU1 point (here $CL_{comb} = 20\%$). This is to be attributed to relatively small number of bins over which the charge asymmetry is tested; anyway, after cuts and SFOS-OFOS subtraction, very few SM events remain in $m(jl)$ distributions so that their eventual effect on charge asymmetry is negligible. In order to prove that the selection of at least one wrong jet per event does not affect significantly charge asymmetry results it has also been performed the statistical tests by selecting only lepton-jet invariant masses formed with the wrong jet (selected on basis of MC truth).

Results are reported in figure 4.28 for SU1 and SU3: the most affected point is SU3 with a $CL_{comb} = 14\%$ for the hypothesis of zero-asymmetry: on the other hand, actually, this confi-

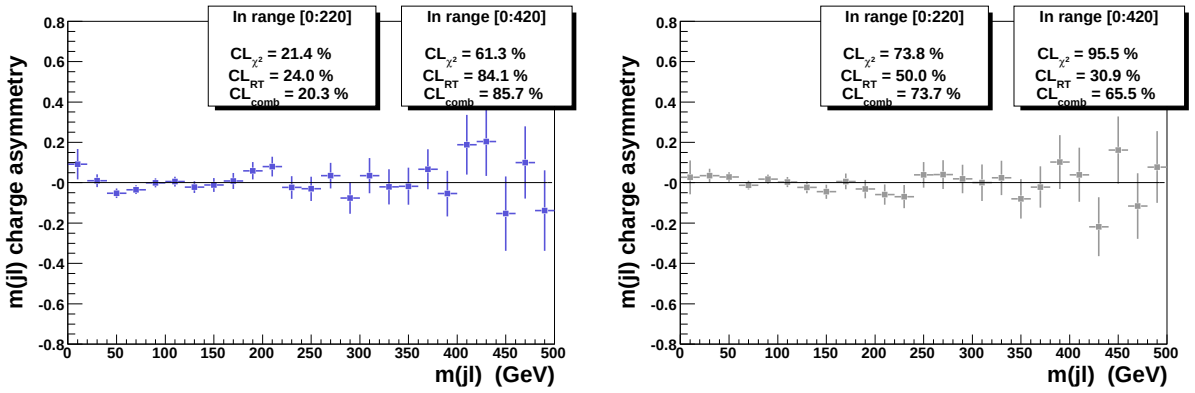

Figure 4.27: Charge asymmetries for $m(jl)$ distributions of SM background events, for SFOS leptons (on the left) and for OFOS leptons (on the right).

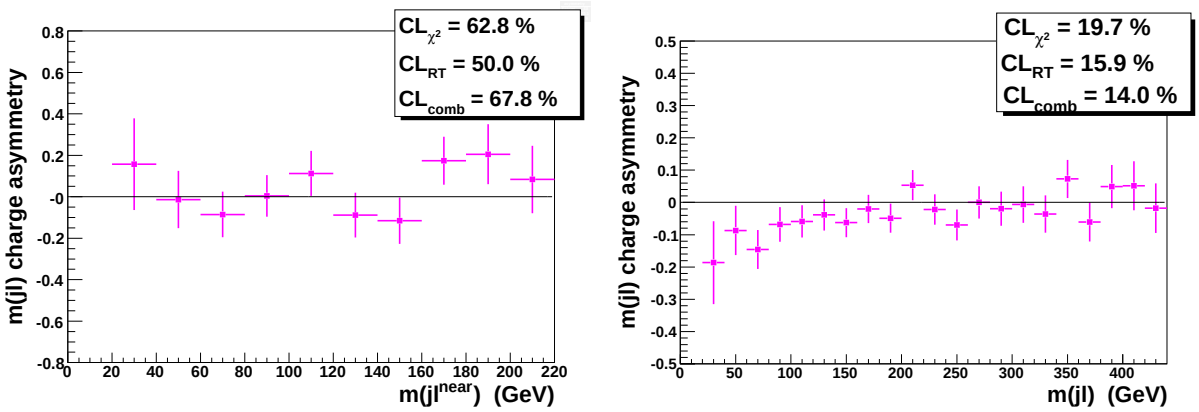

Figure 4.28: Charge asymmetries for $m(jl)$ distributions obtained when a wrong jet is selected, according to MC truth. Left: using the near lepton from the chain involving $\tilde{l}_L$ in SU1 point. Right: using both near and far leptons in SU3 point.

dence level is many orders of magnitude larger than the one obtained in figure 4.24 (right plot) so that we can consider negligible such an effect on final charge asymmetry plot. Table 4.8 reports the confidence levels, as obtained with the two statistical method separately and combined, relative to all of statistical tests performed.

Finally, the whole analysis has been repeated, for SU1 and SU3 points, at different values of integrated luminosity: figure 4.29 illustrtes the confidence levels, CL_{χ^2}, CL_{RT} and CL_{comb}, as a

	SU1			SU3		
	$CL_{\chi_2^0}$	CL_{run}	CL_{comb}	$CL_{\chi_2^0}$	CL_{run}	CL_{comb}
SFOS-OFOS (SUSY sample)	19%	0.243%	**0.390%**	4.2*10^{-7}%	0.621%	**6.64*10^{-8}%**
OFOS (SUSY background)	57.1%	92.1%	86.4%	19.3%	93.3%	48.9%
SFOS (SUSY background)	30.7%	24.0%	26.6%	53.5%	30.9%	46.2%
SFOS (SM)	21.4%	24%	20.3%	81.3%	84.1%	85.7%
OFOS (SM)	73.8%	50.0%	73.7%	96.6%	30.9%	65.5%
SFOS (wrong jet)	62.8%	50.0%	67.8%	19.7%	15.9%	14%

Table 4.8: Confidence levels for all statistical test performed.

function of the integrated luminosity with which the analysis was done.

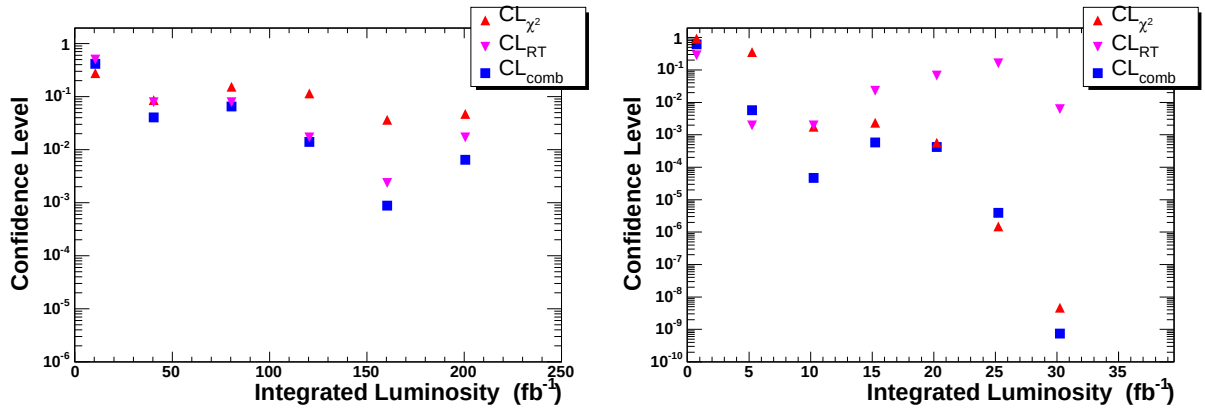

Figure 4.29: Confidence levels for having no charge asymmetry in $m(jl)$ distributions as functions of integrated luminosity. Left: using the near lepton from the chain involving $\tilde{l}_L$ in SU1 point. Right: using both near and far leptons in SU3 point.

It is evident that, in the case of SU1, to achieve a confidence level (CL_{comb}), for the zero-asymmetry hypothesis, below 1%, it is necessary to collect a statistics corresponding to at least 100 fb-1 while scarcely 10 fb-1 (ten times less) are needed to performe the measure in SU3 with an even higher

probability. It should be reminded that, at the initial luminosity (10^{33} cm-2s^{-1}), LHC can collect around 10 fb^{-1} per year while up to 100 fb^{-1} per year at the project luminosity (10^{34} cm^{-2}s^{-1}): thus, once new physics is discovered, whether this measurement it will be possible in the first few days strongly depends on the model as proved by the study of two different points in mSUGRA parameter space, like SU1 and SU3.

Conclusions

Supersymmetry research is one of the main items of the wide physics program of the four experiments working at the new high energy collider, Large Hadron Collider (LHC) at CERN. If Supersymmetry (SUSY) exists LHC will allow to discover it, at least up to an energy scale of the order of ~ 1 TeV. In particular in the ATLAS experiment, two search strategies for supersymmetric particles have been studied: namely inclusive and exclusive searches. Inclusive analyses consist in searching for generic SUSY signals such as missing transverse energy plus high transverse momentum multi-jets plus, eventually leptons. In this way it will be possible to show any deviations with respect to what expected from Standard Model predictions and, at the same time, to measure the SUSY mass scale. After this phase, if new physics emerge, it will be necessary to characterize it with measurements of branching ratios, masses, spins, etc. This is the subject of exclusive analyses which consist in reconstructing particular decay chains from which it is possible to extract useful information. In this context is set the work described in this thesis: it represents a feasibility study (all events have been generated and then simulated with the fast simulation software called ATLFAST) of second lightest neutralino spin measurements for two different benchmark points (selected by ATLAS collaboration) in the minimal Supergravity model (mSUGRA) parameter space: namely a "typical" point in bulk region (SU3) and, as a more complicated case, a point in stau-coannihilation region (SU1). In particular, the decay chain $\tilde{q}_L \rightarrow \tilde{\chi}_2^0 q \rightarrow \tilde{l}_{L,R}^{\pm} l^{\mp} q \rightarrow l^+ l^- q \ \tilde{\chi}_1^0$ has been studied in order to verify the consistency of the spin-$1/2$ neutralino hypothesis, by looking for charge (charge of lepton) asymmetry in lepton-jet invariant mass distributions. By means of a set of optimized cuts, the decay chain under study was isolated and both SUSY and Standard Model background events were successfully reduced. In order to estimate the charge asymmetry in invariant mass distributions, two independent statistical method were used: the residual background were proved to have no asymmetry: the only effect is a slight dilution of the asymmetry of signal. The spin measurement has been possible for both mSUGRA points even if with more diffi-

culties in SU1 case due to its kinematic properties. Results show that an integrated luminosity of at least 100 fb^{-1} is needed in the case of the SU1 point to observe a non-zero charge asymmetry with a confidence level of about 99%, while in the more favorable case of the SU3 point just 10 fb^{-1} would be sufficient. Next step will be to perform the same studies by using the full reconstruction of events in the ATLAS detector which, unlike fast simulation (ATLFAST), takes into account all reconstruction efficiencies and detector resolutions for each point of the whole ATLAS detector (requiring for this reason a much larger processing time with respect to ATLFAST).

Bibliography

[1] P.Higgs, *Phys. Lett.* **12** (1964) 132-133; *Phys. Rev. Lett.* **13** (1964) 508; *Phys. Rev. Lett.* **145** (1966) 1264.

[2] S.P. Martin, *A supersymmetry Primer* **hep-ph/9709356**

[3] S. Dawson, *SUSY and Such* **hep-ph/9612229**

[4] *A Combination of Preliminary Electroweak Measurements and Constraints on the Standard Model* **CERN-EP/2001-098**

[5] ATLAS Collaboration, *ATLAS: Detector and Physics Performance Technical Design Report*, CERN/LHC/99-14, ATLAS TDR 14 (1999).

[6] ATLAS Collaboration, *ATLAS: Detector and Physics Performance Technical Design Report*, CERN/LHC/99-15, ATLAS TDR 15 (1999).

[7] I.J.R. Aitchinson, Lectures at 2001 CERN Summer School, Beatemberg. CERN-2002-002;
I.J.R. Aitchinson and A.J.G. Hey,*Gauge Theories in Particle Physics*, second edition, Institute of Physics (1999);
F. Halzen, D.A. Martin, *Quark and leptons*, J. Wiley & Sons.

[8] J. Baines et al., *B Decays at the LHC*, CERN-TH/2000-101.

[9] *The Large Hadron Collider Accelerator Project*, LHC CERN-AC-93-03.

[10] *The Large Hadron Collider Conceptual Design*, LHC CERN-AC-95-05.

[11] ATLAS Collaboration, ATLAS Technical Proposal, CERN/LHCC/94-93 (1994).

[12] CMS Collaboration, CMS Technical Proposal, CERN/LHCC/94-38 (1994).

[13] LHCb Collaboration, LHCb TeCHNICAL PROPOSAL, CERN/LHCC/94-4 (1998).

[14] ALICE Collaboration, ALICE Technical Proposal, CERN/LHCC/95-71 (1995).

[15] ATLAS Collaboration, *ATLAS Inner Detector Technical Design Report Vol. 1*, CERN/LHC/97-16, ATLAS TDR 4 (1997).

[16] ATLAS Collaboration, *ATLAS Inner Detector Technical Design Report, Vol. 2*, CERN/LHC/97-17, ATLAS TDR 5 (1997).

[17] ATLAS Collaboration, *ATLAS Pixel Detector Technical Design Report*, CERN/LHC/98-13, ATLAS TDR 4 (1998).

[18] ATLAS Collaboration, *ATLAS Magnet System Technical Design Report*, CERN/LHCC/97-18, ATLAS TDR 6, (1997).

[19] ATLAS Collaboration, *ATLAS Liquid Argon Calorimeter Technical Design Report*, CERN/LHC/96-41, ATLAS TDR 2 (1998).

[20] ATLAS Collaboration, *ATLAS Tile Calorimeter Technical Design Report*, CERN/LHCC/96-42, ATLAS TDR 3, (1996).

[21] ATLAS Collaboration, *ATLAS Muon Spectrometer Technical Design Report*, CERN/LHCC/97-22, ATLAS TDR 10, (1997).

[22] Michela Biglietti, *Muon Object Oriented Reconstruction fot the ATLAS Experiment at LHC.*, PhD Thesis XVI Ciclo, Universitá degli studi di Napoli “Federico II”.

[23] G.Viehhauser, *Detector Physics of ATLAS precision muon chamber*, PhD thesis, CERN.

[24] E. Gschwendtner et al., *Analysis of the X-tomograph scan data for MDT chamber prototypes*, ATLAS-MUON-NO-97-175, CERN (1997).

[25] C. Bacci et al., *Autocalibration of High Precision Drift Tubes*, Nucl. Phys. Proc. Suppl 54 (1997) 311.

[26] H. Groenstege, *The RASNIK/CCD 3D Alignment system*, ATLAS Note MUON-NO-155 (1997).

[27] V. Polichronakos, *A Proposal to Use Chatode Strip Chambers (CSC) for the ATLAS Forward Muon System*, ATLAS-MUON-94-038.

[28] A. Gordeev et al., *CSC Performance at High Background Rates*, ATL-MUON-2000-005.

[29] E. Duchovni et al., *Possible Utilization of Thin-Gap Chambers in the ATLAS Muon System*, ATL-MUON-93-023.

[30] ATLAS Collaboration, *ATLAS First Level Trigger Technical Design Report*, CERN/LHCC/98-14, (1998).

[31] ATLAS Collaboration, *ATLAS High-level Triggers, DAQ and DCS Technical Proposal*, CERN/LHCC/2000-17 (2000).

[32] M.S. Alam et al., [CLEO Collaboration], *Phys. Rev. Lett.***74** (1995) 2885 as updated in S. Ahmed et al., CLEO CONF 99-10; BELLE Collaboration, BELLE-CONF-0003, contribution to the 30th International conference on High-Energy Physics, Osaka, 2000. See also K. Abe et al., [Belle Collaboration], [arXiv:hep-ex/0107065]; L.Lista [BaBar Collaboration], [arXiv:hep-ex/0110010]; C. Degrassi, P.Gambino and G.F. Giudice, JHEP **0012** (2000) 009 [arXiv:hep-ph/0009337]; M. Carena, D. Garcia, U. Nierste and C.E. Wagner, *Phys. Lett. B* **499** (2001) 141 [arXiv:hep-ph/0010003].

[33] S. Baek, P. Ko and J. H. Park *Muon anomalous magnetic moment from effective supersymmetry* Eur. Phys. J. C24, 613-618 **hep-ph/0203251**; David W. Hertzog, *The BNL muon anomalous magnetic moment measurement*, (2002) **hep-ex/0202024**.

[34] C.L. Bennett et al., arXiv:astro-ph/0302207;D.N. Spergel et al., arXiv:astro-ph/0302209.

[35] H. Baer et al., *Linear Collider Capabilities for Supersymmetry in Dark Matter Allowed Regions of the mSUGRA Model*, **hep-ph/0311351**

[36] F. Gianotti, *Searches for supersymmetry at high-energy colliders: the past, the present and the future.*, New Journal of Physics **4** (2002) 63.1-63.25.

[37] ALEPH Collaboration, *Searches for Supersymmetric Particles in e^+e^- Collisions at $\sqrt{s}$ up to 202 GeV and Mass Limit for the Lightest Neutralino*, [hep-ph/0011047] v1 (2000).

[38] D.R. Tovey, *Measuring the SUSY Mass Scale at the LHC*, **ATL-PHYS-2002-013**

[39] C.G. Lester, *Model independent sparticle mass measurements at ATLAS (Phd thesis)*, **CERN-THESIS-2004-003**

[40] B.C. Allanach et al., *Measuring sparticle masses in non-universal string inspired models at the LHC*, **arXiv:hep-ph/0007009**

[41] E. Lykten, *Prospects for Slepton Searches with ATLAS (Phd thesis)*, **Phd thesis**

[42] A.J. Barr, *Determinating the spin of supersymmetric particles at the LHC using lepton charge asymmetry*, Phys.Lett. **B596** (2004) 205-212, [hep-ph/0405052].

[43] G. Corcella et al., *JHEP* **0101** (2001) 010, [hep-ph/0011363].

[44] S. Moretti et al., *JHEP* **0204** (2002) 028, [hep-ph/0204123].

[45] G. Corcella et al., [hep-ph/0210213].

[46] Program and its documentation are available from www.hep.phy.cam.ac.uk/richardn/HERWIG/ISAWIG

[47] H. Baer et al., [hep-ph/0001086].

[48] https://twiki.cern.ch/twiki/bin/view/Atlas/AtlFastProduction

[49] M.L. Mangano, M.Moretti, F.Piccinini, R.Pittau and A.Polosa, *JHEP* **0307** (2003) 001, [hep-ph/0206293]

[50] E.Richter-Was, D.Froidevaux and L.Poggioli, *ATLAS Internal Note* **ATL-PHYS-98-131** (1998).

[51] A. G. Frodesen, O. Skjeggestad, H. T$\bar{o}$fte, *Probability and Statistic in Particle Physics*, Universitetsforlaget (1979).